Northumbria Research Link

Northumbria Research Link

Hybrid Mode Feed Horns for Reflector Antennas Operating at 20/30GHz

David Charles **Geen**

A thesis submitted in fulfilment
of the requirements of
Northumbria University
for the degree of
Doctor of Philosophy

School of Computing, Engineering and Information Sciences
Northumbria University
Newcastle-upon-Tyne, NE1 8ST
United Kingdom

December 2004

Contents

Abstract

This thesis presents the findings of an investigation into hybrid mode feed horns for use in the next generation of reflector antennas for satellite communications at Ka-band.

Within the thesis, general field theory is developed and subsequently applied to specific horn-types in an effort to understand and explore the limits of the bandwidth over which they can offer suitable radiation characteristics. Studies into the use of both corrugated and dielectric-loaded horns identify a shortfall in their performance, particularly in the context as feeds for elliptical reflector antennas at Ka-band, as a consequence of the sizeable frequency separation between the Transmit and Receive functions.

The need to operate at two widely separated bands, with little concern for the performance at all frequencies in between, affords the opportunity to take advantage of two exclusive mechanisms to independently optimise the performance at two sub-bands, corresponding to the Transmit and Receive functions. The 'dual-band' concept is explored by extending the field theory developed earlier in the thesis, this being applied to a corrugated structure with secondary mechanism that takes effect once the performance as a consequence of the corrugations themselves begins to degrade.

The theory is tested by way of a practical investigation comparing the measured performance of different horn types, including a novel horn borne out of the dual-band concept described above. This led to the need to develop, construct and evaluate a suitable anechoic chamber, the work associated with this also being included in the thesis as an appendix.

The results are reviewed in the context of the Ka-band application against both RF and practical design goals with the conclusion that the novel dual-band horn offers superior performance with respect to the state-of-the-art.

Abstract

This thesis presents the findings of an investigation into hybrid mode feed horns for use in the next generation of reflector antennas for satellite communications at Ka-band.

Within the thesis, general field theory is developed and subsequently applied to specific horn-types in an effort to understand and explore the limits of the bandwidth over which they can offer suitable radiation characteristics. Studies into the use of both corrugated and dielectric-loaded horns identify a shortfall in their performance, particularly in the context as feeds for elliptical reflector antennas at Ka-band, as a consequence of the sizeable frequency separation between the Transmit and Receive functions.

The need to operate at two widely separated bands, with little concern for the performance at all frequencies in between, affords the opportunity to take advantage of two exclusive mechanisms to independently optimise the performance at two sub-bands, corresponding to the Transmit and Receive functions. The 'dual-band' concept is explored by extending the field theory developed earlier in the thesis, this being applied to a corrugated structure with secondary mechanism that takes effect once the performance as a consequence of the corrugations themselves begins to degrade.

The theory is tested by way of a practical investigation comparing the measured performance of different horn types, including a novel horn borne out of the dual-band concept described above. This led to the need to develop, construct and evaluate a suitable anechoic chamber, the work associated with this also being included in the thesis as an appendix.

The results are reviewed in the context of the Ka-band application against both RF and practical design goals with the conclusion that the novel dual-band horn offers superior performance with respect to the state-of-the-art.

Abstract

This thesis presents the findings of an investigation into hybrid mode feed horns for use in the next generation of reflector antennas for satellite communications at Ka-band.

Within the thesis, general field theory is developed and subsequently applied to specific horn-types in an effort to understand and explore the limits of the bandwidth over which they can offer suitable radiation characteristics. Studies into the use of both corrugated and dielectric-loaded horns identify a shortfall in their performance, particularly in the context as feeds for elliptical reflector antennas at Ka-band, as a consequence of the sizeable frequency separation between the Transmit and Receive functions.

The need to operate at two widely separated bands, with little concern for the performance at all frequencies in between, affords the opportunity to take advantage of two exclusive mechanisms to independently optimise the performance at two sub-bands, corresponding to the Transmit and Receive functions. The 'dual-band' concept is explored by extending the field theory developed earlier in the thesis, this being applied to a corrugated structure with secondary mechanism that takes effect once the performance as a consequence of the corrugations themselves begins to degrade.

The theory is tested by way of a practical investigation comparing the measured performance of different horn types, including a novel horn borne out of the dual-band concept described above. This led to the need to develop, construct and evaluate a suitable anechoic chamber, the work associated with this also being included in the thesis as an appendix.

The results are reviewed in the context of the Ka-band application against both RF and practical design goals with the conclusion that the novel dual-band horn offers superior performance with respect to the state-of-the-art.

Abstract

This thesis presents the findings of an investigation into hybrid mode feed horns for use in the next generation of reflector antennas for satellite communications at Ka-band.

Within the thesis, general field theory is developed and subsequently applied to specific horn-types in an effort to understand and explore the limits of the bandwidth over which they can offer suitable radiation characteristics. Studies into the use of both corrugated and dielectric-loaded horns identify a shortfall in their performance, particularly in the context as feeds for elliptical reflector antennas at Ka-band, as a consequence of the sizeable frequency separation between the Transmit and Receive functions.

The need to operate at two widely separated bands, with little concern for the performance at all frequencies in between, affords the opportunity to take advantage of two exclusive mechanisms to independently optimise the performance at two sub-bands, corresponding to the Transmit and Receive functions. The 'dual-band' concept is explored by extending the field theory developed earlier in the thesis, this being applied to a corrugated structure with secondary mechanism that takes effect once the performance as a consequence of the corrugations themselves begins to degrade.

The theory is tested by way of a practical investigation comparing the measured performance of different horn types, including a novel horn borne out of the dual-band concept described above. This led to the need to develop, construct and evaluate a suitable anechoic chamber, the work associated with this also being included in the thesis as an appendix.

The results are reviewed in the context of the Ka-band application against both RF and practical design goals with the conclusion that the novel dual-band horn offers superior performance with respect to the state-of-the-art.

THE BRITISH LIBRARY

DOCUMENT SUPPLY CENTRE

Boston Spa, Wetherby, West Yorkshire LS23 7BQ

BRITISH LIBRARY DOCTORAL THESIS AGREEMENT FORM

The British Thesis Service is designed to promote awareness of and improve access to the results of publicly funded British Doctoral Research.

Theses in the scheme are publicised through various current awareness media including printed subject bulletins and on-line databases.

On demand access is provided for individual researchers and libraries from a single, central collection of more than 120,000 doctoral theses.

Access Agreement

Through my *university/~~college/department~~, I agree to supply the British Library Document Supply Centre, with a copy of my thesis.

I agree that my thesis may be copied on demand for loan or sale by the British Library, or its agents, to requesting libraries (who may add the copy to their collection for loan or consultation) or individuals. I understand that any copies of my thesis will contain the following statement:

This copy has been supplied on the understanding that it is copyright material and that no quotation from the thesis may be published without proper acknowledgement.

I confirm that the thesis and abstracts are my original work, that further copying will not infringe any rights of others, and that I have the right to make these authorisations. Other publication rights may be granted as I choose.

The British Library agrees to pay me a royalty of ten percent on any sales of the second and subsequent copies of my thesis per year. The royalty will be paid annually in April.

In order to be eligible for such royalties, I agree that my obligation is to notify the British Library of any change of address.

* *please delete as applicable.*

INSTRUCTIONS FOR BRITISH DOCTORAL THESIS FORM

Please complete this agreement carefully, so that your thesis can be made available as rapidly as possible. Please type or print in black, and look through the instructions which follow for explanations concerning the Agreement Form.

ITEM 1:

Full name. This should be as shown on your title page, and as registered with the awarding body.

ITEM 2:

Future mailing address. This is the address at which you can be reached after you have completed your degree requirements. It will be used in mailing any royalties due from the sale of your thesis.

ITEM 3a:

Please enter your university name, plus college or department. For example: University of York, Department of Computer Science.

ITEM 4:

Enter the name(s) of any sponsoring body other than those in 3a.

ITEM 8:

Additional keywords. If your thesis requires additional keywords for identification which are not included in the title, please add up to five keywords.

ITEM 9:

Select from the Subject Categories section in this leaflet the one category that best relates to the subject content of your thesis. Enter the corresponding code in the boxes and the category title next to it. If you wish, you may indicate up to two additional subject codes.

STANDARDS

The physical presentation of your thesis should be in accordance with the following specifications:

- The copy must be legible. The size of character used in the main text, including displayed matter and notes, should be not less than 2.0mm for capitals and 1.5mm for x-height (height of lower case x)

- Paper should be size A4, white and within the range $70g/m^2$ to $100g/m^2$.

- Text should be single sided - right hand pages (rectos) only.

- The margin at the binding edge of the page should be not less than 40mm. Other margins should be not less than 15mm. Running heads and page numbers should be within the recommended margins.

The recommendations as set out in the withdrawn BS 4821:1990 remain good practice.

IMPORTANT:

If your thesis is not produced according to these standards, it may not be possible to include it in the scheme.

BRITISH DOCTORAL THESIS AGREEMENT FORM

Please type or print in black ink

Personal Data

1 Surname _____GEEN_____

Forenames _____DAVID CHARLES_____

2 Present mailing address _____

_____46, EDINBURGH ROAD_____

_____PEEBLES_____

_____EH45 8EB._____

Future mailing address _____

_____

_____

_____

Effective date for future address _____

Doctoral Degree Data

3 Full name of University conferring degree, and college or division if appropriate

_____NORTHUMBRIA UNIVERSITY_____

_____

Department _____School of Computing, Engineering + Info. Sciences_____

4 Name of co-sponsoring body(ies) (if any)

_____

_____

_____

_____

5 Abbreviations for degree awarded

_____PhD_____

6 Date degree awarded ___26/8/05.___

7 Title of thesis _____HYBRID MODE FEED HORNS FOR REFLECTOR ANTENNAS OPERATING AT 20/30 GHz._____

8 List up to five additional descriptive keywords or short phrases not in your thesis title to help subject access.

a _____Corrugated Horns_____

b _____Dual - mode Horns_____

c _____Elliptical Reflector Antennas_____

d _____Satellite antennas_____

e _____Ka - Band_____

9 Subject category for your thesis. Enter a code from the Subject Category list overleaf and write in the category selected. You may enter two additional categories and/or codes on the extra lines provided.

0	9	0	Electrical Engineering
2	0	0	Physics, general
1	7	B	Communications Systems, Telecoms.

10 Language of text (if not English)

_____

IMPORTANT:
You must sign the Access Agreement on page 1 of this leaflet and enclose it with this form and your thesis

Hybrid Mode Feed Horns for Reflector Antennas Operating at 20/30GHz

David Charles **Geen**

A thesis submitted in fulfilment of the requirements of

Northumbria University

for the degree of

Doctor of Philosophy

School of Computing, Engineering and Information Sciences

Northumbria University

Newcastle-upon-Tyne, NE1 8ST

United Kingdom

December 2004

Abstract

This thesis presents the findings of an investigation into hybrid mode feed horns for use in the next generation of reflector antennas for satellite communications at Ka-band.

Within the thesis, general field theory is developed and subsequently applied to specific horn-types in an effort to understand and explore the limits of the bandwidth over which they can offer suitable radiation characteristics. Studies into the use of both corrugated and dielectric-loaded horns identify a shortfall in their performance, particularly in the context as feeds for elliptical reflector antennas at Ka-band, as a consequence of the sizeable frequency separation between the Transmit and Receive functions.

The need to operate at two widely separated bands, with little concern for the performance at all frequencies in between, affords the opportunity to take advantage of two exclusive mechanisms to independently optimise the performance at two sub-bands, corresponding to the Transmit and Receive functions. The 'dual-band' concept is explored by extending the field theory developed earlier in the thesis, this being applied to a corrugated structure with secondary mechanism that takes effect once the performance as a consequence of the corrugations themselves begins to degrade.

The theory is tested by way of a practical investigation comparing the measured performance of different horn types, including a novel horn borne out of the dual-band concept described above. This led to the need to develop, construct and evaluate a suitable anechoic chamber, the work associated with this also being included in the thesis as an appendix.

The results are reviewed in the context of the Ka-band application against both RF and practical design goals with the conclusion that the novel dual-band horn offers superior performance with respect to the state-of-the-art.

Contents

List of Figures

List of Tables

x

Acknowledgements

Author's Declaration

I hereby declare that this thesis is entirely my own work and has not been submitted in support of an application of another degree or qualification of this or any other university, institute of learning or industrial organisation.

List of Publications

Geen, D.C. and Smith, D.: *Design, construction and performance of a small, low cost anechoic measuring system for research applications*, IEEE AP-S International Symposium, June 18-23 1995, Newport Beach, California, USA.

Geen, D.C. and Smith, D.: *Enhanced teaching of antenna theory and measurement techniques using a low cost anechoic measuring system*, 25th European Microwave Conference, Sept. 4-8 1995, Bologna, Italy.

Smith, D., Geen, D.C. and Johns, D.: *Application of a 3-dimensional transmission line modelling method to the simulation of conical corrugated horns*, International Conference on Electromagnetics in Advanced Applications, Sept. 12-15 1995, Turin, Italy.

Geen, D.C. and Smith, D.: *Wide flare-angle horn antenna with means for radiating low levels of crosspolarisation in two widely separated frequency bands*, IEEE AP-S International Symposium, 1996, Baltimore, USA, Vol. 3, pp 2026-29.

Geen, D.C. and Smith, D.: *Compact anechoic chamber and antenna measurement system for microwave teaching and research applications*, Microwave and Optics Technology Letters, 1996.

Geen, D.C. and Smith, D.: *Narrow flare-angle, dual-band horn antenna with good crosspolar and VSWR characteristics*, 26th European Microwave Conference, 1996, Prague.

Glossary of acronyms

ACTS	Advanced Communication Test Satellite
APC	Antenna Pattern Comparison
BSS	Broadcast Satellite Services
CODE	Co-operative Olympus Data Experiment
CP	Circular Polarisation
DUT	Device Under Test
EIRP	Effective Isotropic Radiated Power
FSS	Fixed Satellite Services
HLP	Horizontal Linear Polarisation
IP	Internet Protocol
LHCP	Left Hand Circular Polarisation
LP	Linear Polarisation
RHCP	Right Hand Circular Polarisation
SGH	Standard Gain Horn
TE	Transverse Electric
TM	Transverse Magnetic
VLP	Vertical Linear Polarisation
VSAT	Very Small Aperture Terminal
VSWR	Voltage Standing Wave Ratio

Chapter 1

Introduction to the research program.

1.1 Ka-band as an emerging technology

To date the majority of geostationary, commercial satellite communication systems have operated at C-band (4/6GHz) and more recently Ku-band (11/14GHz). However, an increase in the demand for satellite relay services fuelled mainly by a dramatic rise in wideband digital IP traffic, coupled with congestion of the geostationary arc caused by the growing number of satellites filling existing orbital slots, has resulted in the need to develop the next generation of satellite services offering additional capacity.

To address this, in the mid-1990's, Ka-band spectrum (20/30GHz) was allocated to both FSS (Fixed Satellite Services) as well as Non-Geostationary Satellite Services. The FSS Ka-band spectrum allocation was given twice the bandwidth as is now available to the C, Ku-FSS and Ku-BSS (Broadcast Satellite Services) fleets of satellites. So, a typical Ka-band satellite may have 1 GHz or more of available spectrum for use on either of two orthogonal polarisations; legacy C and Ku-band satellites only having 500-575 MHz. With FSS Ka-band satellites being coordinated every 2° (in a similar manner to legacy FSS C and Ku-band satellites), merely considering the spectrum and orbital arc plan allows the Ka-band satellite fleet to match the available FSS capacity of the C and Ku-band satellite fleets combined in any given region.

A 2° orbital coordination however brings with it the need to provide earth stations having radiation patterns with sufficiently narrow main beams and low off-axis sidelobe envelopes to ensure interference with neighbouring satellites is maintained at acceptable levels. At C-band and FSS Ku-band this has traditionally been addressed with the use of relatively large antennas ($\approx$3m diameter at C-band and

1

≈90cm diameter at FSS Ku-band), neither of which are viable solutions for a new mass-market of consumers, from both a cost and a practical standpoint, particularly in dense conurbations.

Notably, those satellite systems that do employ small earth station antennas in widespread use today are for BSS Ku-band services, not FSS services. The BSS Ku-band satellite fleet is coordinated at orbital slots every 9° and at 12 GHz these small (45-65cm diameter) antennas exhibit acceptable interference rejection from adjacent satellites spaced so far apart. Whilst such antennas meet the commercial goal of offering a low-cost solution for consumers and small-to-medium enterprises utilising BSS services, for existing C and FSS Ku-band frequency plans they cannot be made to deliver the technical requirements for 2° orbital spacing.

However, as the operational frequency of these small antennas migrates to a Ka-band frequency, the antennas become much more directive (higher on-axis gain with similar off-axis gain), thereby allowing them to offer the superior performance suited to the adjacent satellite interference specifications. Coupled with recent advances in satellite on-board processing technology allowing spot beams with increased EIRP to combat atmospheric fading, the convenient size of the antenna opens the way for a massive increase in the number of potential users and there begins to emerge a strong business case for broadband IP via satellite at Ka-band.

To add credence and support to these arguments, significant Ka-band experiments have already been carried out to investigate the propagation characteristics and feasibility of the band. In the USA research was encouraged through the ACTS program [1.1], which performed extensive propagation experiments that proved communications in this new frequency band are indeed viable. The results provided by ACTS, which was only decommissioned earlier this year (2004), are particularly valuable as they have been collected over a thirteen year period and are statistically robust. Encouragement can also be drawn from work in Europe supported by the European Space Agency (ESA) through an experiment called CODE (Co-operative Olympus Data Experiment) [1.2] which, as the name suggests, utilised the 20/30GHz communications payload of the Olympus satellite until its decommissioning in 1994.

Despite strong scientific support, implementation of Ka-band has, until recently, been slow due largely to the reticence of the major satellite operators to provide the significant investment required to generate momentum and subsequently confidence in this new market. In addition, development of digital coding techniques that improved the bandwidth usage at Ku-band reduced the pressure on the immediate need to migrate to the next generation systems.

However, the requirement for Ka-band has recently been reinforced by the increased demand for High Definition TV, a particularly bandwidth-hungry TV format, as well as increased demand for IP traffic. Today, with commercial programmes such as WildBlue [1.3] now well underway, Ka-band looks like it is here to stay and work to develop the appropriate hardware is gathering momentum.

Consequently, work to develop better, smaller and less expensive hardware is continuing, interest in the design of appropriate antennas has grown and the need to research the antenna design issues has increased.

The following section examines the antenna design parameters with a view to highlighting the relevance of the work undertaken as part of this research programme in the context of the background presented above.

1.2 Reflector antenna design parameters

The majority of antennas are designed to focus electromagnetic energy in a given direction, thereby allowing for the transfer of energy over a larger distance than if the energy had not been focused, but instead, allowed to radiate equally in all directions. The antenna's ability to collimate or focus maximum energy in a given direction is referred to as its directivity, or gain if antenna ohmic losses are taken into account. In addition, the manner in which this energy is spread over an angular region centred about the direction of maximum radiated energy is called the radiation pattern and it is this together with antenna gain that are most often used, directly or indirectly, as the measure of an antenna's suitability for a given application.

In the case of satellite communications where the distances over which signals must travel are necessarily large and the risk of interference great as a consequence of the close proximity between adjacent satellites on the geostationary arc, the ideal characteristics of such a pattern would be one in which all the energy was focussed into an infinitely narrow beam as approximated in Figure 1.1.
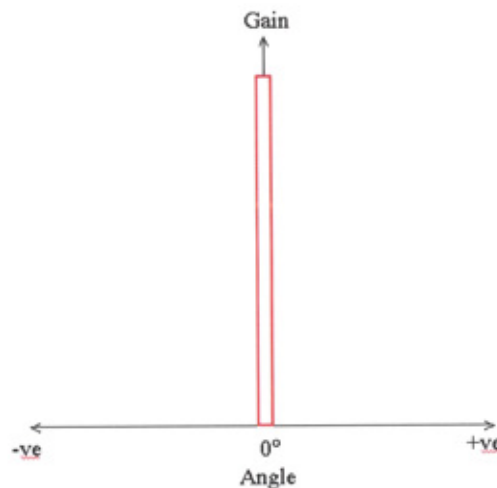
Figure 1.1 *Hypothetical ideal antenna radiation pattern for satellite communications*

Although such a pattern is not realistically achievable, a close approximation can be achieved with use of reflector type antennas, specifically offset reflector antennas, for which Figure 1.2 illustrates a typical radiation pattern.
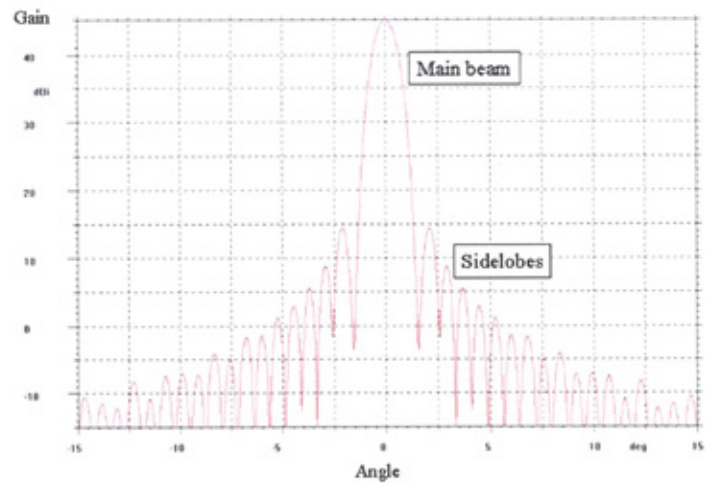
(a)
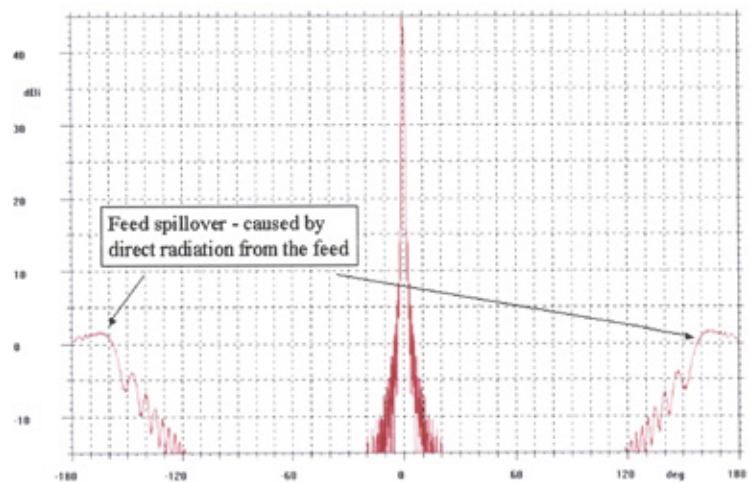
(b)

Figure 1.2 *Example of typical radiation pattern for a single-offset reflector antenna*

Notice in Figure 1.2 how the first sidelobe is almost 30dB down with respect to the maximum gain. This is a direct consequence of eliminating any blockage from the antenna aperture with use of an offset reflector geometry, as illustrated in Figure 1.3. The alternative would be an axisymmetric geometry where the feed sits at the centre of the aperture, the level of the first sidelobe and the resulting potential for increased interference from and to adjacent satellites being proportional to the percentage of the aperture blocked by the feed [1.4].

Offset reflector antennas are therefore well suited to satellite communications and for low cost applications, single-offset antenna geometries in particular represent the design of choice for the industry.
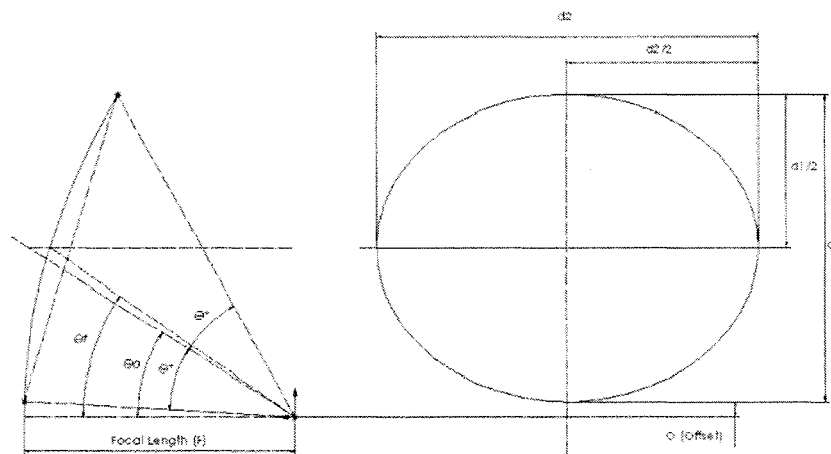
Figure 1.3 *Elliptical single-offset reflector antenna geometry*

With the parameters of the satellite itself generally pre-defined and fixed, the effectiveness of a communication link in terms of bit error rate and availability are largely set by the earth station antenna on-axis EIRP (Effective Isotropic Radiated Power), obtained from the product of transmitter power and antenna gain. To improve link performance it is not always possible to simply increase the on-axis EIRP without a corresponding increase to the off-axis EIRP, that is to say the EIRP outside the main beam as a consequence of the antenna sidelobes. Off-axis EIRP is

strictly regulated by the relevant authorities to avoid interference and power can only be radiated within a specified sidelobe envelope. There is therefore a limit to the maximum allowable on-axis EIRP dictated by the off-axis sidelobe characteristics, or radiation pattern, of the individual antenna and there is a need to optimise the antenna design accordingly.

Two main factors influence the antenna gain and radiation pattern, the first being the reflector optical geometry and the second being the way in which a given reflector is illuminated by the primary source of electromagnetic energy.

The reflector geometry is determined through optical theory such that energy emanating from a primary source located at the reflector system's focal point is properly focussed. The primary source illumination characteristics are governed by the design of the feed, its function being to control the distribution of electromagnetic energy over the surface of the reflector.

The feed characteristics and reflector optics, and the subsequent interaction between them, influence the antenna design through the antenna efficiency, η, which in turn relates the effective gain, G_{eff}, to the theoretical gain, G, through

$$G_{eff} = G\eta \tag{1.1}$$

where $G = 4\pi A / \lambda^2$, A being the aperture area.

η is the product of a number of terms each of which defines the efficiency of the antenna in different key areas and as such is given by;

$$\eta = \eta_{illumination} \cdot \eta_{spillover} \cdot \eta_{crosspol} \cdot \eta_{feed\,loss} \cdot \eta_{blockage} \cdot \eta_{refl.\,surface\,error} \tag{1.2}$$

The design goal is to maximise the overall efficiency in order to achieve the maximum gain for a given size of antenna or conversely, minimise the antenna size for a given gain requirement.

Equation 1.2 shows the first four terms are dependant on the performance of the primary feed since both its copolar and crosspolar components are transformed directly through the reflector system to appear in the secondary far-field radiation characteristics. Consequently, the feed is the single most influential element with regard to the efficiency of the overall antenna sub-system and as such has been the subject of a great deal of research since the advent of satellite communications in the late 1950's.

For frequencies above approximately 2GHz the feed usually takes the form of an aperture type antenna, examples of which are given in Figure 1.4.

It is the investigation into the design of the primary feed in the context of small (<70cm diameter), single-offset reflector geometries for use as the next generation of consumer Ka-band antenna sub-systems that is the subject of the work reported herein.
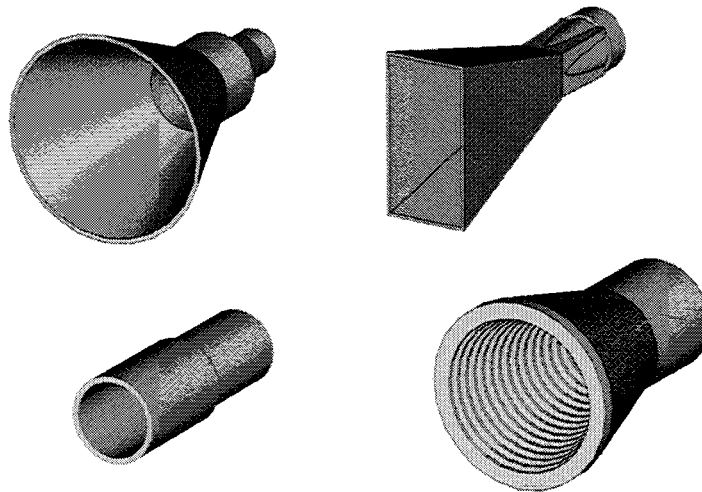
Figure 1.4 *Examples of primary feed horns*

1.3 Horn antenna design scope

With a view to setting out a scope of work it is worthwhile to highlight the main design boundary conditions for the primary feed. Based on the Ka-band application described so far and in accordance with Equation 1.2 these can be summarised as:

Design boundary conditions for the feed horn:

1. Control of copolar patterns to properly illuminate the reflector optical geometry

2. Low crosspolarisation to allow frequency reuse

3. Good VSWR (return loss)

4. Low insertion loss

5. Environmentally hardy (outdoor 10 year life-cycle)

6. Lends itself to low-cost, high-volume manufacture

where these are applicable in the context of the 20/30GHz bands for simultaneous receive and transmit functions.

These characteristics, particularly the desire for low crosspolarisation over such a wide overall operating bandwidth, are consistent with the performance of a class of feed horns called hybrid mode horn antennas. In accordance, these will be examined for the general case in Chapter 2 before the specific cases of the corrugated and dielectric-loaded horn are investigated in Chapters 3 and 4 respectively, the aim being to assess their suitability for this application against the design boundary conditions above.

Up to, and including Chapter 4 no specific reflector geometry is assumed, however in Chapter 5 the performance of the horns of Chapters 3 and 4 are examined in the context of non-circular reflector apertures where a shortfall in their ability to deliver the desired performance over an extended bandwidth is identified.

Chapter 6 goes on to identify a novel horn design with the potential to offer superior performance to the conventional horns of Chapters 3 and 4 by employing two

exclusive mechanisms to optimise the performance at the upper (transmit) and lower (receive) sub-bands independently.

Chapter 7 then provides practical and theoretical results for various forms of corrugated and dielectric-loaded horn designs and Chapter 8 provides an evaluation of the results together with further discussion. By way of a comparison and in an attempt to benchmark the designs, it includes a review of each horn-type against the six design boundary conditions listed here. Chapter 9 goes on to conclude the research and provide ideas for further work.

Additional material on general aperture theory in support of Chapter 2 together with details of work carried out towards the design, build and evaluation of a suitable anechoic chamber to assist with this research are provided in Appendices 1 and 2 respectively.

1.4 References

[1.1]   Gedney, R.T., Wright, D.L., Balombin, L., Sohn, P.Y.: *Advanced Communications Technology Satellite (ACTS)*, Nasa report IAF-90-481, 1990.

[1.2]   European Space Agency's *Olympus users' guide*, Ref no. UG-6-1-S/JC/pat2.

[1.3]   www.wildblue.com

[1.4]   Hatcher, B.R.: *Graphs estimate feed blockage*, Microwaves, July 1971, pp 31-32.

Chapter 2

General modal analysis of hybrid mode structures

In this chapter the general form of the field components within cylindrical hybrid mode waveguides will be developed in preparation for subsequent analysis in Chapters 3 and 4 where they will be specified fully for the particular cases of corrugated and dielectric-loaded waveguide.

After determining the transverse fields, the overall aim is to substitute these into Equation A1.23 in order to predict the copolar and crosspolar radiation performance.

2.1 Introduction to modal analysis

The classical method of studying the field distributions in waveguide is to determine the modal characteristics as described by solutions of Maxwell's equations subject to the application of specific boundary conditions dictated by the waveguide geometry. Solutions take the form of an infinite series of orthogonal field distributions, or modes, each being expressed in terms of either cylindrical or spherical wave functions divided into axial and transverse components. It is the transverse components that are of most interest since it is these that are generally assumed to be the aperture fields, as used to calculate radiation characteristics.

For a given coordinate system, appropriate to the waveguide geometry, the relationships between the components of the electromagnetic fields are given by Maxwell's equations and by the equations representing the properties of the medium in which the fields exist. Where the medium is a perfect insulator with no stored charges, general solutions to Maxwell's equations take the form [2.1]

$$\nabla^2 \Psi = -\omega^2 \mu \varepsilon \, \Psi = -k^2 \Psi \qquad (2.1)$$

where k is known as the unbounded wavenumber.

Equation 2.1 is known as the Helmholtz wave equation and is used to obtain solutions of the form of the electric and magnetic field quantities. Application of the boundary conditions set by the cross section of the device then yield the propagation and amplitude coefficients thereby allowing the fields to be specified fully.

In smooth walled, metallic waveguide solutions take the form of transverse electric (TE) or transverse magnetic (TM) modes possessing longitudinal components of either the magnetic field (H_z) or the electric field (E_z) respectively. Other waveguide structures can be made to support different types of modes possessing longitudinal components of both H_z and E_z, these being known as hybrid modes. Of particular interest is the hybrid mode designated HE_{11} in circular waveguide which has been found to have extremely desirable properties for antenna applications especially with regard to its pattern symmetry and polarisation purity [2.2, 2.10].

2.2 Characterisation of the HE_{11} mode

The characteristics of the HE_{11} mode can be demonstrated by considering it as a combination of TE_{11} and TM_{11} modes in smooth-walled circular waveguide. By examining the field distributions illustrated in Figure 2.1, it is apparent that the fundamental TE_{11} mode exhibits a zero field at the aperture edge in the $\phi = \pi/2$ plane (H-plane) and a positive, non-zero field at the aperture edge in the $\phi = 0$ plane (E-plane). The non-zero field gives rise to significant diffraction and poor sidelobe performance [2.3, 2.4] and because the field distribution is asymmetrical in ϕ there is a relatively high crosspolar field component.

In comparison, the TM_{11} mode exhibits a zero field at the aperture edge in the $\phi = \pi/2$ plane and a negative, non-zero field at the aperture edge in the $\phi = 0$ plane. Furthermore, the crosspolar field component is almost equal but opposite to that due to the TE_{11} mode. It is reasonable to suggest that the vector addition of a suitable combination of TE_{11} and TM_{11} modes can be made to exhibit a smooth truncation of the fields at the aperture edge with near equal E- and H-plane distributions and

consequently a much reduced crosspolar component. These properties are carried over to the far-field radiation patterns as shown in Figure 2.2 which compares the radiation pattern due to the TE_{11} mode with that due to an appropriate combination of TE_{11} and TM_{11} modes. The difference is significant with the E-plane sidelobe level dropping from -18dB to -41dB, the level of crosspolar radiation falling from -18dB to -36dB and much improved E- and H-plane pattern symmetry over the majority of the main lobe. These are desirable characteristics with which to illuminate reflector antennas.

The close-to-zero fields at the edge of the aperture yield correspondingly small currents on the waveguide or horn flange, thereby bringing added confidence to the assumption made for the aperture theory of Appendix 1 whereby the currents on the flange are neglected.

For a smooth walled waveguide or horn antenna the TE_{11} and TM_{11} modes propagate with different velocities and in order to obtain the desired effect the two modes must be properly phased as well as being of the correct magnitude. This is achieved by introducing a discontinuity to couple the required amount of energy from the dominant TE_{11} mode to the TM_{11} mode at such a position along the length of the horn that the field components combine favourably at the aperture. Horns which take advantage of this effect are called dual-mode horns and two noteable examples are the Potter horn [2.5] and Satoh's dielectric, ring-loaded horn [2.6].
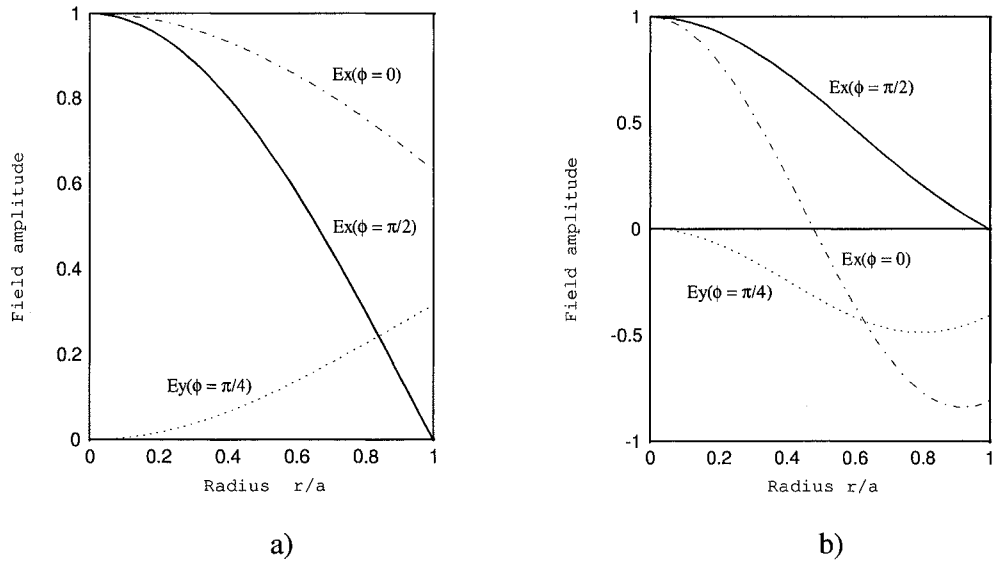
Figure 2.1 *Aperture field distribution of a) TE_{11} and b) TM_{11} modes in smooth-walled circular waveguide of radius* a
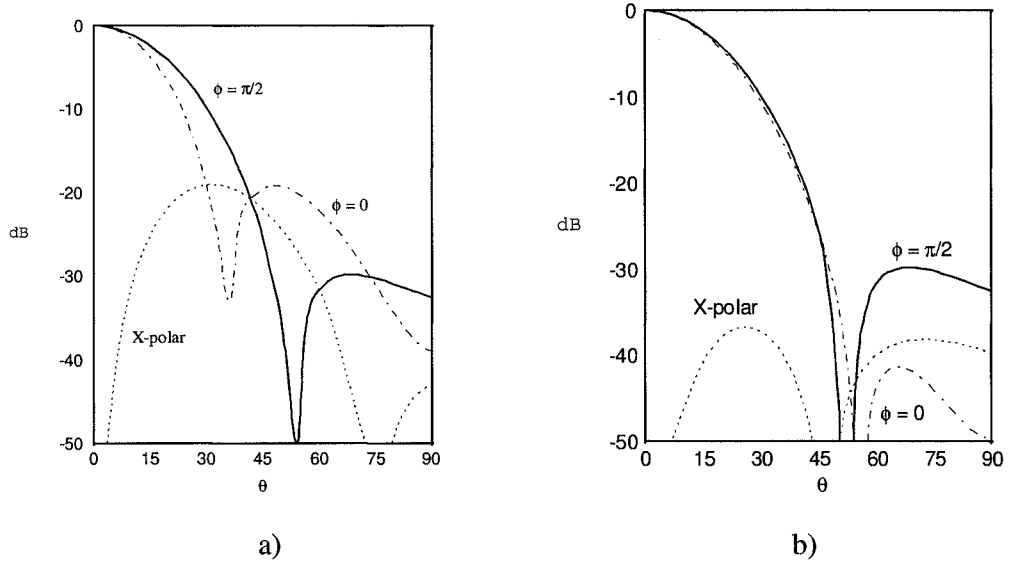
Figure 2.2 *Radiation patterns of a smooth-walled circular waveguide carrying a) only the TE_{11} mode and b) 67%TE_{11} mode combined in-phase with 33%TM_{11} mode*

The performance of the dual-mode horn is limited by its relatively narrow bandwidth due to the requirement to correctly phase the two separate modes. If, as a consequence of choosing the right boundary conditions, the two modes were made to

15

travel at the same waveguide velocity over a significant range of frequencies, the condition for low crosspolarisation could be achieved over a wide band. Under such conditions, where axial components of both electric (E_z) and magnetic (H_z) fields are present, the resulting mode would be considered hybrid.

2.3 Boundary conditions for Hybrid Modes

The boundary surfaces capable of supporting hybrid modes include metallic corrugated surfaces and interfaces between dielectrics of different permitivities. Following Clarricoats [2.7, 2.8], the mathematical representation of such boundaries can be simplified considerably by approximating them as having constant surface impedance (Z) and admittance (Y) characteristics, where these relate the electric and magnetic fields tangential to the boundary surface such that, in cylindrical coordinates

$$Z = \frac{E_\phi}{H_z} \quad \text{and} \quad Y = -\frac{H_\phi}{E_z} \qquad (2.2)$$

The concept of Z and Y being constant refers to them being independant of the angle at which an incident wave strikes the surface and allows the problem to be treated by means of modal analysis similar to that used for a conventional, homogeneously-filled, closed waveguide.

Modal analysis of hybrid modes is discussed in the following sections. The general boundary value problem is evaluated with use of the constant surface reactance approximation to yield general expressions for the transverse field components in cylindrical waveguides of circular cross-section.

16

2.4 Cylindrical modal analysis

Applying the separation of variables [2.9] to Equation 2.1 in cylindrical coordinates, general solutions are of the form

$$\psi = B_m(k_\rho r)e^{-jk_z z}e^{-jm\phi} \qquad (2.3)$$

where a time dependence $e^{j\omega t}$ is assumed. The ϕ and z dependent terms are harmonic functions usually expressed as sines or cosines. $B_m(k_\rho r)$ denotes solutions to Bessel's equation of order m commonly given by $J_m(k_\rho r)$, representing Bessel functions of the first kind or $N_m(k_\rho r)$, representing Bessel functions of the second kind, or by a linear combination of both. The constants k_ρ and k_z are the transverse and axial wavenumbers or propagation constants respectively, these being connected through the relationship $k^2 = k_\rho^2 + k_z^2$. k is the unbounded wavenumber defined as $k^2 = \omega^2 \varepsilon \mu$ (as in Equation 2.1), its value being set by the frequency of operation and the medium through which the wave is propagating.

Consider a circular cylindrical waveguide consisting of two annular regions as in Figure 2.3. At the boundary $r = r_1$ the surface impedance and admittance are considered finite, hence, from Equation 2.2, axial components of both electric (E_z) and magnetic (H_z) fields are necessarily present. These, in turn, must satisfy Maxwell's equations

$$\nabla^2 E_z + k^2 E_z = 0 \qquad (2.4)$$

$$\nabla^2 H_z + k^2 H_z = 0 \qquad (2.5)$$

which from Equation 2.1 and 2.3 have general solutions of the form

$$\psi = \left[a_m J_m(k_\rho r) + b_m N_m(k_\rho r)\right] e^{-jk_z z} e^{-jm\phi} \qquad (2.6)$$
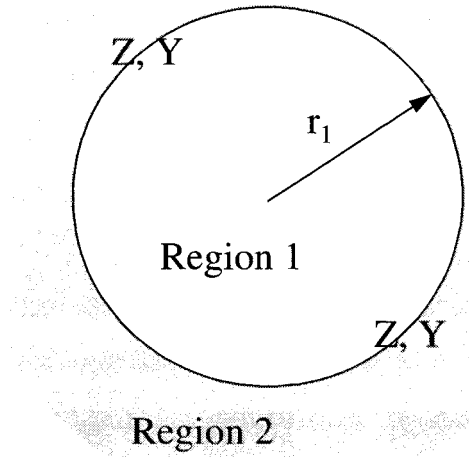
Figure 2.3 *Cylindrical boundary model for circular waveguide*

In the inner region containing the axis $r = 0$, Bessel functions of the second kind are excluded due to the requirement that the fields are finite. Solutions therefore reduce to

$$E_{z_1} = a_m J_m \left(k_{\rho_1} r \right) e^{j(\omega t - m\phi - k_z z)}$$

(2.7)

$$H_{z_1} = -j\eta_1 b_m J_m \left(k_{\rho_1} r \right) e^{j(\omega t - m\phi - k_z z)}$$

(2.8)

where $\eta_1 = (\mu_1 / \varepsilon_1)^{1/2}$ and the subscript 1 denotes region 1 of Figure 2.3.

Since both the electric and magnetic field components are present, the modes are necessarily hybrid. The degree to which a given mode is hybrid is defined as the ratio of H_z to E_z which from Equation 2.7 and 2.8 leads to

$$\overline{\Lambda} = -j \frac{b_m}{a_m} \eta_1 \qquad\qquad (2.9)$$

where $\overline{\Lambda}$ is known as the hybrid factor. Equation 2.7 and 2.8 can now be rewritten as

$$E_{z_1} = a_m J_m \left(k_{\rho_1} r \right) e^{-jm\phi} \qquad\qquad (2.10)$$

$$H_{z_1} = j a_m \eta_1^{-1} \overline{\Lambda} J_m \left(k_{\rho_1} r \right) e^{-jm\phi} \qquad\qquad (2.11)$$

where $e^{j\omega t}$ is assumed and the z dependence has been dropped for convenience. Knowing the form of the axial field components, the form of the transverse field components are obtained through the relationships defined by Maxwell's equations and are given by

$$E_{\phi_1} = -a_m G_1 \left[\overline{\Lambda} F_m \left(k_{\rho_1} r \right) + \overline{k}_z m \right] e^{-jm\phi}$$

$$H_{\phi_1} = -j a_m \eta_1^{-1} G_1 \left[\overline{k}_z \overline{\Lambda} m + F_m \left(k_{\rho_1} r \right) \right] e^{-jm\phi}$$

$$\qquad\qquad (2.12)$$

$$E_{\rho_1} = -j a_m G_1 \left[\overline{\Lambda} m + \overline{k}_z F_m \left(k_{\rho_1} r \right) \right] e^{-jm\phi}$$

$$H_{\rho_1} = a_m \eta_1^{-1} G_1 \left[\overline{k}_z \overline{\Lambda} F_m \left(k_{\rho_1} r \right) + m \right] e^{-jm\phi}$$

where

$$G_1 = \frac{k_1 r}{\left(k_{\rho_1} r \right)^2} J_m \left(k_{\rho_1} r \right)$$

19

$$F_m\left(k_{\rho_1}r\right)=\left(k_{\rho_1}r\right)\frac{J_m^{'}\left(k_{\rho_1}r\right)}{J_m\left(k_{\rho_1}r\right)}$$

(2.13)

$$\overline{k}_z=\frac{k_z}{k_1}$$

and the prime denotes differentiation with respect to the argument.

Equation 2.12 give the form of the transverse fields in the inner region of the waveguide. In order to specify them fully it is necessary to determine the values of $\overline{\Lambda}$ and $\overline{k}_z$.

With this in mind, and in an effort to develop a general procedure for evaluating the field components, Equation 2.2 are rewritten in terms of Equations 2.10-2.12 at the boundary $r=r_1$ to yield two alternative expressions for $\overline{\Lambda}$

$$\overline{\Lambda}^{-1}=\frac{F_m(k_{\rho_1}r_1)-\left(\dfrac{(k_{\rho_1}r_1)^2}{k_1r_1}\right)\overline{Z}_m}{-\overline{k}_zm}$$

(2.14)

$$\overline{\Lambda}=\frac{F_m(k_{\rho_1}r_1)-\left(\dfrac{(k_{\rho_1}r_1)^2}{k_1r_1}\right)\overline{Y}_m}{-\overline{k}_zm}$$

(2.15)

where $\overline{Z}_m$ and $\overline{Y}_m$ are the normalised surface reactances at $r=r_1$ given by

$$\overline{Z}_m=\frac{-j}{\eta_1}Z$$

(2.16)

and

$$\overline{Y}_m=-j\eta_1Y$$

(2.17)

20

Equating 2.14 to 2.15 leads to the general modal characteristic equation for k_z in inhomogeneously filled circular cylindrical waveguide as

$$\left(m\,\bar{k}_z\right)^2 = \left[F_m\left(k_{\rho_1}r_1\right) - \left(\frac{(k_{\rho_1}r_1)^2}{k_1 r_1}\right)\bar{Z}_m\right]\left[F_m\left(k_{\rho_1}r_1\right) - \left(\frac{(k_{\rho_1}r_1)^2}{k_1 r_1}\right)\bar{Y}_m\right] \qquad (2.18)$$

In contrast to smooth-walled waveguides filled with a homogeneous medium, for which the relationships between the propagation coefficients are generally closed form expressions, for waveguides able to support hybrid modes there is often no direct relationship between the unbounded, transverse and longitudinal wavenumbers, and Equation 2.18 must be solved iteratively to determine $\bar{k}_z$.

Subtracting Equation 2.14 from 2.15 yields a second order quadratic equation for the hybrid factor such that

$$\bar{\Lambda}^2 - \bar{\Lambda}\frac{\left(\frac{(k_{\rho_1}r_1)^2}{k_1 r_1}\right)\left[\bar{Z}_m - \bar{Y}_m\right]}{-m\bar{k}_z} = 1 \qquad (2.19)$$

with the solution

$$\bar{\Lambda} = \pm\left(\frac{\Psi^2}{4} + 1\right)^{\frac{1}{2}} + \frac{\Psi}{2} \qquad (2.20)$$

where Ψ is given by

$$\Psi = \frac{\left(\frac{(k_{\rho_1}r_1)^2}{k_1 r_1}\right)\left[\bar{Z}_m - \bar{Y}_m\right]}{-m\bar{k}_z} \qquad (2.21)$$

Equation 2.18 and 2.20 describe the parameters $\overline{\Lambda}$ and $\overline{k}_z$ in terms of the normalised surface reactances $\overline{Z}_m$ and $\overline{Y}_m$ at $r = r_1$. These can only be specified with knowledge of the waveguide structure and boundary conditions, which are as yet unknown.

At this point, with no specific boundaries having been considered, it is useful to study general field and radiation characteristics from the results developed so far, under the assumption that only the fields in the inner region contribute to the radiated fields. To this end it is convenient to express the fields in Cartesian coordinates to allow for easy distinction between copolar and crosspolar components. Making use of the recurrence relationships [2.9], the relevant parts of Equation 2.12 are rewritten for an x directed electric field and for the dominant modes with $m = 1$ as

$$E_x(r,\phi) = -ja\frac{k_1}{2k_{\rho_1}}\left[J_0\left(k_{\rho_1}r\right)\left(\overline{\Lambda} + \overline{k}_z\right) + J_2\left(k_{\rho_1}r\right)\left(\overline{\Lambda} - \overline{k}_z\right)\cos 2\phi\right]$$

$$E_y(r,\phi) = -ja\frac{k_1}{2k_{\rho_1}}J_2\left(k_{\rho_1}r\right)\left(\overline{\Lambda} - \overline{k}_z\right)\sin 2\phi$$

$$\tag{2.22}$$

$$H_x(r,\phi) = j\frac{a}{\eta_1}\frac{k_1}{2k_{\rho_1}}J_2\left(k_{\rho_1}r_1\right)\left(\overline{\Lambda}\overline{k}_z - 1\right)\sin 2\phi$$

$$H_y(r,\phi) = -j\frac{a}{\eta_1}\frac{k_1}{2k_{\rho_1}}\left[J_0\left(k_{\rho_1}r\right)\left(\overline{\Lambda}\overline{k}_z + 1\right) + J_2\left(k_{\rho_1}r\right)\left(\overline{\Lambda}\overline{k}_z - 1\right)\cos 2\phi\right]$$

It is evident that, under the provision $\overline{k}_z = \overline{\Lambda}$, $E_y = 0$ and the aperture electric field is purely linearly polarised and independent of ϕ. The same characteristics are observed for the aperture magnetic field under the provision $\overline{\Lambda}\overline{k}_z = 1$. Such characteristics have been identified in section 2.2 as being extremely desirable for antenna feed applications, consequently it is important to determine the conditions

under which they occur from which design criteria may be obtained. To this end possible values for the two parameters $\overline{\Lambda}$ and $\overline{k}$ are

$$\overline{k}_z = 1 \tag{2.23}$$

and

$$\overline{\Lambda} = 1 \tag{2.24}$$

To a good approximation, Equation 2.23 is true for hybrid mode feeds with aperture radii greater than about 1.5λ, as verified in Chapter 3 (Equation 3.11). From Equation 2.20, Equation 2.24 is satisfied when $\overline{Z}_m = \overline{Y}_m$, for which Equation 2.20 actually reduces to $\overline{\Lambda} = \pm 1$. This is known as the balanced hybrid condition and the two roots correspond to the HE_{1n} and EH_{1n} modes respectively. For a sufficiently large aperture, such that $\overline{k}_z \rightarrow 1$, and under the balanced hybrid condition when $\overline{\Lambda} = +1$, the aperture electric fields in Equation 2.22 reduce to (except for a constant),

$$E_x(r, \phi) = J_0(k_{\rho_1} r_1)$$

$$E_y = 0$$

This corresponds to the HE_{11} mode for which the pattern is axially symmetric, being independent of ϕ, and the crosspolarisation is zero.

Conversely, under the condition $\overline{\Lambda} = -1$, the aperture electric fields reduce to (except for a constant),

$$E_x(r, \phi) = J_2(k_{\rho_1} r_1) \cos 2\phi$$

$$E_y(r,\phi) = J_2(k_{\rho_1} r_1)\sin 2\phi$$

corresponding to the EH_{11} mode whereby the pattern is completely ϕ-dependant and in fact is totally crosspolarised in the $\phi = \pm 45°$ planes.

For this, and most other applications, it is the fundamental HE_{11} mode under the condition $\overline{\Lambda} = +1$ that is of most interest because of its polarisation purity and circularly symmetric radiation characteristics.

With the behaviour of $\overline{\Lambda}$, and subsequently the aperture fields, being dependent on the boundary conditions at $r = r_1$, the physical requirements for low crosspolarisation in cylindrical waveguides differ according to the structure itself. For the special cases of corrugated and dielectric-loaded cylindrical waveguide, field solutions together with design criteria are developed next in Chapters 3 and 4 respectively.

2.5 References

[2.1]   Schelkunoff, S.A.: *Electromagnetic waves*, Van Nostrand, Princeton, N.J., 1943.

[2.2]   Dragone, C.: *Attenuation and radiation characteristics of the HE_{11} –mode*, IEEE Trans., 1980, MTT-28, pp 704-10.

[2.3]   King, A.P.: *The radiation characteristics of conical horn antennas*, Proc. IRE, March 1950, pp 249-51.

[2.4]   Schorr, M.G. and Beck, F.J.: *Electromagnetic field of the conical horn*, J. of App. Phys., 1950, Vol. 21, pp 795-801.

[2.5]   Potter, P.D.: *A new horn antenna with suppressed sidelobes and equal beamwidths*, Jet Propulsion Labs publications, June 1963, pp 71-78.

[2.6]   Satoh, T.: *Dielectric-loaded horn antenna*, IEEE Trans., 1972, AP-20, pp 199-201.

[2.7]   Clarricoats, P.J.B. and Saha, P.K.: *Propagation and radiation behaviour of corrugated feeds, part I corrugated waveguide feeds*, Proc. IEE, 1971, Vol. 118, pp 1167-76.

[2.8]   Clarricoats, P.J.B. and Saha, P.K.: *Propagation and radiation behaviour of corrugated feeds, part II corrugated conical horn feeds*, Proc. IEE, 1971, Vol. 118, pp 1177-86.

[2.9]   Harrington, R.F., *Time harmonic electromagnetic fields*, McGraw Hill, N.Y., 1961.

[2.10] Schrank, H. and Love, A.W.: *Spillover and beam efficiency for hybrid-mode feeds*, IEEE AP Magazine, August 1991, Vol. 33, No.4, pp 33-5.

Chapter 3

Modal analysis of Corrugated Waveguide

The corrugated feed is perhaps the most important class of all hybrid mode structures and has been employed extensively since first introduced by Kay in 1964 [3.1]. Since then it has been the subject of a great deal of research, most notably by Clarricoats [3.2], Dragone [3.3] and Thomas [3.4] et al.

The continued interest [3.5] is testament to the significant advantages offered by the corrugated structure, not least, as a feed for reflector antennas, as in this application. The following chapter examines, in general, the operation and performance of the corrugated horn and provides some indication as to its potential limitations when applied to applications for satellite communications at Ka-band.

3.1 Principles of operation

Referring to Figure 3.1, the principle of operation relies on there being a sufficient number of slots per wavelength such that the slot can only support radial TM fields with field components E_z, H_ϕ and H_ρ. The slot width must therefore be $< \lambda/2$.

With the correct geometry the boundary conditions presented by the surface allow TE and TM modes of corresponding order to propagate with the same velocity over a wide frequency range in the form of hybrid modes. The bandwidth limitations of the dual-mode horns of Chapter 2 are thereby overcome and desirable radiation properties are achievable for fractional bandwidths in excess of 50%.

By approximating the corrugated boundary as a constant surface reactance [3.2], it can be characterised by an impedance, Z and an admittance, Y. With this approach the effect of the ridges is assumed negligible but for the fact that they present a zero impedance to the E_ϕ field component. A further assumption is made such that,

provided there are sufficient corrugations per wavelength, the fields in each slot are deemed independant of z, the longitudinal direction of propagation, and only standing TM waves of the lowest order are present. The approximations improve as the number of slots per wavelength increases and the thickness of each ridge decreases.
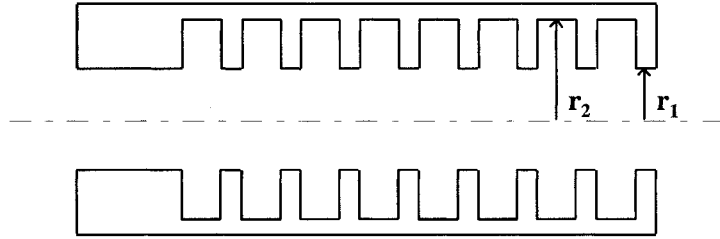
Figure 3.1 *Corrugated waveguide*

Although the majority of corrugated feeds take the form of conical structures, an excellent understanding of the way in which they operate can first be obtained by considering the corrugated waveguide of Figure 3.1. Indeed from the aperture theory developed in Appendix 1, the analysis undertaken for the cylindrical structure can easily be applied, with the addition of a phase correction factor, to horns with modest semi-flare angles with considerable success [3.6].

3.2 Modal analysis of cylindrical corrugated waveguide

From Chapter 2 the form of the fields in the inner region are given by Equations 2.10-2.12 with $\varepsilon = \varepsilon_0$ and $\mu = \mu_0$. To specify them fully requires k_z and $\overline{\Lambda}$, as defined in Equation 2.18 and 2.20, to be determined from knowledge of the normalised surface reactances, $\overline{Z}$ and $\overline{Y}$, at $r = r_1$. Applying the boundary condition

that imposes continuity of the tangential field components (E_z, H_z, E_ϕ and H_ϕ) at the surface $r = r_1$ allows $\overline{Z}$ and $\overline{Y}$ to be specified in terms of the fields in the outer region as described below.

From the assumption that only TM standing waves are present in the slots (for which $k_z = 0$, hence $k_\rho = k_0$), solutions to the wave equation for the axial field components in the outer region, assuming a time dependence $e^{j\omega t}$, are given by

$$E_{z_2} = \left[A_m J_m(k_0 r) + B_m N_m(k_0 r) \right] e^{-jm\phi} \tag{3.1}$$

$$H_{z_2} = 0 \tag{3.2}$$

Applying the boundary conditions $E_{z_2} = 0$ at $r = r_2$, it follows that

$$\left[A_m J_m(k_0 r_2) + B_m N_m(k_0 r_2) \right] = 0$$

from which

$$B_m = -\frac{J_m(k_0 r_2)}{N_m(k_0 r_2)} A_m$$

Equation 3.1 can then be rewritten as

$$E_{z_2} = c_m \left[J_m(k_0 r) N_m(k_0 r_2) - N_m(k_0 r) J_m(k_0 r_2) \right] e^{-jm\phi} \tag{3.3}$$

where $c_m = \dfrac{A_m}{N_m(k_0 r_2)}$

Knowing the form of the axial field components and after the assumption that E_{ϕ_1} goes to zero on the ridges and cannot penetrate the slot, the form of the ϕ directed fields in the outer region are given by

$$E_{\phi_2} = 0 \tag{3.4}$$

$$H_{\phi_2} = c_m \frac{-j}{k_0} \omega \varepsilon_0 \left[J'_m(k_0 r) N_m(k_0 r_2) - N'_m(k_0 r) J_m(k_0 r_2) \right] e^{-jm\phi} \tag{3.5}$$

Inserting Equations 3.2 - 3.5 in Equation 2.2 and subsequently Equation 2.16 and 2.17, the normalised reactance characteristics presented by the slots at the boundary $r = r_1$ are given by

$$\overline{Z}_m = \frac{-j}{\eta_0} \frac{E_{\phi_2}}{H_{z_2}} = 0 \tag{3.6}$$

$$\overline{Y}_m = -j\eta_0 \frac{H_{\phi_2}}{E_{z_2}} = \left[\frac{J'_m(k_0 r) N_m(k_0 r_2) - N'_m(k_0 r) J_m(k_0 r_2)}{J_m(k_0 r) N_m(k_0 r_2) - N_m(k_0 r) J_m(k_0 r_2)} \right] \Bigg|_{r=r_1} \tag{3.7}$$

Replacing Equation 3.6 and 3.7 in Equation 2.18 and 2.19, the characteristic equation for k_z in corrugated waveguide is obtained as

$$\left(m\overline{k}_z \right)^2 = F_m \left(k_{\rho_1} r_1 \right) \left[F_m \left(k_{\rho_1} r_1 \right) - \frac{\left(k_{\rho_1} r_1 \right)^2}{k_0 r_1} \overline{Y}_m \left(k_0 r_1 \right) \right] \tag{3.8}$$

and the equation for $\overline{\Lambda}$ obtained as

$$\overline{\Lambda}^2 - \overline{\Lambda} \frac{\left(\dfrac{(k_{\rho_1} r_1)^2}{k_0 r_1} \right) \overline{Y}_m(k_0 r_1)}{m\overline{k}_z} = 1 \tag{3.9}$$

where the solution is given by Equation 2.20 with

29

$$\Psi = \frac{(k_\rho r_1)^2}{k_0 r_1} \frac{1}{\overline{k}_z m} \overline{Y}_m (k_0 r_1)$$

(3.10)

With means of determining $\overline{k}_z$ and $\overline{\Lambda}$ it is possible to identify the physical conditions for low crosspolarisation and related to this, equal E and H-plane patterns, as defined by Equation 2.23 for $\overline{k}_z$ and Equation 2.24 for $\overline{\Lambda}$.

With a view to establishing appropriate design criteria, Equation 3.8 can be solved iteratively for $\overline{k}_z$ to determine the propagation characteristics of a specific corrugated geometry. Figure 3.2 illustrates the variation in $k_z r_1$ versus $k_0 r_1$ for the first four modes in waveguide typical of the aperture of a horn. It is evident that for the dominant HE$_{11}$ mode, as the size of the aperture in wavelengths increases, $k_z r_1 \rightarrow k_0 r_1$ for which $\overline{k}_z \rightarrow 1$. Equation 2.23 is therefore true to a good approximation when

$$k_0 r_1 >> 1$$

(3.11)

which is satisfied provided $r_1 \geq 1.5\lambda_0$, a condition valid for the majority of horn antennas.

The aperture being sufficiently large, as in Equation 3.11, can be considered as design criteria Number 1.
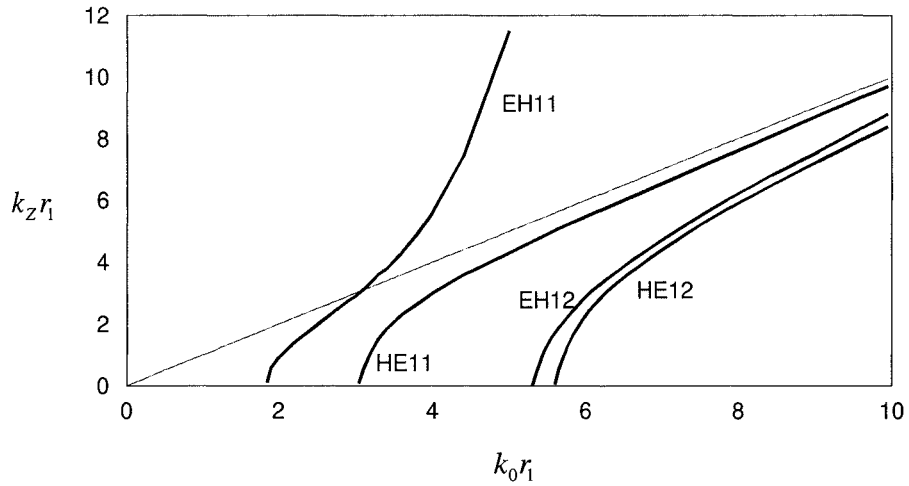
Figure 3.2 *Dispersion characteristics for corrugated waveguide*

From Figure 3.2 it is noticeable that the first mode to be excited does not propagate in the same manner as the other three. This is the mode that exists when the surface admittance appears inductive [3.7]. Dragone [3.8] calls this the surface wave mode since the field is confined to the region close to the wall and decays quickly away from it. However, Clarricoats and Saha [3.2] proposed the name EH_{11} mode and since this is in more widespread use, it is the term employed here. For later discussion it should be observed that in corrugated waveguide the first mode for which $\overline{\Lambda} = +1$ under balanced conditions, labelled HE_{11} in Figure 3.2, is actually the second mode with order $m = 1$ to be excited.

With Equation 3.11 and therefore the condition $\overline{k}_z \rightarrow 1$ being considered true for most practical horn designs, the form of the aperture field distribution is set largely by $\overline{\Lambda}$. It is evident from Equation 3.9 that $\overline{\Lambda} = \pm 1$ is satisfied when

$$\overline{Y}_m(k_0 r_1) = 0 \qquad\qquad (3.12)$$

To determine the physical significance of Equation 3.12 it is advantageous to invoke the large argument approximations for the Bessel functions [3.2], this being consistent with Equation 3.11. On doing so Equation 3.7 reduces to

31

$$\overline{Y} = -\cot[k_0 d]$$
(3.13)

where $d = r_2 - r_1$. Equation 3.12 is satisfied when $k_0 d = \pi/2$ in Equation 3.13, which implies a slot depth $d = \lambda/4$, a most important result in the design of corrugated horns.

The depth of the corrugation needing to be $\lambda/4$ can be considered as design criteria Number 2.

For a sufficiently large aperture and under the balanced hybrid condition when $\overline{\Lambda} = +1$, Equation 3.8 reduces to

$$F_1\left(k_{\rho_1} r_1\right) \approx \mp 1$$
(3.14)

for which, from Equation 2.13, the solutions are $J_0\left(k_{\rho_1} r_1\right) = 0$ and $J_2\left(k_{\rho_1} r_1\right) = 0$, corresponding to the HE_{1n} and EH_{1n} modes respectively. The eigenvalue for the HE_{11} mode under balanced hybrid conditions in corrugated waveguide is therefore approximated as

$$k_{\rho_1} r_1 \approx 2.405$$
(3.15)

Solutions of $J_0(2.405) = 0$ are sometimes used to represent the copolar field distribution in corrugated waveguide and whilst this offers substantial simplifications, care should be taken for conditions when $\overline{Y} \neq 0$, as illustrated in Figure 3.3, where it is demonstrated how the approximate eigenvalue differs from that obtained with the surface impedance model.

This point has been emphasised in [3.9] with use of a more accurate model incorporating space harmonics where the same discussion provides further justification for the use of the constant surface impedance model used here, following good agreement with the more accurate space harmonic method.
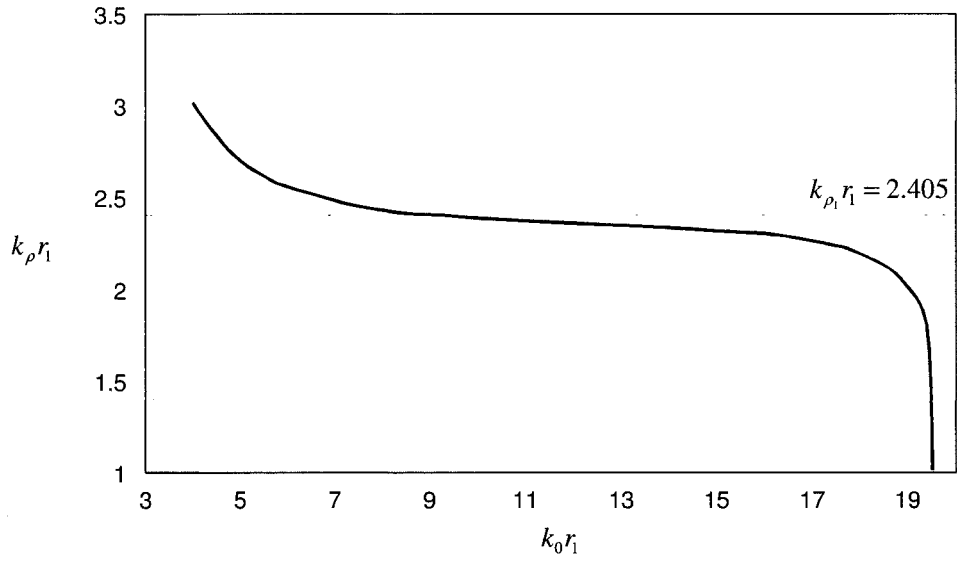
Figure 3.3 *Variation in radial vs freespace wavenumbers.* $\overline{Y} = 0$ *at* $k_0 r_1 = 10$

More significant to the behaviour of the field distribution is the frequency variation of the hybrid factor, $\overline{\Lambda}$, as illustrated in Figure 3.4, again for the HE_{11} mode.
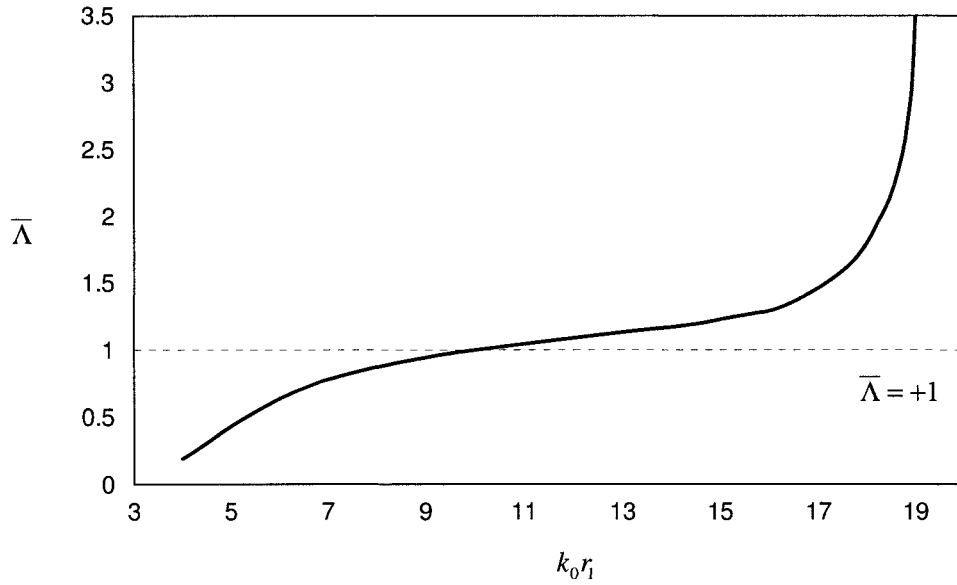
Figure 3.4 *Variation in hybrid factor vs* $k_0 r_1$. $\overline{Y} = 0$ *at* $k_0 r_1 = 10$

Note the condition $\overline{Y} = 0$ *at* $k_0 r_1 = 10$, for which these parameters are evaluated, is chosen as being representative of the size of the aperture of typical horn antennas.

With the useful crosspolar bandwidth being determined primarily by the frequency range over which $\overline{\Lambda}$ does not deviate appreciably from its optimum value of unity, and the conditions for low crosspolarisation being synonymous with good pattern symmetry, the slow variation of the function plotted in Figure 3.4 suggests the corrugated guide offers potentially good performance over a significant bandwidth. The general shape of the graph is only to be expected after demonstrating the admittance, $\overline{Y}$, varies as the cotangent of the argument as in Equation 3.13.

In order to develop this point further, and making use of the internal field characteristics developed so far, it is now useful to examine the radiation characteristics of corrugated waveguide.

3.3 Radiation characteristics

With a view to examining the radiation characteristics in the context of a practical horn design for a reflector antenna, the following discussions centre on the performance of a corrugated horn of modest flare angle and relatively small aperture. However, it is anticipated the conclusions will extend to a wide range of horn geometries.

Of particular interest is the frequency behaviour of the radiated crosspolarisation as plotted in Figure 3.5, for a horn where the slot depth is chosen to yield $\overline{Y} = 0$ at $f/f_0 - 1 = 0$ and $k_0 r_1 = 10$. The shaded regions represent the operating bands of interest for commercial Ka band systems.
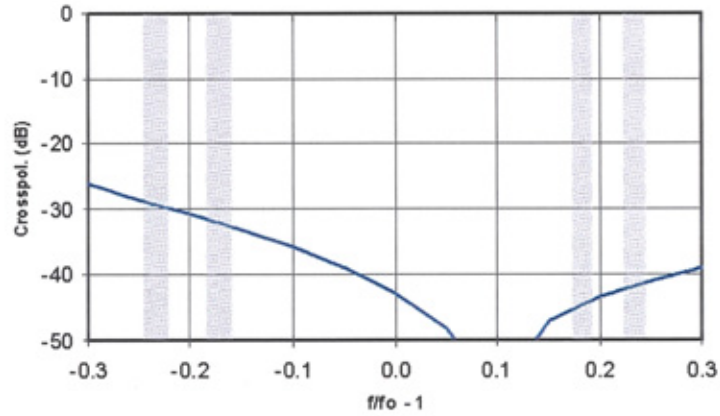
Figure 3.5 *Peak crosspol vs normalized frequency (HE$_{11}$ mode only).*
Slot depth chosen to yield Y=0 at f/f$_0$ – 1 = 0 and $k_0 r_1 = 10$

Notice how the response is not centred about f_0 and is also not symmetrical, highlighting the influence of the electrical aperture size as the frequency varies. The frequency response is generally more symmetrical for larger aperture sizes and centred closer to f_0.

Increasing the slot depth by approximately 15% yields the crosspolar response as in Figure 3.6, for which, at the limits of the operational band corresponding to f/f_0-1 = ±0.24, the crosspolar level is now balanced.

A further justification of increasing the corrugation slot depth in a practical horn is brought about by the marked improvement to the return loss at the lower edge of the operational band as a result of implementing this change.

35
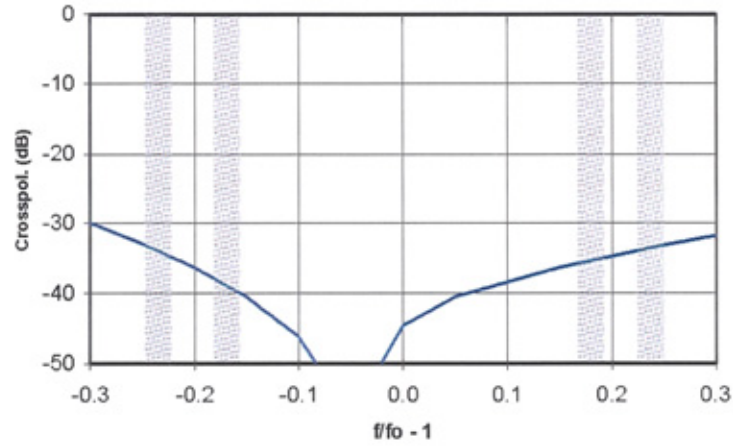
Figure 3.6 *Peak crosspol vs normalized frequency (HE₁₁ mode only).*
Slot depth chosen to yield Y=0 at f/f₀ − 1 = -0.15

By way of the modal analysis presented so far and with the addition of a spherical phase cap to account for the horn flare angle [Appendix 1], Figure 3.7 indicates the co-and crosspolar patterns, calculated by way of the Fourier Transform method [Appendix 1], at the limits of the 20/30GHz operational band. The corrugated horn appears to offer good performance with peak crosspolar values of better than -32dB together with reasonable pattern symmetry.

However, whilst this simple analytical technique provides a valuable means by which to study the fundamental principles of the corrugated horn, when considering the subtleties of their operation over such an extended bandwidth, further scrutiny of the assumptions made throughout the analysis is required.

(a)

(b)
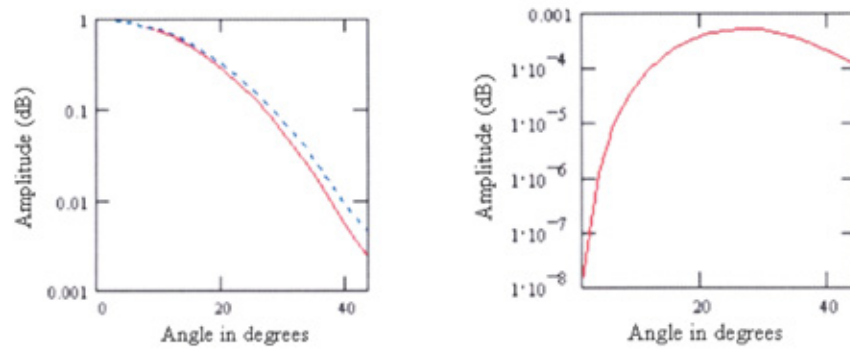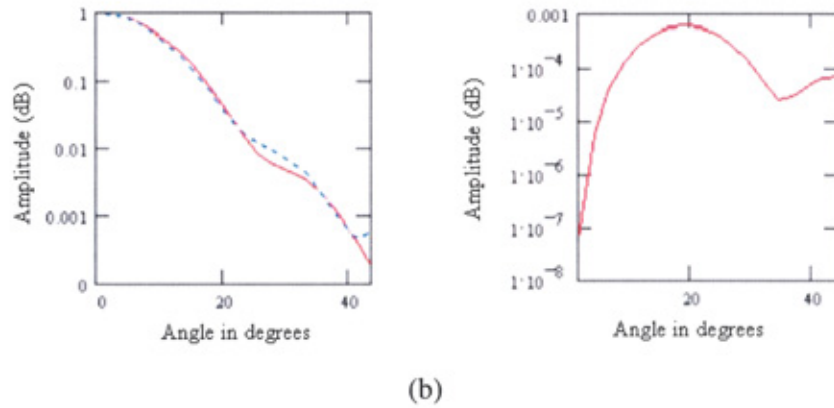
Figure 3.7 *Co- and crosspolar radiation patterns at a)* $f/f_0-1 = -0.24$ *and b)* $f/f_0-1 = +0.24$. *(HE$_{11}$ mode only). Slot depth chosen to yield Y=0 at* $f/f_0 - 1 = -0.15$

3.4 Limitations of the modal analysis

Inevitably, the accuracy of the modal analysis is subject to the validity of the various approximations associated with the way in which the boundary value problem is evaluated. By describing the corrugated boundary in terms of a constant surface reactance, no account is taken of the periodicity or exact geometry of the corrugations and, more significantly, no account is taken of the effect of higher order modes that may be generated within the horn.

Although Dragone [3.3] has suggested modifications to Equation 3.13 to account for the corrugation geometry, it is the assumption that only the HE$_{11}$ mode is present in the aperture that yields the greatest potential for error to the modal analysis presented here. In a practical horn the rapid change in the surface reactance characteristics in the throat together with mode conversion as the energy propagates from the throat to the aperture can lead to the generation of higher order modes, which must be included in the analysis if accurate predictions are to be made.

This has been studied by various researchers, again most notably Dragone [3.8] and Clarricoats [3.9]. By way of scattering analysis, Clarricoats developed the

propagation characteristics and subsequently the impact on radiation characteristics of higher order modes, such as EH_{12} and HE_{12}. If present, these have been shown to dominate crosspolar performance and degrade copolar pattern symmetry.

It is apparent that the useful bandwidth over which the corrugated horn can operate is set not only by the first order behaviour of the dominant HE_{11} mode but also the second order behaviour of higher order modes that inevitably occur in a practical horn design.

The effect of the exact corrugation geometry on mode content together with the need to account for these higher order modes to ensure accurate results has led to the development of more sophisticated analytical techniques such as Mode Matching [3.10, 3.11], Finite Difference-Time Domain (FD-TD) [3.12, 3.13] and Finite Element Method (FEM) [3.14], the FD-TD codes being employed in Chapter 7.

Nevertheless, the modal analysis presented in this chapter serves as a useful tool by which to explain the operation of the corrugated horn together with its potential for good crosspolar performance. In addition to providing important initial design criteria, it also provides a means with which to predict copolar patterns accurately and crosspolar patterns satisfactorily, provided the higher order mode content does not dominate. This will be developed further in Chapter 6 where the presence of higher order modes is examined in the context of a new dual-band horn.

Further discussion as to the practical limitations and the implementation of the corrugated horn are reserved for Chapter 7 when its performance is compared with the equivalent dielectrically-loaded horn, discussed in Chapter 4, together with a new horn design, as described in Chapter 6.

3.5 References

[3.1]   Kay, A.F.: *The Scalar Feed*, US AFCRL 64-347, AD60169, March 1964.

[3.2]   Clarricoats, P.J.B and Saha, P.K.: *Propagation and radiation behaviour of corrugated feeds Pt 1 and Pt2*, Proc. IEE, 1971, Vol. 118, pp 167-186.

[3.3]   Dragone, C.: *Characteristics of a broadband microwave corrugated feed: A comparison between theory and experiment*, Bell Syst. Tech. J., 1977, Vol. 56, pp 869-888.

[3.4]   Thomas, MacA. B.: *Design of corrugated conical horns*, IEEE Trans., 1978, AP-26, pp 367-372

[3.5]   Clarricoats, P.J.B., Dubrovka, R.F. and Olver, A.D.: *High performance compact corrugated horn*, IEE Proc., Dec 2004, A+P, Vol. 151, pp 519-24

[3.6]   Parini, C.G.: *Accurate prediction of cross-polar performance of narrow flare angle corrugated horns*, Int. URSI Symp. On EM Theory, Munich, Aug. 1980.

[3.7]   Thomas, MacA. B. and Minnett, H.C.: *Modes of propagation in cylindrical waveguides with anisotropic walls*, Proc. IEE, 1978, Vol. 125, p 929.

[3.8]   Dragone, C.: *Reflection, transmission and mode conversion in a corrugated feed*, Bell Syst. Tech. J., 1977, Vol. 56, pp 835-867.

[3.9]   Clarricoats, P.J.B., Olver, A.D.: *Corrugated horns for microwave antennas*, IEE Electromagnetic Wave Series, Vol 18, 1984.

[3.10] James, G.L.: *Analysis and design of TE11-to-HE11 corrugated cylindrical waveguide mode converters*, IEEE Trans., 1981, MTT-29, pp 1059-66.

[3.11] Raghaven, K.: *Modal matching technique applied to dielectric-loaded and smooth-walled conical horns*, Report, 1986, Dept. of Electrical and Electronic Eng., Queen Mary College, London.

[3.12] Gwarek, W.K.: *V2DE Solver*, FD-TD code for EM analysis of axisymmetrical antennas. Developed at Warsaw Polytechnic, Poland, 1995.

[3.13] *Microwave Studio* by CST – www.cst.de

[3.14] *HFSS* by Ansoft – www.ansoft.com

Chapter 4

Modal analysis of Dielectric-Loaded Waveguide

An alternative to the corrugated horn, which has received much attention [4.1, 4.2 et al], is the dielectric-loaded horn as illustrated in Figure 4.1.

It is made up of a smooth-walled metal horn, loaded with a core of dielectric material which itself is surrounded by an annulus of differing dielectric material such that there is a 'soft' discontinuity at the boundary of the inner and outer dielectric.

The concept and benefits of loading a smooth-walled horn were discovered almost by accident with the use of foam fillers to provide greater environmental protection against water ingress and condensation. It was noticed that certain forms and shapes of the inserts resulted in improved polarisation purity. Further investigations have subsequently shown the dielectric-loaded horn to offer the potential for wider band performance than the equivalent corrugated horn as discussed in this chapter.

The analysis follows that of [4.3] but it is noted that this subject has been preceded with related work from a great many authors including Beam and Wachowski [4.4], Kharadly and Lewis [4.5] and Clarricoats and Salema [4.6].
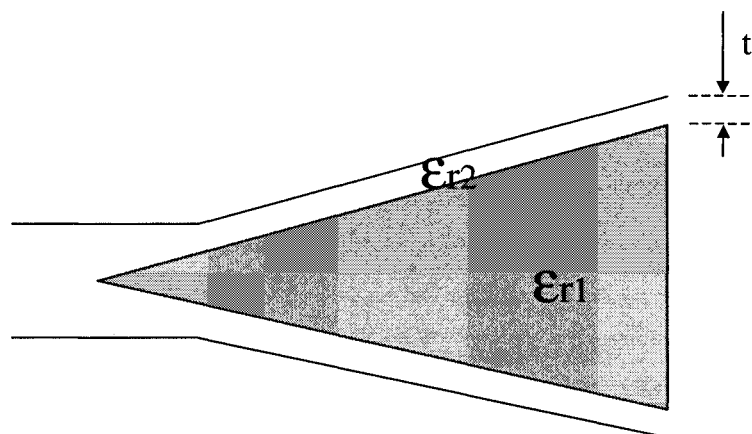
Figure 4.1 *Example of dielectric-loaded horn*

4.1 Principle of operation

The principle of operation can be explained by considering the interface between two media with distinctly different permitivities. For the planar interface illustrated in Figure 4.2, the amplitude coefficients of the incident wave in region 1 represent either TM to z and TE to z waves respectively. Interaction at the boundary causes some of the energy to be transmitted into region 2 while some is reflected back into region 1. Mahmoud [4.7] has shown that the reflected wave amplitudes in region 1 due to an incident TE to z wave are related through

$$E_r = R_e E_i + X\eta_1 H_i \qquad (4.1)$$

and through

$$H_r = -X\eta_1^{-1} E_i + R_h H_i \qquad (4.2)$$

for an incident TM to z wave. R_e, R_h and X are complex functions dependant on the surface reactance characteristics as set by the relative media properties, waveguide dimensions and frequency of operation.
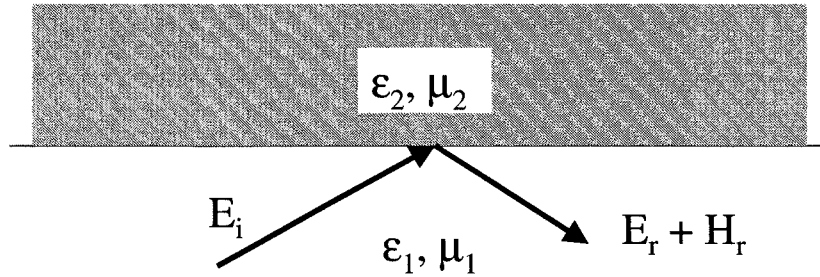
Figure 4.2 *Soft boundary interaction*

Equation 4.1 and 4.2 reveal that the TE and TM waves are somehow coupled by the interface of the two media and that an incident TE wave gives rise to reflected TE and TM waves of corresponding order and vice-versa. This concept can be extended to a cylindrical or conical interface as in the case of the dielectric loaded waveguide and the dielectric loaded horn respectively. As with the corrugated waveguide, by choosing the correct geometry it is possible to excite the required combination of TE_{11} and TM_{11} modes, which propagate together over a wide range of frequencies to form the HE_{11} mode.

4.2 Modal analysis of cylindrical dielectric-loaded waveguide

The form of the fields in the inner region are given by eqn 2.10 – 2.12 with suitable values of ε_1 and μ_1 depending on the properties of the dielectric material. In the outer region, unlike in the corrugated guide, both E_z and H_z components are present and solutions to Equation 2.3 take the form

$$E_{z_2} = \left[A_m J_m \left(k_{\rho_2} r \right) + B_m N_m \left(k_{\rho_2} r \right) \right] e^{-jm\phi} \tag{4.3}$$

$$H_{z_2} = \left[C_m J_m \left(k_{\rho_2} r \right) + D_m N_m \left(k_{\rho_2} r \right) \right] e^{-jm\phi} \tag{4.4}$$

where $k_{\rho_2}^2 = k_2^2 - k_z^2$ (assuming the system is lossless).

Applying the boundary conditions $E_z = 0$ and $\partial H_z / \partial r = 0$ at the waveguide wall, $r = r_2$, it follows that

$$\left[A_m J_m \left(k_{\rho_2} r \right) + B_m N_m \left(k_{\rho_2} r \right) \right] = 0 \Big|_{r=r2} \tag{4.5}$$

$$\left[C_m J_m' \left(k_{\rho_2} r \right) + D_m N_m' \left(k_{\rho_2} r \right) \right] = 0 \Big|_{r=r2} \tag{4.6}$$

42

from which

$$B_m = -\frac{J_m(k_{\rho_2} r_2)}{N_m(k_{\rho_2} r_2)} A_m$$

$$D_m = -\frac{J_m'(k_{\rho_2} r_2)}{N_m'(k_{\rho_2} r_2)} C_m$$

Equation 4.3 and 4.4 can then be rewritten as

$$E_{z_2} = c_m \left[J_m(k_{\rho_2} r) N_m(k_{\rho_2} r_2) - N_m(k_{\rho_2} r) J_m(k_{\rho_2} r_2) \right] e^{-jm\phi} \qquad (4.7)$$

$$H_{z_2} = d_m \left[J_m(k_{\rho_2} r) N_m'(k_{\rho_2} r_2) - N_m(k_{\rho_2} r) J_m'(k_{\rho_2} r_2) \right] e^{-jm\phi} \qquad (4.8)$$

where $\quad c_m = \dfrac{A_m}{N_m(k_{\rho_2} r_2)}$, and $\quad d_m = \dfrac{C_m}{N_m'(k_{\rho_2} r_2)}$

Using the expansion of Maxwell's equations, the form of the transverse field components in the outer region are subsequently given by

$$E_{\phi_2} = \frac{1}{k_{\rho_2}^2} \left[j\omega\mu_2 d_m k_{\rho_2} L_m^N(k_{\rho_2} r) - \frac{k_z}{r} c_m m M_m^D(k_{\rho_2} r) \right] e^{-jm\phi}$$

$$E_{\rho_2} = -\frac{1}{k_{\rho_2}^2} \left[\frac{\omega\mu_2}{r} d_m m L_m^D(k_{\rho_2} r) + jk_z c_m k_{\rho_2} M_m^N(k_{\rho_2} r) \right] e^{-jm\phi}$$

$$\qquad (4.9)$$

$$H_{\phi_2} = -\frac{1}{k_{\rho_2}^2} \left[\frac{k_z}{r} d_m m L_m^D(k_{\rho_2} r) + j\omega\varepsilon_2 c_m k_{\rho_2} M_m^N(k_{\rho_2} r) \right] e^{-jm\phi}$$

$$H_{\rho_2} = -\frac{1}{k_{\rho_2}^2} \left[jk_z d_m k_{\rho_2} L_m^N(k_{\rho_2} r) - \frac{\omega\varepsilon_2}{r} c_m m M_m^D(k_{\rho_2} r) \right] e^{-jm\phi}$$

where

$$L_m^N\left(k_{\rho_2}r\right) = J_m'\left(k_{\rho_2}r\right)N_m'\left(k_{\rho_2}r_2\right) - N_m'\left(k_{\rho_2}r\right)J_m'\left(k_{\rho_2}r_2\right)$$

$$L_m^D\left(k_{\rho_2}r\right) = J_m\left(k_{\rho_2}r\right)N_m'\left(k_{\rho_2}r_2\right) - N_m\left(k_{\rho_2}r\right)J_m'\left(k_{\rho_2}r_2\right)$$

$$M_m^N\left(k_{\rho_2}r\right) = J_m'\left(k_{\rho_2}r\right)N_m\left(k_{\rho_2}r_2\right) - N_m'\left(k_{\rho_2}r\right)J_m\left(k_{\rho_2}r_2\right)$$

$$M_m^D\left(k_{\rho_2}r\right) = J_m\left(k_{\rho_2}r\right)N_m\left(k_{\rho_2}r_2\right) - N_m\left(k_{\rho_2}r\right)J_m\left(k_{\rho_2}r_2\right)$$

At the boundary $r = r_1$ the tangential field components are continuous, to be consistent with Snell's law. Making use of all the z directed field components (Equation 2.10, 2.11, 4.7 and 4.8) and applying the boundary condition $E_{z_1} = E_{z_2}$ and $H_{z_1} = H_{z_2}$, allows the amplitude coefficients c_m and d_m to be expressed in terms of a_m and b_m such that

$$c_m = a_m \left. \frac{J_m\left(k_{\rho_1}r\right)}{M_m^D\left(k_{\rho_2}r\right)}\right|_{r=r_1} \tag{4.10}$$

$$d_m = b_m \left. \frac{J_m\left(k_{\rho_1}r\right)}{L_m^D\left(k_{\rho_2}r\right)}\right|_{r=r_1} \tag{4.11}$$

Furthermore, since Equation 2.9 expresses b_m in terms of a_m, Equation 4.11 can be rewritten as

$$d_m = j\frac{a_m}{\eta_1}\bar{\Lambda}\left. \frac{J_m\left(k_{\rho_1}r\right)}{L_m^D\left(k_{\rho_2}r\right)}\right|_{r=r_1} \tag{4.12}$$

Substituting Equation 4.10 and 4.12 in Equations 4.7 – 4.9, the form of the fields at the boundary surface, $r = r_1$, can be expressed in terms of the arbitrary constant a_m, with $\bar{k}_z$ and $\bar{\Lambda}$ unknowns, as

$$E_{z_2} = a_m J\left(k_{\rho_1} r_1\right) e^{-jm\phi}$$

$$H_{z_2} = ja_m \bar{\Lambda} \eta_1^{-1} J\left(k_{\rho_1} r_1\right) e^{-jm\phi}$$

$$E_{\phi_2} = -a_m G_2 \left[\frac{\mu_2}{\mu_1} \bar{\Lambda}\left(k_{\rho_2} r\right) \frac{L_m^N\left(k_{\rho_2} r\right)}{L_m^D\left(k_{\rho_2} r_1\right)} + \bar{k}_z m \right] e^{-jm\phi}$$

$$H_{\phi_2} = -ja_m \eta_1^{-1} G_2 \left[\bar{k}_z m \bar{\Lambda} + \frac{\varepsilon_2}{\varepsilon_1}\left(k_{\rho_2} r\right) \frac{M_m^N\left(k_{\rho_2} r\right)}{M_m^D\left(k_{\rho_2} r_1\right)} \right] e^{-jm\phi}$$

(4.13)

$$E_{\rho_2} = -ja_m G_2 \left[\frac{\mu_2}{\mu_1} \bar{\Lambda} m + \bar{k}_z\left(k_{\rho_2} r\right) \frac{M_m^N\left(k_{\rho_2} r\right)}{M_m^D\left(k_{\rho_2} r_1\right)} \right] e^{-jm\phi}$$

$$H_{\rho_2} = a_m \eta_1^{-1} G_2 \left[\bar{k}_z \bar{\Lambda}\left(k_{\rho_2} r\right) \frac{L_m^N\left(k_{\rho_2} r\right)}{L_m^D\left(k_{\rho_2} r_1\right)} + \frac{\varepsilon_2}{\varepsilon_1} m \right] e^{-jm\phi}$$

where $\bar{k}_z = \dfrac{k_z}{k_1}$ and $G_2 = \dfrac{k_1 r}{\left(k_{\rho_2} r\right)^2} J_m\left(k_{\rho_1} r_1\right)$.

Following the general procedure in Chapter 2, the surface reactances can now be specified by substituting the relevant equations from Equation 4.13 into Equation 2.2. Adopting the normalised forms, as defined by eqn 2.16 and 2.17, expressions for the impedance and admittance are given by

$$\overline{Z} = \frac{k_1 r}{\left(k_{\rho_2} r\right)^2} \left[\frac{\overline{k}_z m}{\overline{\Lambda}} + k_{\rho_2} r \frac{\mu_1}{\mu_2} \frac{L_m^N\left(k_{\rho_2} r\right)}{L_m^D\left(k_{\rho_2} r\right)} \right]_{r=r1} \tag{4.14}$$

$$\overline{Y} = \frac{k_1 r}{\left(k_{\rho_2} r\right)^2} \left[\overline{k}_z m \overline{\Lambda} + k_{\rho_2} r \frac{\varepsilon_2}{\varepsilon_1} \frac{M_m^N\left(k_{\rho_2} r\right)}{M_m^D\left(k_{\rho_2} r\right)} \right]_{r=r1} \tag{4.15}$$

Substituting Equation 4.14 and 4.15 into Equation 2.14 and 2.15 respectively, yields two alternative expressions for $\overline{\Lambda}$

$$\overline{\Lambda}^{-1} = \frac{1}{m \overline{k}_z} \frac{F_m\left(k_{\rho_1} r_1\right) - \frac{\left(k_{\rho_1} r_1\right)^2}{\left(k_{\rho_2} r_1\right)^2} \overline{L}_m\left(k_{\rho_2} r_1\right)}{\frac{\left(k_{\rho_1} r_1\right)^2}{\left(k_{\rho_2} r_1\right)^2} - 1} \tag{4.16}$$

$$\overline{\Lambda} = \frac{1}{m \overline{k}_z} \frac{F_m\left(k_{\rho_1} r_1\right) - \frac{\left(k_{\rho_1} r_1\right)^2}{\left(k_{\rho_2} r_1\right)^2} \overline{M}_m\left(k_{\rho_2} r_1\right)}{\frac{\left(k_{\rho_1} r_1\right)^2}{\left(k_{\rho_2} r_1\right)^2} - 1} \tag{4.17}$$

where

$F_m\left(k_{\rho_1} r_1\right)$ is defined in Equation 2.13,

$$\overline{L}_m\left(k_{\rho_2} r_1\right) = \frac{\mu_1}{\mu_2} k_{\rho_2} r \frac{L_m^N\left(k_{\rho_2} r\right)}{L_m^D\left(k_{\rho_2} r\right)} \bigg|_{r=r_1} \tag{4.18}$$

$$\overline{M}_m\left(k_{\rho_2} r_1\right) = \frac{\varepsilon_2}{\varepsilon_1} k_{\rho_2} r \frac{M_m^N\left(k_{\rho_2} r\right)}{M_m^D\left(k_{\rho_2} r\right)} \bigg|_{r=r_1} \tag{4.19}$$

Now the characteristic equation is obtained by equating Equation 4.16 to 4.17, yielding

$$\left(m\,\overline{k}_z\right)^2\left[\frac{\left(k_{\rho_1}r_1\right)^2}{\left(k_{\rho_2}r_1\right)^2}-1\right]^2 = \left[F_m\left(k_{\rho_1}r_1\right)-\frac{\left(k_{\rho_1}r_1\right)^2}{\left(k_{\rho_2}r_1\right)^2}\overline{L}_m\left(k_{\rho_2}r_1\right)\right]\left[F_m\left(k_{\rho_1}r_1\right)-\frac{\left(k_{\rho_1}r_1\right)^2}{\left(k_{\rho_2}r_1\right)^2}\overline{M}_m\left(k_{\rho_2}r_1\right)\right]$$

(4.20)

which can be solved iteratively to find the propagation constant $\overline{k}_z$ for a given structure where μ_1, ε_1, μ_2, ε_2, r_1 and r_2 are known, and ω is specified.

m is the azimuthal dependance for a given mode and for the circular, coaxial structures considered here $m = 1$ since only modes of the type HE_{1n} or EH_{1n} are excited due to the circular-symmetry of the geometries considered.

An equation for $\overline{\Lambda}$ is obtained by subtracting Equation 4.16 from 4.17 to give

$$\overline{\Lambda}-\overline{\Lambda}^{-1} = \frac{\dfrac{\left(k_{\rho_1}r_1\right)^2}{\left(k_{\rho_2}r_1\right)^2}\left[\overline{L}_m\left(k_{\rho_2}r_1\right)-\overline{M}_m\left(k_{\rho_2}r_1\right)\right]}{m\overline{k}_z\left[\dfrac{\left(k_{\rho_1}r_1\right)^2}{\left(k_{\rho_2}r_1\right)^2}-1\right]}$$

(4.21)

solutions of which are given by Equation 2.20 with

$$\Psi = \frac{\dfrac{\left(k_{\rho_1}r_1\right)^2}{\left(k_{\rho_2}r_1\right)^2}\left[\overline{L}_m\left(k_{\rho_2}r_1\right)-\overline{M}_m\left(k_{\rho_2}r_1\right)\right]}{m\overline{k}_z\left[\dfrac{\left(k_{\rho_1}r_1\right)^2}{\left(k_{\rho_2}r_1\right)^2}-1\right]}$$

(4.22)

In the outer region, $r_1 < r < r_2$, k_z can exceed k_2 away from cut-off. From the separation relationship $k_{\rho_2}^2 = k_2^2 - k_z^2$, when k_z exceeds k_2, k_{ρ_2} becomes imaginary

and the Bessel functions $J_m(k_{\rho_2} r)$ and $N_m(k_{\rho_2} r)$ are replaced by the modified Bessel functions $I_m(K_{\rho_2} r)$ and $K_m(K_{\rho_2} r)$, where $K_{\rho_2} = -jk_{\rho_2}$.

4.3 Design criteria

Having established the characteristic equations, it is possible to identify the conditions for which Equation 2.23 and 2.24 are satisfied in an effort to establish the required dimensions for optimum performance. To this end it is useful to plot the dispersion characteristics as illustrated in Figure 4.3 for a waveguide with dimensions typical of the aperture of a horn. For the dominant HE_{11} mode, $k_z r_1 \rightarrow k_1 r_1$ as the aperture size increases in wavelengths, hence $\bar{k}_z \rightarrow 1$ and Equation 2.24 appears to be satisfied under the condition

$$k_1 r_1 \gg 1 \tag{4.23}$$

which is true at the aperture for the majority of dielectric-loaded horn antennas in a similar manner to Equation 3.11 for corrugated horns.

Comparing Figure 4.3 with Figure 3.2 it is apparent that for the dielectric-loaded waveguide there is no surface wave mode and the first mode for which $\bar{\Lambda} = +1$ under balanced conditions is the first to be excited, unlike in the corrugated guide, where it is the second. This presents a problem for the nomenclature of the subsequent modes in dielectric-loaded guide since convention requires the second mode to be called the EH_{11} mode but this conflicts with the name given to the surface wave mode of the corrugated guide. Conversely, calling it the EH_{12} mode, as required to be consistent with the terminology for the corrugated guide, conflicts with the corresponding order of the root to the characteristic equation (Equation 4.20). While this problem will not be resolved here, attention is drawn to the potential confusion that could arise as a result of the inconsistency between the two nomenclatures. In this instance the second mode for the dielectric-loaded guide has been labelled EH_{11} and the third

HE_{12} and so on. Whichever terminolgy chosen, the name allocated to the first mode for which $\overline{\Lambda} = +1$ under balanced conditions in both types of waveguide is HE_{11}, and since other higher order modes are not examined here specifically, there should be little or no confusion throughout this discussion.
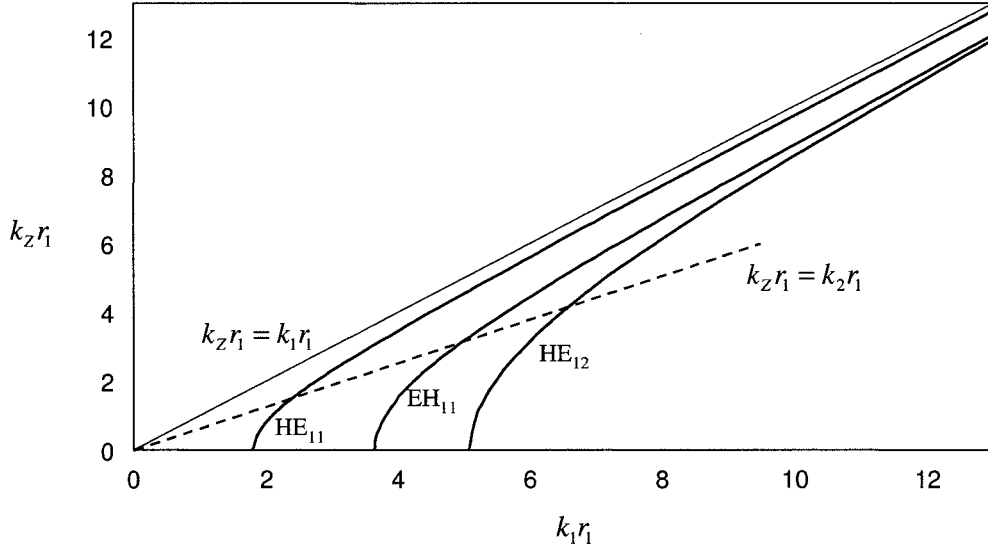
Figure 4.3 *Dispersion characteristics for dielectric-loaded waveguide* ($\varepsilon_r = 1.48$)

In addition to the requirement that $\overline{k}_z \to 1$, the aperture distribution is also set by the hybrid factor, $\overline{\Lambda}$, the requirement for copolar pattern symmetry and low crosspolarisation being dependant on satisfying Equation 2.24. On examination of Equation 4.21 it is evident Equation 2.24 is true under the condition

$$\overline{L}_m \left(k_{\rho_2} r_1 \right) = \overline{M}_m \left(k_{\rho_2} r_1 \right)$$

(4.24)

for which Equation 4.21 reduces to the balanced hybid condition, $\overline{\Lambda} = \pm 1$. Replacing the Bessel functions with the modified Bessel functions (as consistent with Figure 4.3) and invoking the large argument, asymptotic approximations for $\overline{L}$ and $\overline{M}$ (as

consistent with Equation 4.23), an equation for the optimum thickness, t^a, of the outer annulus, for the case where the outer dielectric is air, is obtained, following Lier [4.1],

$$t^a = \frac{1}{k_0} \tanh^{-1} \left[\frac{1}{\sqrt{\varepsilon_{r1}}} \right] \left[\frac{1}{\sqrt{\varepsilon_{r1} - 1}} \right] \qquad (4.25)$$

where k_0 is the freespace wavenumber, ε_r is the relative permitivity of the inner dielectric material and 'a' denotes asymptotic.

Figure 4.4 shows plots of $\overline{\Lambda}$ versus $k_1 r_1$ for the HE_{11} mode, with ε_r as a parameter. Comparing Figure 4.4 with Figure 3.4, it is immediately apparent the range over which $\overline{\Lambda}$ does not deviate appreciably from unity is greater for the dielectric-loaded guide than for the corrugated guide suggesting that it may offer superior crosspolar bandwidth performance. Referring back to Equation 4.25, this is only to be expected after the surface impedance of the dielectric-air interface was found to vary as the hyperbolic tangent function. This is a slow monotonically-varying function compared to the periodic tangent function through which the surface impedance of the corrugated boundary varies, as evident in Equation 3.13, and the bandwidth over which the crosspolarisation remains below a specified level can be expected to be wider for the dielectric-loaded case.
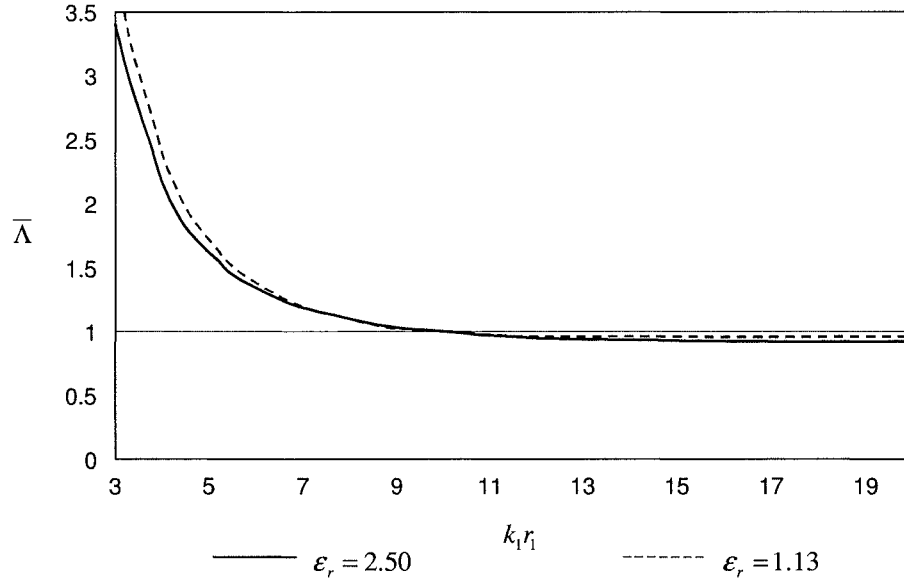
Figure 4.4 *Variation in* $\overline{\Lambda}$ *vs* $k_1 r_1$. $\overline{\Lambda} = +1$ *when* $k_1 r_1 = 10$

Notably, the air gap, t, surrounding the dielectric core for the calculations carried out in Figure 4.4 has been determined iteratively, using the cylindrical modal analysis rather than the asymptotic approximation, to yield $\overline{\Lambda} = +1$ when $k_1 r_1 = 10$ for each value of ε_r. By doing so, the variation in $\overline{\Lambda}$ is found to be almost independent of the dielectric constant. This is in contrast to results published by other authors [4.7] who have used asymptotic values of t when plotting equivalent graphs and concluded that wider crosspolar bandwidth can be achieved with use of materials having a higher dielectric constant. The results presented here suggest this not to be the case; Mahmoud's conclusions being more a reflection on the accuracy of the asymptotic approximation for the reactance characteristics of the dielectric-air interface.

With this in mind, it is noted that Equation 4.25 has been developed with use of the large argument approximations and its accuracy increases with increasing aperture size. A measure of its accuracy for a given aperture is the ratio, t^a / t^c, where values of t^c are obtained from numerical solutions to Equation 4.24 through the more accurate cylindrical modal analysis with values of $\overline{L}$ and $\overline{M}$ calculated using

Equation 4.18 and 4.19. Figure 4.5 compares t^a/t^c versus $k_1 r_1$ with the equivalent parameter for the corrugated guide, d^a/d^c, where d^a is the slot depth satisfying Equation 3.12 with $\overline{Y}$ given by Equation 3.13 and d^c is that satisfying Equation 3.12 with $\overline{Y}$ given by Equation 3.7. Although Equation 3.13 is not the true asymptotic form of eqn 3.7, it is the equation most often used in the design of corrugated horns and as such is a direct equivalent to Equation 4.25 for dielectric-loaded horns. It is therefore reasonable to compare the accuracy of each.
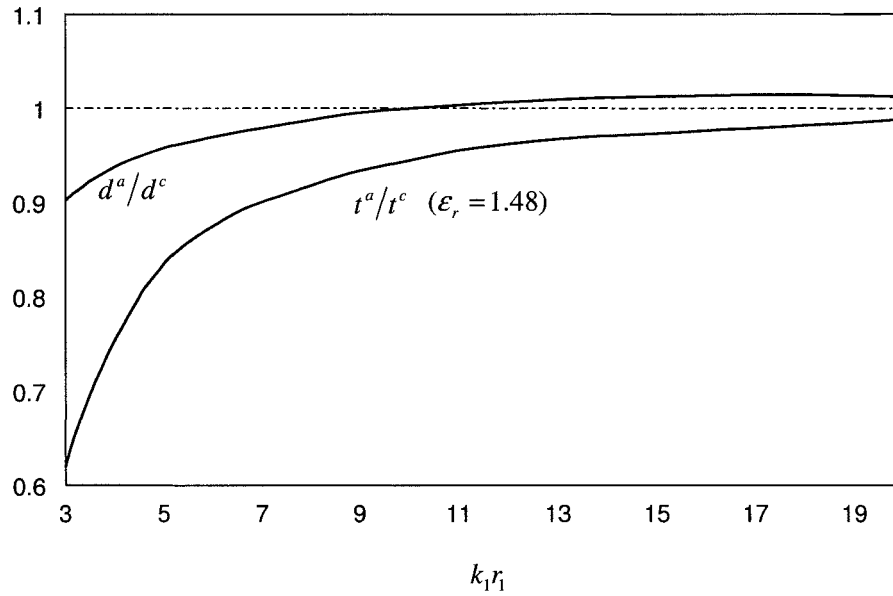
Figure 4.5 *Variation in the accuracy of the asymptotic approximation for the surface reactance characteristics of corrugated (d^a/d^c) and dielectric-loaded (t^a/t^c) waveguide vs aperture size. t^a and d^a calculated when $k_1 r_1 = 10$.*

For the corrugated guide, values of d obtained using the asymptotic model are in excellent agreement with those obtained using the cylindrical model, suggesting that

it lends itself more readily to simplifications brought about by asymptotic approximations, even for relatively small apertures.
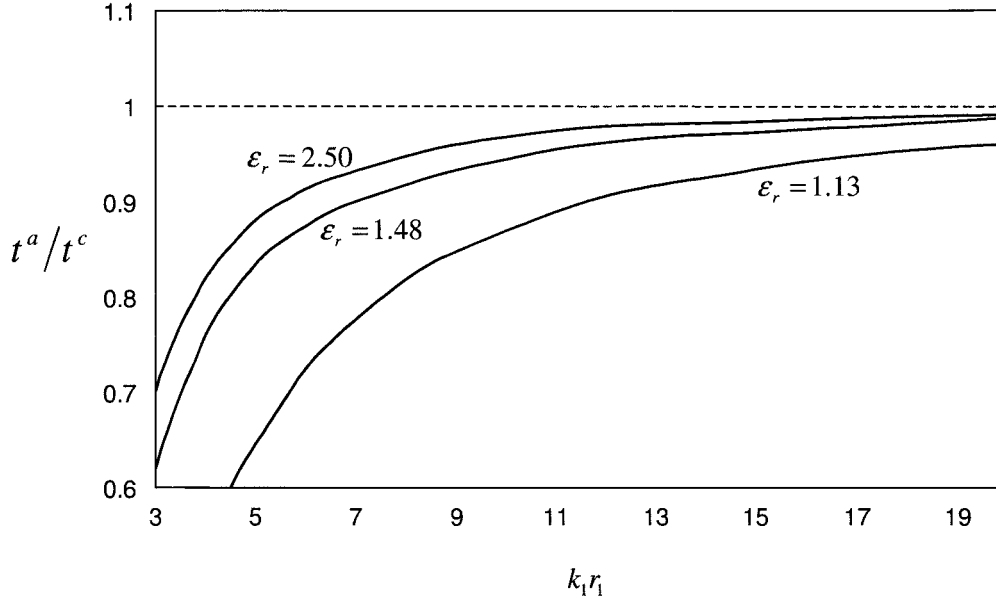
$$t^a/t^c$$

Figure 4.6 *Variation in the accuracy of the asymptotic approximation for the surface reactance characteristics of dielectric-loaded* (t^a/t^c) *waveguide vs aperture size with* ε_r *as a parameter.* t^a *calculated when* $k_1 r_1 = 10$.

Figure 4.6 compares t^a/t^c for three different values of ε_r where the different dielectric constants represent distinctly different materials. $\varepsilon_r = 1.13$ is typical of an expanded polystyrene foam (density $= 55\text{kg/m}^3$) as used extensively by Clarricoats and Olver and their co-workers at Queen Mary's College [4.2], $\varepsilon_r=2.5$ is typical of solid polystyrene as used by Lier [4.1]. $\varepsilon_r=1.48$ is typical of a rigid, polyurethane foam [4.8].

It appears that for the dielectric-guide, Equation 4.25 offers accurate solutions for aperture sizes typical of a horn feed when material of a relatively high permitivity is used, but for materials having lower values of ε_r the model breaks down.

From this, it is concluded the required air gap should be calculated with a technique more accurate than the asymptotic approximation, particularly for small horns and for those employing material with a low ε_r.

4.4 Radiation characteristics

In a horn of sufficiently large diameter such that $\overline{k}_z \to 1$, $k_{\rho_2} > k_{\rho_1}$ and consequently $k_{\rho_2}^2 \gg k_{\rho_1}^2$. Under this condition Equation 4.20 reduces to

$$F_1\left(k_{\rho_1} r_1\right) \approx \mp 1 \tag{4.26}$$

Equation 4.26 is the same as Equation 3.14 for the corrugated waveguide described in Chapter 3, from which it can be speculated the dielectric loaded waveguide has similar radiation characteristics [4.1, 4.9]. As with the corrugated guide, the asymptotic solution to the eigenvalue for the HE_{11} mode is given by $J_0\left(k_{\rho_1} r_1\right) = 0$ with $k_{\rho_1} r_1 = 2.405$. For the corrugated guide this was shown (Figure 3.3) to be a reasonable approximation to the solution obtained using the surface impedance model, especially when operating close to the balanced hybrid condition. However, for the dielectric-loaded waveguide, this is not the case as illustrated in Figure 4.4, from which it is evident the approximate eigenvalue differs considerably from that obtained with the surface impedance model. Indeed for typical values of t when $2.5 > \varepsilon_{r1} > 1.13$, $k_{\rho_1} r_1$ only approaches to within 5% of 2.405 when $k_1 r_1 \sqrt{\varepsilon_{r1} - 1} > 19$, a condition not often satisfied in conventional feed horns.

Interestingly, Equation 4.26 only requires the aperture size to be sufficiently large before being true and under such conditions is not dependant on the hybrid factor, $\overline{\Lambda}$. This is in contrast to the corrugated guide which requires both the aperture to be large and $\overline{\Lambda} \approx 1$. This is an important observation, since it suggests the performance of dielectric loaded waveguide of sufficiently large dimensions is only weakly

dependant on t, the size of air gap. Whilst this may be true for the condition when the HE_{11} mode is already established in a waveguide structure, experience has found the air gap to be more critical in the transitional region when converting from the TE_{11} in homogeneously-filled guide to the HE_{11} mode, as in the throat of a practical horn design.

In practice the optimum air gap must usually be found empirically or, as for the corrugated horn of Chapter 3, with techniques capable of including higher order modes in the analysis [4.3, 4.10].

The analysis here presents an important insight into the operation of the dielectrically-loaded horn and relates the physical parameters to electrical performance parameters to provide the reader with important design criteria.

Measured data for a practical example is presented in Chapter 7. Discussions on the practical limitations of the design are reserved for Chapter 8 when the dielectric-loaded horn is compared with that of the corrugated horn together with a novel, dual-band horn presented in Chapter 6.

4.5 References

[4.1]   Lier, E.: *A new hybrid-mode horn antenna – an alternative to the corrugated feed*, ELAB report STF44 A85064, The Norwegian Institute of Technology, Trondheim, Norway, 1985.

[4.2]   Olver, A.D., Clarricoats, P.J.B., Raghaven, K.: *Dielectric cone loaded horn antennas*, Proc. IEE, 1988, vol. 135, pp. 158-62.

[4.3]   Raghaven, K.: *Modal matching technique applied to dielectric-loaded and smooth-walled conical horns*, Report, 1986, Dept. of Electrical and Electronic Eng., Queen Mary College, London.

[4.4]   Beam, R.E. and Wachowski, H.M.: *Shielded dielectric-rod waveguides*, AIEE Trans., 1951, Vol. 70, pp874-80.

[4.5]   Kharadly, M.M.Z. and Lewis, J.E.: *Properties of dielectric-tube waveguides*, Proc. IEE, 1969, Vol. 116, No.2, pp 214-24.

[4.6]   Clarricoats, P.J.B. and Salema, C.E.R.C.: *Antennas employing conical dielectric horns. Pt I, Propagation and radiation characteristics of dielectric cones*, Proc. IEE, 1973, Vol. 120, pp 741-9.

[4.7]   Mahmoud, S.F.: *Electromagnetic Waveguides: theory and application*, London, Peregrinus Ltd, 1991.

[4.8]   GEC-Marconi Materials specification bulletin:
        Materials/990/DS/P10/A/4/91, radar transparent products, 1991.

[4.9]   Clarricoats, P.J.B.: *Theoretical comparison of crosspolar performance of dielectric and corrugated feeds*, Electronics letters, 1981, Vol. 17, No.9, pp 317-8.

[4.10] Tun, S.M., Philippou, G.Y. and Adatia, N.: *Analysis and design of rotationally symmetric dielectric loaded waveguides and horns*, ICAP Proc., 1987, pp 438-42.

Chapter 5

Illumination of elliptical reflector antennas – a critical issue

The advantage of both the corrugated and dielectric-loaded horn for antennas requiring low crosspolarisation has been well documented both here and in the literature. However, the consequences brought about by the resulting form of the copolar patterns in the context of a primary feed for a reflector antenna have received less attention, other than general observations regarding pattern symmetry and similarities to a Gaussian beam [5.1].

So far the discussions herein have been restricted to horn apertures of circular cross-section, largely because these represent the largest class of horns of this type; the resulting circularly symmetric copolar radiation pattern being well matched to reflector antennas having circular projected apertures, whether axisymmetric or offset antenna geometries.

However, in the high volume, consumer and small-to-medium enterprise market, there is now a growing trend to make use of antennas having elliptical, offset reflectors, thereby minimising the visual impact whilst maximising RF performance. In this chapter the advantages of elliptical, offset antennas together with the impact this has on the design of the feed horn are explored, particularly in the context of circular polarisation.

5.1 Advantages of elliptical reflector antennas

The advantages of elliptical, offset reflectors over circular, offset reflectors are largely two-fold. In particular they provide significantly improved sidelobe performance in the plane of the major axis of the ellipse. If, as part of the antenna alignment to the satellite, the major axis of the ellipse can be made to be parallel with the geostationary arc, adjacent satellite interference can be significantly reduced.

In addition they offer better scanning properties thereby increasing the potential for additional services from different satellite orbital locations to be delivered simultaneously through a common antenna by way of multiple feeds.

5.1.1 Sidelobe levels:

Figure 5.1 provides a comparison of the antenna radiation patterns in the plane of the major axis for offset reflectors having different values of E, the elliptical aspect ratio (defined as the ratio of the major and minor axes of the ellipse that forms the rim of the projected aperture of the reflector - denoted as d_2/d_1 in Figure 1.3). Notably, in each case the feed illumination is adjusted to suit the reflector-aperture shape to provide a nominal -10dB edge taper around the entire rim of the reflector. The projected-aperture area and focal length are kept constant.

With the projected-aperture area and illumination edge taper kept constant, the directivity is nominally unchanged. However, the beamwidth and sidelobe levels improve considerably with reference to adjacent satellite interference, as quantified in Figure 5.2.
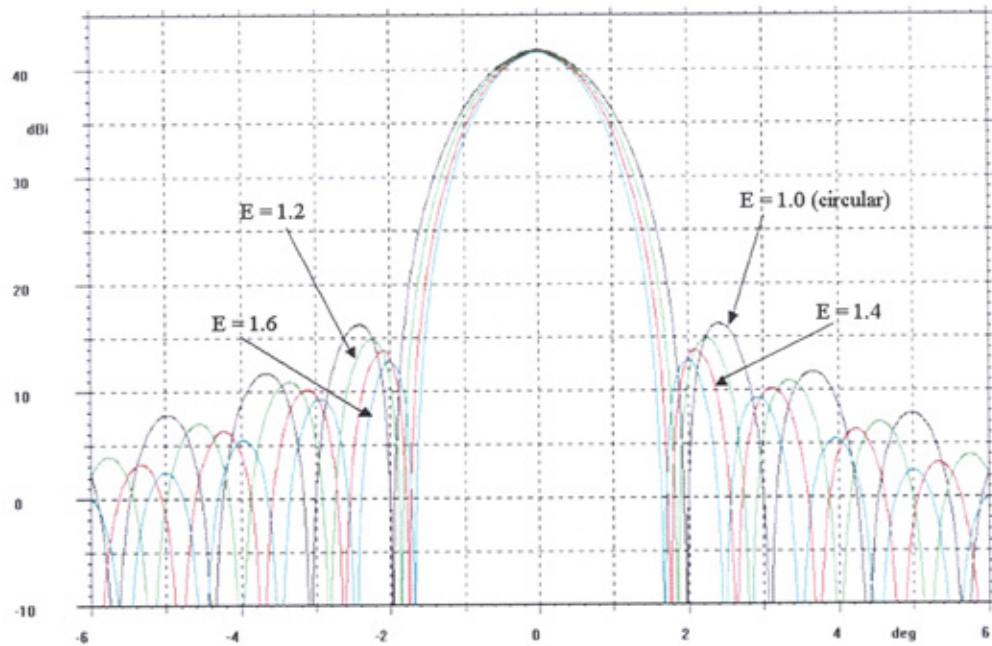
Figure 5.1 ±6° antenna radiation patterns in the plane of the major axis of the ellipse with E, the elliptical aspect ratio, as a parameter. Feed illumination adjusted in each case to provide −10dB edge taper around the entire rim of the reflector.
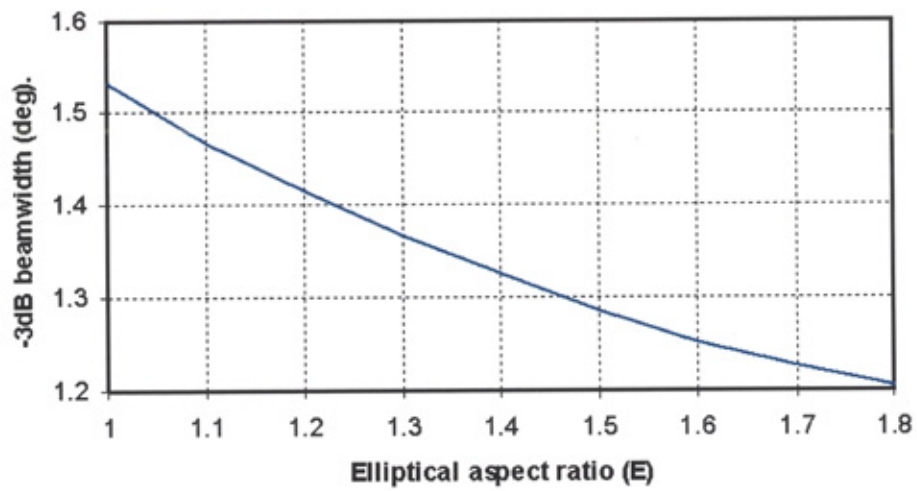
(a)
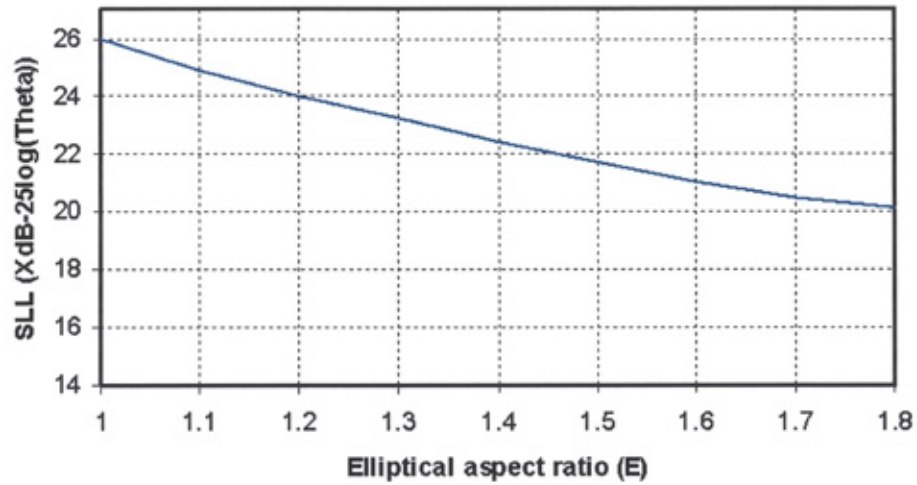
(b)

Figure 5.2 —3dB beamwidth (a) and sidelobe level (b) vs elliptical aspect ratio, E. Feed illumination adjusted for each value of E to provide —10dB edge taper at rim of reflector.

The Y-axis scale represents the value of XdB in the equaition $X - 25\log(\theta)$, where θ is the angle from boresight – a formula commonly used to quantify the sidelobe envelope in antennas for satellite communications

5.1.2 Scanning properties:

The discussion so far has centred on the performance of feeds placed at the focal point of a parabolic reflector. However, in the consumer and small-to-medium enterprise business there is an ever-growing demand to include additional services from different satellite orbital locations through a common antenna. Often there is a desire by the satellite operators to provide their customers with 2-way (Tx/Rx) data traffic from one satellite location together with 1-way (Rx-only) services from one, two or even three alternative satellite locations; all simultaneously.

Because the 2-way service is subject to stringent regulatory performance requirements (to avoid interfering with others in the Transmit mode), the feed horn for the 2-way application must be positioned at the focal point of the reflector to achieve optimum performance. The specifications for the 1-way services are much

less stringent and adequate performance can often be achieved with the use of scanned feeds.

Scanned feeds are additional feeds placed adjacent to the central, on-axis feed at a position whereby they are sensitive to signals from satellites at different orbital locations. The exact scanned feed position is dependent on the antenna optical geometry and the required angular scan between the on-axis satellite orbital location and the scanned satellite orbital location. For a given antenna geometry the performance of the scanned feed reduces as the angular scan increases.

With this in mind there is a need to find ways to improve the scanning properties of this type of antenna, particularly since it is the required performance of the outer-most scanned feed, rather than that of the on-axis 2-way feed, that can often dictate the antenna dimensions.

Herein lies the second major advantage of elliptical reflectors over the equivalent circular reflector. The optics are such that for a given projected aperture area and focal length, an elliptical reflector provides more gain and better adjacent satellite rejection properties for scanned feeds. Specifically, the elliptical optics causes the scanned performance to degrade less with increase in scan angle. This is illustrated in Figure 5.3 for an antenna with geometry typical of that used in the industry. It is evident that for a 15° scanned beam the gain advantage of an elliptical reflector with aspect ratio 1.6 is useful but arguably marginal at 0.35dB. However, for a 20° scanned beam, the gain advantage is close to 1.0dB. With the relationship between aperture size and gain somewhat blurred because of the phase and amplitude imbalance of the scanned feed characteristics across the reflector, an increase of 20-25% to the reflector dimensions may be required to offset a 1dB gain deficit for a scanned feed at 20°. With the satellite system providers being extremely sensitive to the appeal and aesthetics of such antennas to members of the public, this potential increase in size can be detrimental to the viability of the whole network and consequently the opportunity to make use of a smaller size is a major advantage of the elliptical reflector.
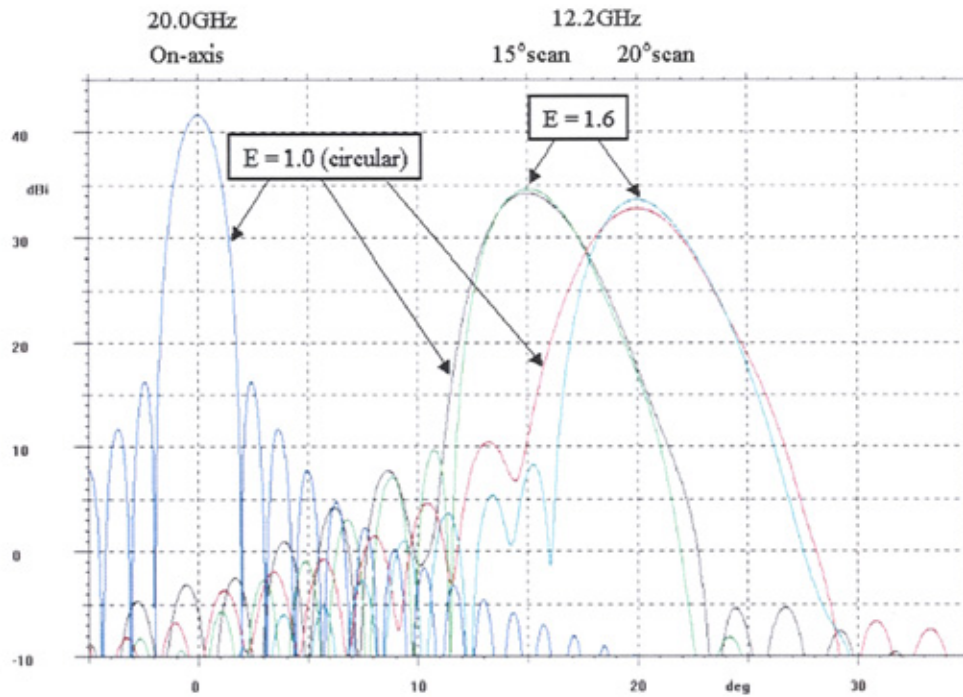
Figure 5.3 *Elliptical vs Circular aperture scanned-beam performance comparison.*
Aperture area constant for both values of E. (On-axis beam shown for reference)

Having established a strong case for the use of elliptical reflectors over the equivalent circular reflector, it is now necessary to examine the implications of this on the feed design itself, as discussed in the next section.

5.2 Elliptical reflectors and their impact on feed horn design

As outlined in Chapter 1, the aim of the feed horn designer is to properly match its radiation characteristics to a pre-defined reflector optical geometry in order to provide the optimum illumination characteristics, which in turn yield the desired secondary radiation characteristics from the antenna.

For the case of a circularly-symmetric antenna geometry this implies the need for a circularly-symmetric radiation pattern from the feed horn, which in turn implies the need for a circularly-symmetric, conical horn, as detailed in Chapters 2, 3 and 4.

By the same logic, the case of an elliptical antenna geometry implies the need for an elliptical radiation pattern to yield efficient illumination of the reflector (as inferred with the results obtained in Figure 5.1 where the feed illumination was manipulated to provide a nominal −10dB edge taper at the reflector rim for all values of E). As expected, this can be achieved with use of an elliptical (or rectangular) feed horn. However, now the quality of the horn design is not set by the E- to H-plane symmetry of the radiation pattern, as was the case for the circular, conical horn, but by the similarity, or balance achieved between the radiation pattern for Vertically polarised signals versus that for Horizontally polarised signals. Without this balance, the reflector is illuminated differently in each case and the antenna secondary patterns and gains differ depending on the polarisation employed.

Figure 5.4 shows in an exaggerated manner how this occurs, the effect being compounded with increase in E. The VLP primary pattern can be seen to match the reflector geometry, offering a more efficient illumination and therefore higher secondary gain. The HLP primary pattern on the other hand, is mis-matched to the reflector and yields a lower secondary gain. Significantly, the non circularly-symmetric primary radiation pattern is representative of a corrugated horn operating away from the balanced hybrid condition.

Accepting this may not be too detrimental to the overall system performance for linearly polarised (LP) systems, the use of circular polarisation (CP) presents a more subtle and complex set of difficulties.
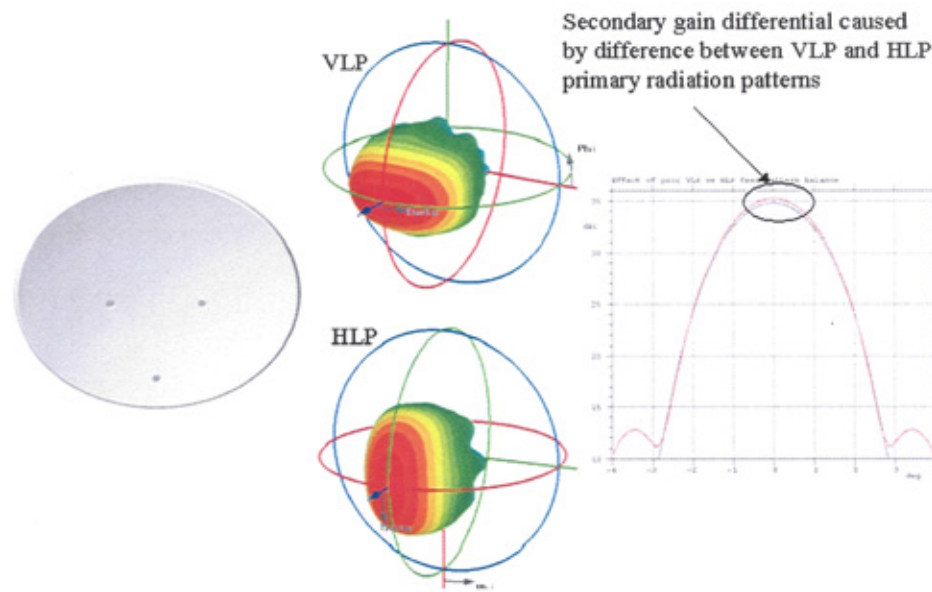
Figure 5.4 *Effect of dissimilar VLP vs HLP primary horn patterns on secondary gain differential*

5.3 Circular Polarisation in elliptical reflectors:

In order to properly determine the impact of CP in elliptical reflectors it is first necessary to discuss the fundamentals of CP and subsequently examine in detail the signal path throughout the antenna in the context of the phase and amplitude relationships required to satisfy the conditions for good CP.

The degree to which a signal is regarded as being circularly polarised is defined by the parameter 'axial ratio' where this is a measure of the ratio of major and minor axis of the ellipse plotted by the path of the rotating polarisation vector. Just as there are Vertical and Horizontal polarisations in the linear domain, so there are Right-Hand and Left-Hand polarisations in the circular domain. These are related through the definitions,

$$\text{RHCP} = |\,\text{VLP}\,|\,\angle\theta° + |\,\text{HLP}\,|\,\angle(\theta + \phi)° \tag{5.1}$$

$$\text{LHCP} = |\,\text{VLP}\,|\,\angle\theta° + |\,\text{HLP}\,|\,\angle(\theta - \phi)° \tag{5.2}$$

Axial ratio is subsequently given by,

$$AR = \sin(\phi)\sqrt{\frac{1+r^2+\sqrt{4r^2\cos(\phi)^2+\left(1-r^2\right)^2}}{1+r^2-\sqrt{4r^2\cos(\phi)^2+\left(1-r^2\right)^2}}} \tag{5.3}$$

where ϕ is the differential phase between VLP and HLP components and r is the ratio of the amplitude of VLP to HLP components.

CP signals are often generated in the waveguide portion of the feed chain by a device known as a polariser. This device converts LP signals to CP signals in Transmit mode or decomposes CP signals to LP signals in Receive mode. The quality of the polariser design is judged by its ability to deliver an axial ratio as close to 1 over the required bandwidth, which from Equation 5.3 requires |VLP| = |HLP| and $\phi = 90°$.

Considering the Transmit mode as the reciprocal, and therefore also representative, of the Receive mode, the signal path through the feed chain and antenna starts out as an LP signal. As it passes through the polariser it is converted to a CP signal having both VLP and HLP components with the desired amplitude and phase relationships to yield the required axial ratio.

These two linear components then propagate through the horn antenna and subsequently radiate out to illuminate the reflector from which they are collimated to propagate through space to the satellite. Throughout this chain, if the quality of the axial ratio provided by the polariser alone is not to be degraded, the phase and amplitude relationships between the VLP and HLP components must be maintained. This implies two important constraints, both of which having a significant impact on the design of the feed horn.

65

5.3.1 Design constraint Number 1:

The first constraint relates to the phase relationship between VLP and HLP such that, in order to maintain the $\phi = \pm 90°$ differential phase provided by the polariser, the phase velocity of each linear polarisation must be equal. By definition, for simultaneous RHCP and LHCP operation (frequency re-use), this implies the waveguide path in front of the polariser must be either circular or square in cross-section, which then imposes the restriction that the feed horn must also be circular or square.

The penalty for not choosing a square or circular cross-section is demonstrated in Figure 5.5, which, from Equation 5.3, plots axial ratio and, for subsequent ease of comparison, crosspolarisation against phase differential between the vertical and horizontal components. The x-axis represents the differential phase over and above that which would already be present in a practical polariser design providing 0.5dB axial ratio (-30.7dB crosspolarisation), and therefore represents the additional differential phase introduced as a consequence of any asymmetry in the waveguide path. The phase differential for a given asymmetrical horn would be dependent on its exact geometry and the frequency of operation and would need to be investigated on a case-by-case basis. Nevertheless Figure 5.5 shows that, for good axial ratio, asymmetrical geometries should be avoided.
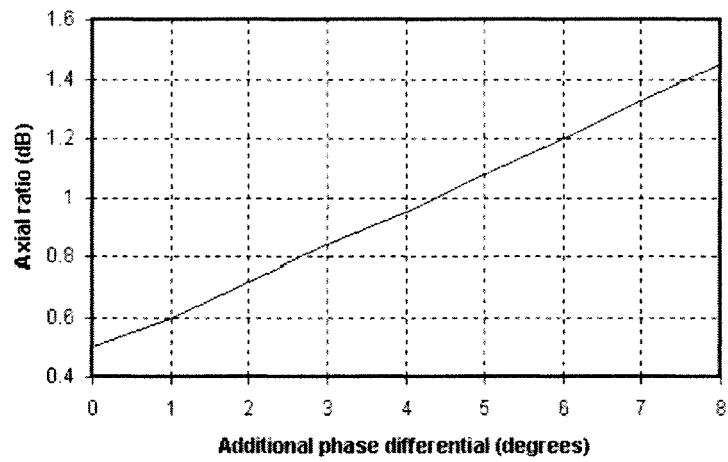
(a)
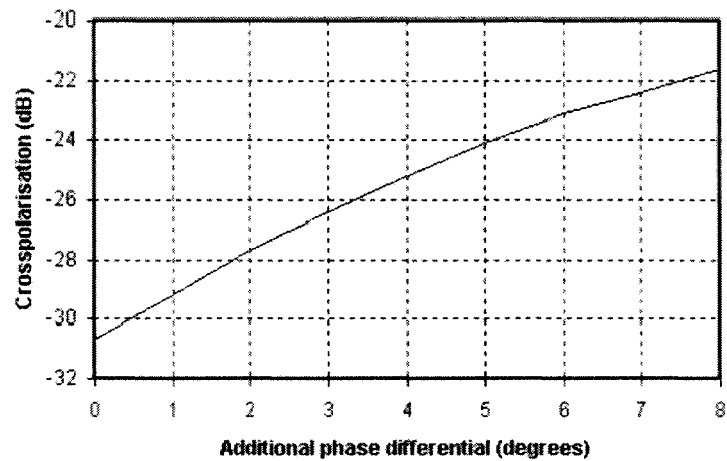
(b)

Figure 5.5 *Axial ratio (a) and Crosspolarisation (b) vs additional phase differential*

Imposing the constraint that the feed horn must be circular or square for use with an elliptical reflector is in conflict with the need to match the illumination characteristics to the reflector shape as highlighted at the start of section 5.2 and demonstrated in Figure 5.1. The question then arises as to what performance can be achieved with this as a restriction?

In an effort to answer this, it is useful to repeat the exercise carried out in Figure 5.1 with a fixed feed illumination for all values of E, to represent the use of a circular feed aperture. Figure 5.6 provides a comparison of the antenna radiation patterns in the plane of the major axis for offset reflectors having different values of E where the feed illumination is circularly-symmetric and fixed at −10dB at the rim of the reflector for the case E = 1.0 (circular).

Now the antenna efficiency and therefore gain degrade with increase in E; a result to be expected as the illumination becomes less and less matched to the reflector shape. However, as plotted in Figure 5.7, the degradation is generally acceptable with only a 2% drop in efficiency for E=1.4 and 4% for E = 1.6, equating to 0.11dB and 0.25dB gain drop respectively.

In comparison with Figure 5.2(a), under the constraint of a fixed feed illumination the −3dB beamwidth remains more constant with E, although does vary in accordance with Figure 5.8(a). In addition the levels of the sidelobe envelope in the plane of the major axis are improved beyond those of Figure 5.2(b) as evident in Figure 5.8(b).
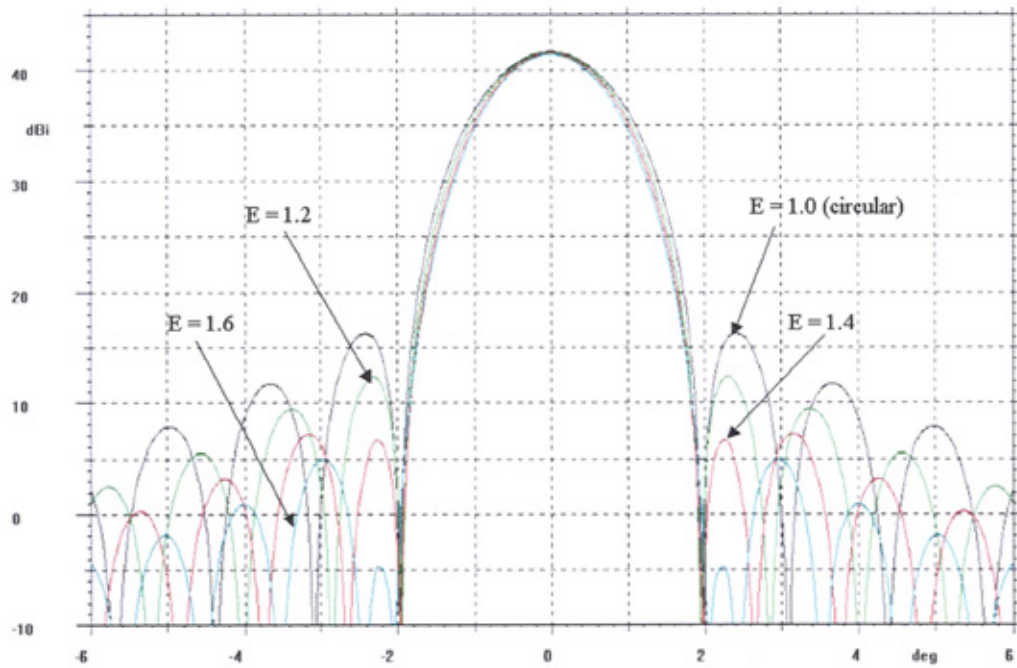
Figure 5.6 ±6° antenna radiation patterns in the plane of the major axis of the
ellipse with E, the elliptical aspect ratio, as a parameter. Feed illumination fixed for
all case at −10dB @ 37.5°.
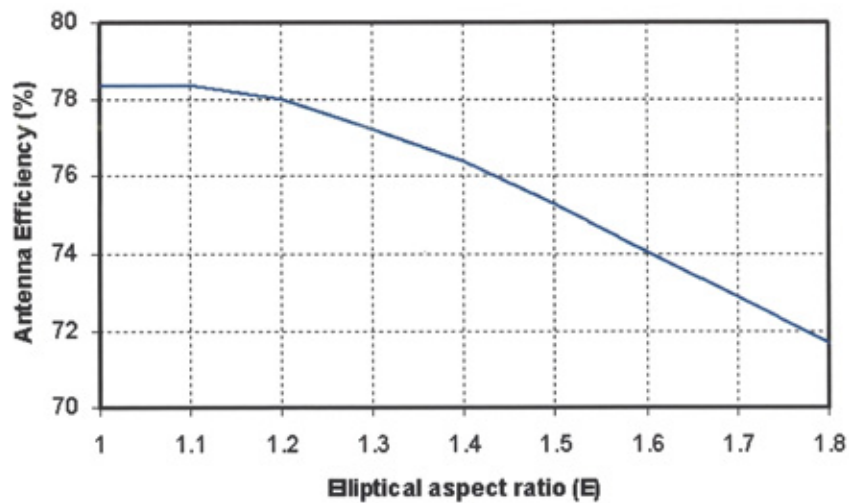
Figure 5.7 Variation in antenna efficiency vs elliptical aspect ratio E. Feed
illumination fixed for all case at −10dB @ 37.5°.
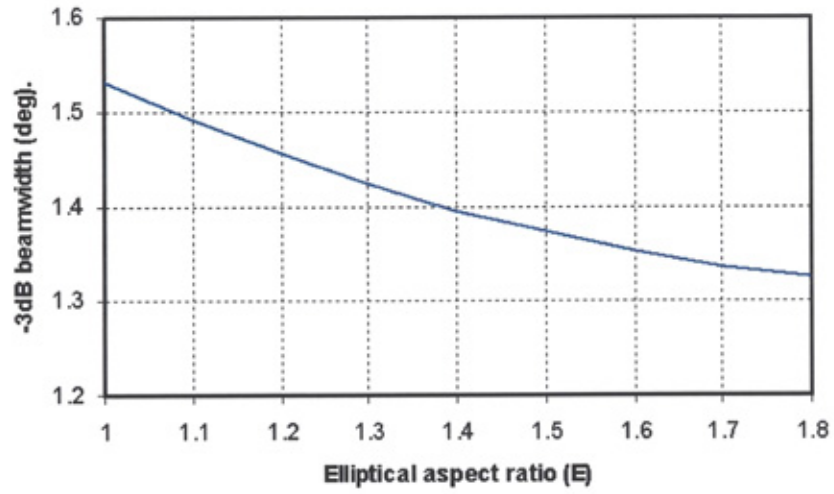
(a)
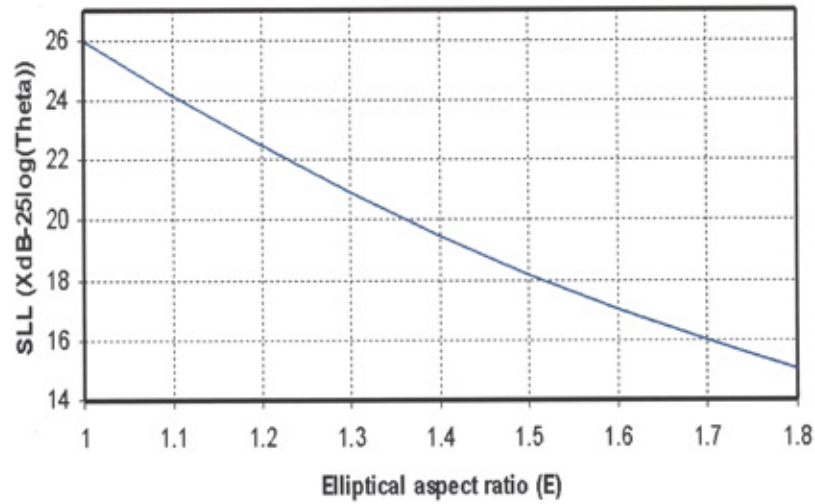
(b)

Figure 5.8 –3dB beamwidth (a) and sidelobe level (b) vs elliptical aspect ratio, E.
Feed illumination fixed at –10dB @ 37.5° for all values of E.

The Y-axis scale represents the value of XdB in the equaition $X - 25\log(\theta)$, where θ is the angle from boresight – a formula commonly used to quantify the sidelobe envelope in antennas for satellite communications

Design constraint Number 1 therefore calls for a horn with circular symmetry. Whether the resulting circular illumination characteristics are acceptable is largely dependant on the specific application for which the antenna is being designed. The results provided here however, indicate that for elliptical reflectors with values of E < 1.6, the small penalty in antenna efficiency is more than offset by the significant improvement to axial ratio this approach allows the designer to realise; provided of course design constraint Number 2 is also adhered to.

5.3.2 Design constraint Number 2:

The second design constraint relates to the amplitude relationship between VLP and HLP. Before continuing and to avoid confusion it is beneficial to highlight certain definitions used in the subsequent discussions.

Primary – relates to the feed horn itself

Secondary - relates to the overall antenna and includes the effect of both the feed horn and the reflector

LP crosspolarisation - relates to the crosspolarisation between VLP and HLP components

CP crosspolarisation - relates to the crosspolarisation between RHCP and LHCP components

Axial ratio (AR) – defined by Equation 5.3. Relates to CP crosspolarisation through Equation 5.4

(The terms 'CP crosspolarisation' and 'axial ratio' are used as equivalents throughout the text depending on the context).

$$CPxpol = 20\log\left(\left(10^{AR/20} - 1\right)/\left(10^{AR/20} + 1\right)\right) \qquad (5.4)$$

Following Figure 5.4, to ensure the secondary antenna gain is equal for each linear polarisation component, the illumination characteristics of the horn for both Vertical and Horizontal polarised components must be the same. Adhering to design constraint Number 1 it is assumed the feed horn is circularly symmetric; consequently to achieve secondary gains that are equal for each linear polarisation implies that the primary copolar patterns are also circularly symmetric.

Figure 5.9 shows, in a more quantitative manner, the effect illustrated in Figure 5.4. It attempts to evaluate the effect of illuminating elliptical reflectors with a non-circularly symmetric primary radiation pattern with a plot of differential gain between the reflector illuminated with the primary pattern arising from a horizontally polarised signal versus that arising from a vertically polarised signal for a horn having an asymmetrical primary pattern. The feed illumination is represented by means of a simple exponential function, chosen to approximate well the radiation pattern of a corrugated horn operating at the extremes of the band (either at 19 or 30GHz) when the copolar pattern symmetry is beginning to degrade.

Using peak LP crosspolarisation in the $\phi = 45°$ plane as the metric by which to quantify primary pattern *asymmetry*, the reflector in Figure 5.9 is illuminated with a feed having a peak LP crosspolar level of –25dB, which although worse than suggested by the findings of Chapter 3 and 4, is a possibility in practical conventional feed designs, as discussed in Chapter 8.
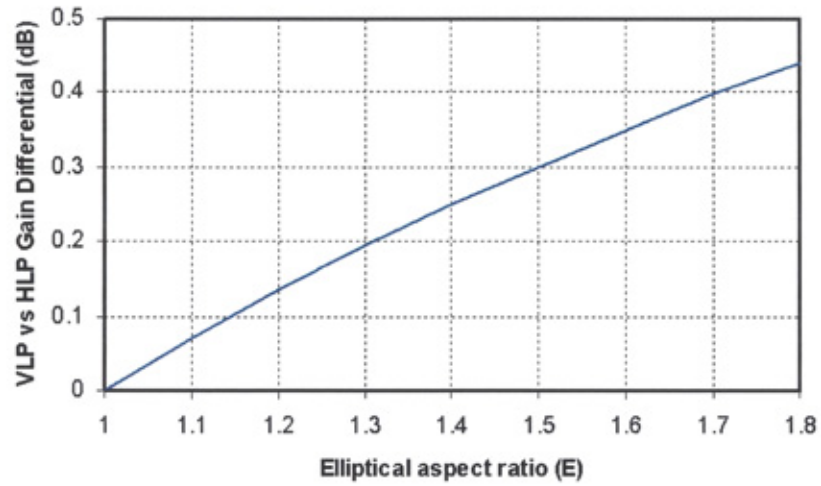
Figure 5.9 *Secondary gain differential as a consequence of primary pattern asymmetry vs reflector aspect ratio (E). Reflector illuminated with asymmetric primary feed pattern having –25dB peak crosspolarisation.*

Considering the same VLP and HLP feed illumination characteristics used in Figure 5.9 and applying these as the two components of an equivalent CP illumination of the reflector, it is possible to illustrate directly the consequences of the asymmetry of the primary radiation patterns on the secondary CP crosspolarisation.

For the purpose of providing a point of reference, it is useful to conduct this analysis with the assumption there is no additional contribution to CP crosspolarisation from other sources, thereby implying the polariser offers a perfect axial ratio of 0dB. However, to provide a realistic backdrop for practical antenna designs it is also useful to examine the condition whereby the effect of a polariser offering an axial ratio of 0.5dB (typical of the state-of-the-art) is superimposed on top of the effect of the asymmetry to primary radiation patterns. In this way it is possible to discriminate between particular phenomena and identify specific causes.

Figure 5.10 illustrates the predicted secondary CP crosspolar radiation patterns for four reflectors having different values of E in the range 1.0 to 1.6. For each reflector the CP crosspolarisation is plotted as a consequence of i) primary pattern asymmetry only, ii) 0.5dB axial ratio contribution from the polariser only and iii) combined effect of i) and ii). In each case the secondary copolar pattern is provided for reference.

Notice how there is no specific contribution to the secondary on-axis CP crosspolarisation from primary pattern asymmetry in the case of the circular reflector (E = 1.0) and that this phenomena is peculiar to elliptical reflectors.

Also note the small amount of copolar main beam squint, a consequence of illuminating an offset reflector with a CP feed [5.2].
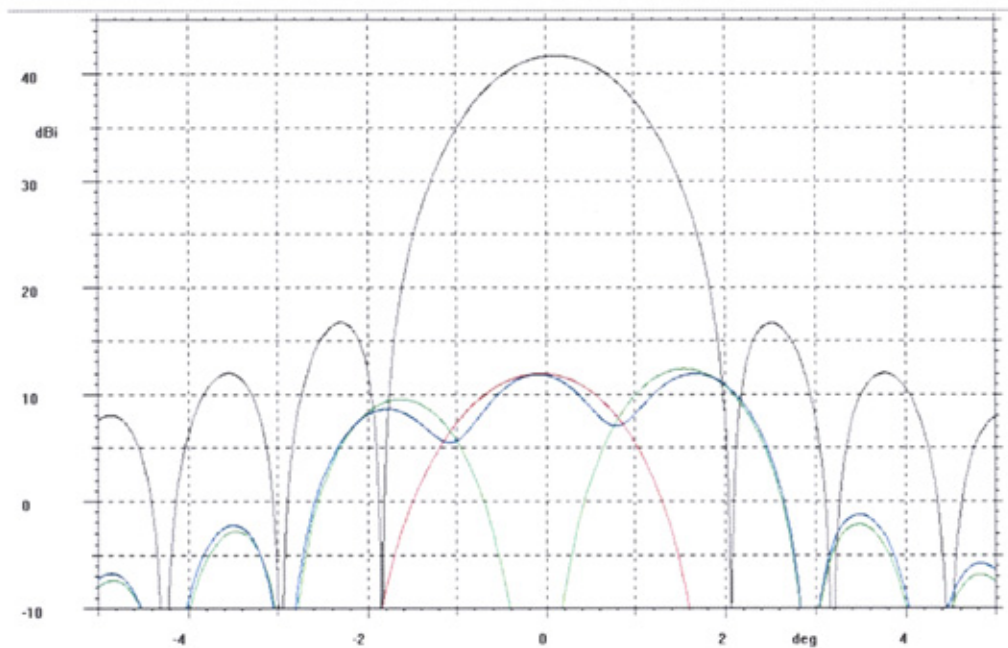
(a) E= 1.0 (circular)
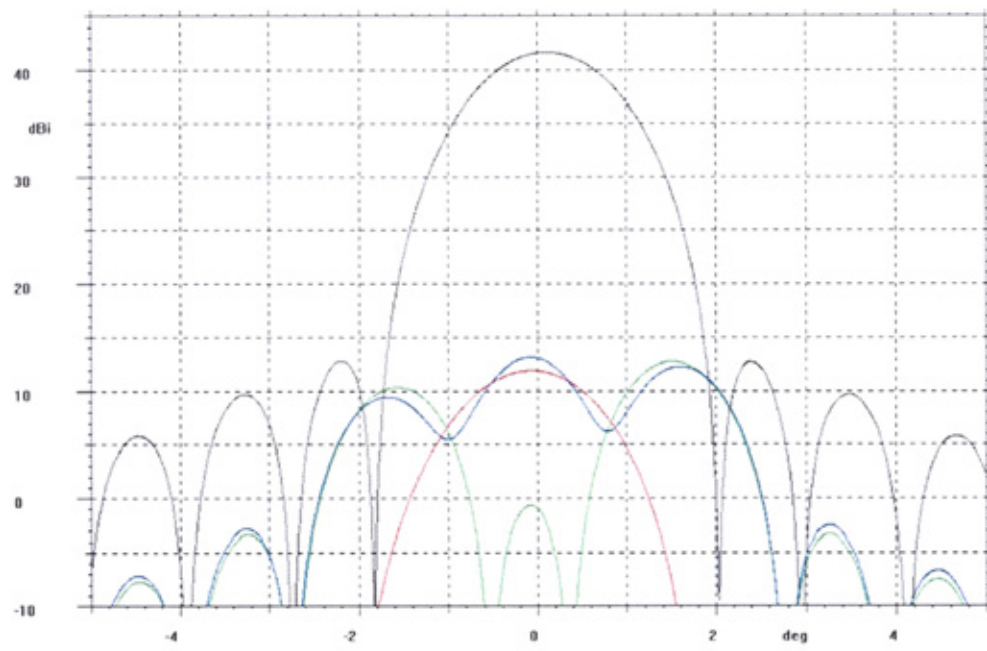
(b) E = 1.2
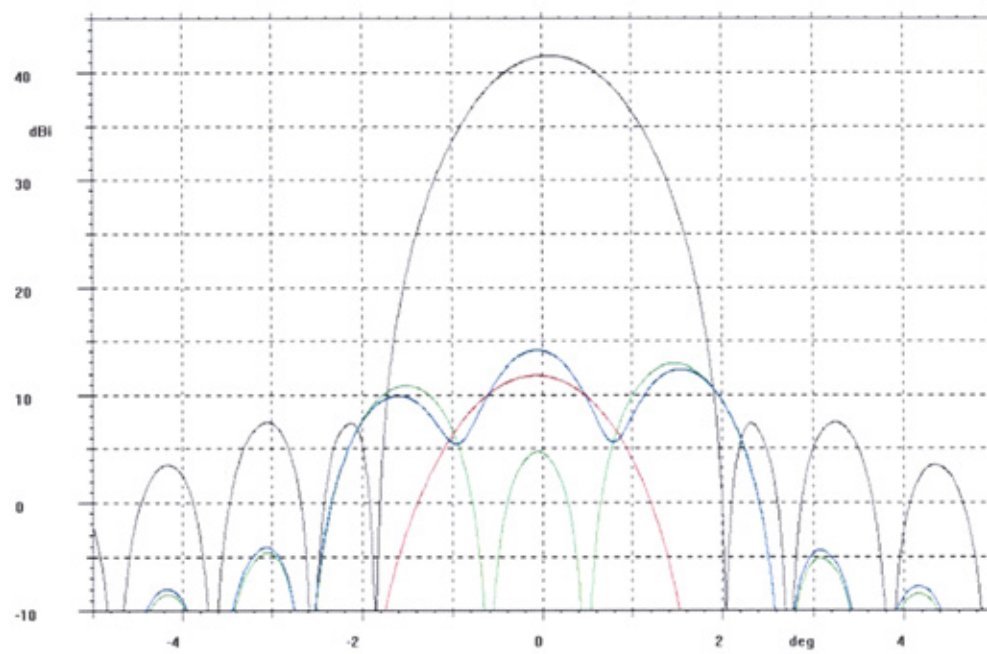
(c) E = 1.4
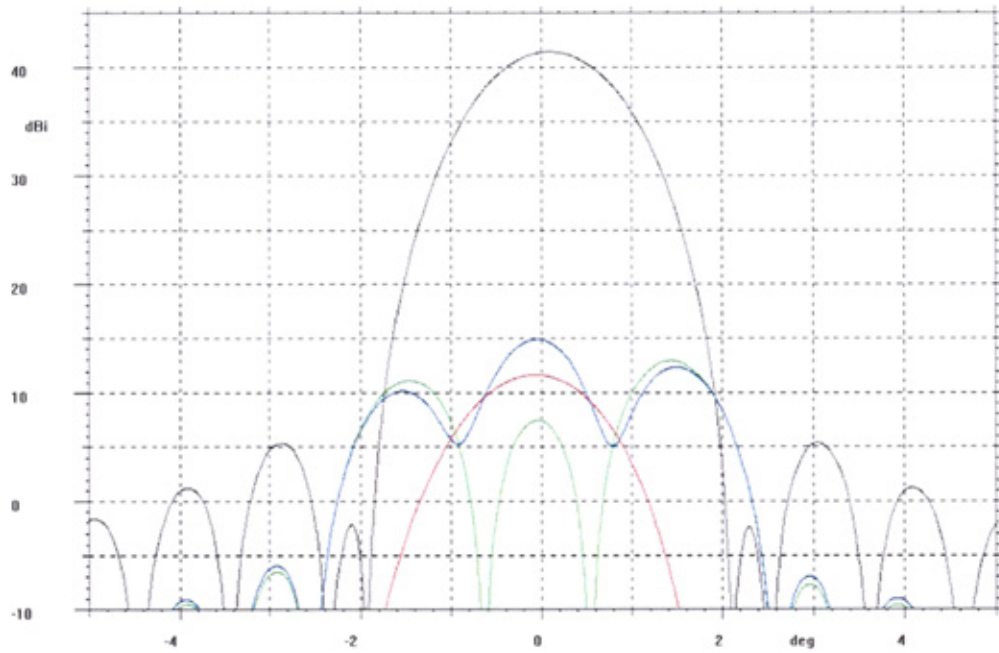
(d) E = 1.6

Figure 5.10 *Secondary CP crosspolarisation as a consequence of i) primary pattern
asymmetry only (equivalent to primary LP crosspolarisation of –25dB) – green
trace, ii) 0.5dB axial ratio contribution from the polariser only – red trace, and iii)
combined effect of i) and ii) – blue trace. For values of E from 1.0 to 1.6.*

Using the results of Figure 5.10 to plot the level of secondary on-axis CP
crosspolarisation as a consequence of primary pattern asymmetry alone (green trace),
as in Figure 5.11, provides an interesting comparison with the results in Figure 5.9.
The red dots on Figure 5.11 are points taken directly from Figure 5.9 after having
been translated to CP crosspolarisation, first through Equation 5.3 and then through
Equation 5.4.

Here then is proof that gain differential caused by primary pattern asymmetry
contributes directly to secondary on-axis CP crosspolarisation in elliptical reflectors.
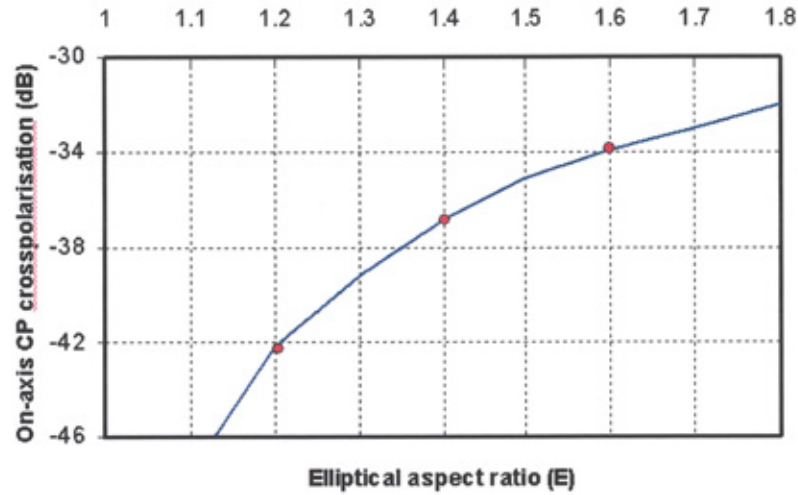
Figure 5.11 *Contribution to secondary on-axis CP crosspolarisation as a consequence of VLP vs HLP primary pattern imbalance equivalent to –25dB peak crosspolarisation.*

Of practical note is the overall degradation to secondary on-axis CP crosspolarisation for the case when the contribution from the polariser is included. Considering the case for which E = 1.6, the CP crosspolarisation degrades by > 3dB (axial ratio by > 0.25dB) for a primary pattern asymmetry equivalent to -25dB peak LP crosspolarisation.

Again using the crosspolarisation in the $\phi = 45°$ plane as a metric for primary pattern asymmetry, Figure 5.12 illustrates the degradation to secondary on-axis CP crosspolarisation of three horns offering –25dB, -30dB and –35dB LP crosspolarisation. It is clear that, for this antenna geometry, even a horn with –35dB peak LP crosspolarisation yields a >1dB degradation to overall antenna crosspolarisation.

Design constraint Number 2 therefore calls for a horn having better than –35dB LP crosspolarisation and consequently superior pattern symmetry.

77
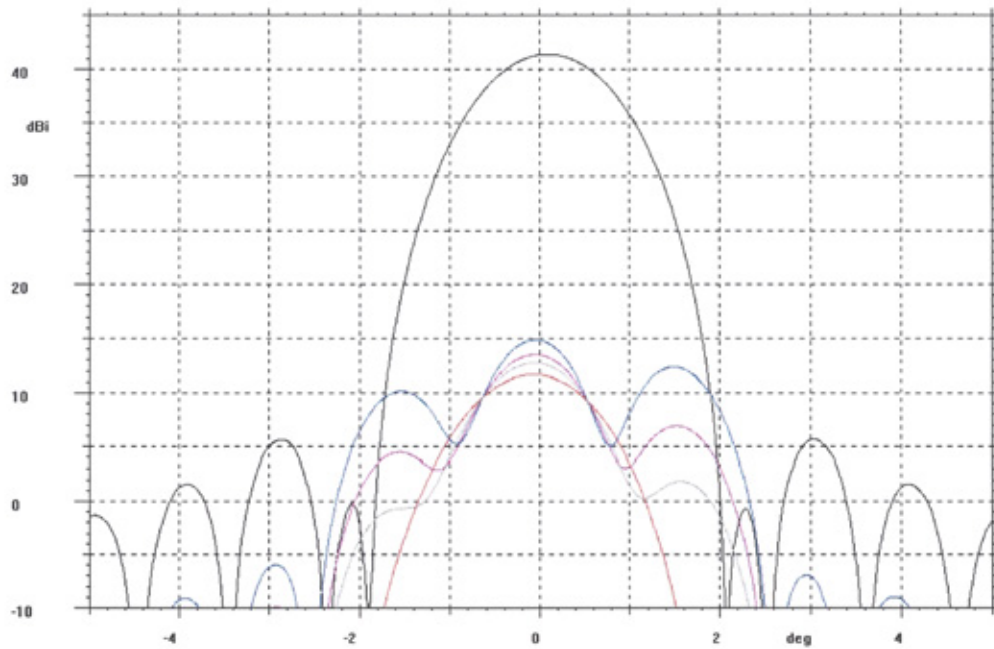
Figure 5.12 *Secondary CP crosspolarisation as a consequence of primary pattern asymmetry; blue = -25dB, magenta = -30dB, grey = -35dB, red = zero; for an elliptical reflector with E = 1.6. Includes 0.5dB axial ratio contribution from the polariser.*

The characteristics required from the primary radiation patterns and ultimately therefore the performance of the horn used to illuminate the reflector is dictated by the overall antenna specification, the axial ratio offered by the polariser and the elliptical aspect ratio, E, of the reflector. With the demand for ever-increasing system capacity placing additional emphasis on the performance of frequency re-use system architectures, and therefore a greater emphasis on the crosspolar performance of the antenna, there is a need for a horn with better characteristics than those of the conventional designs described in Chapters 3 and 4.

The design constraints presented here suggest the horn should be circularly symmetric with superior polarisation purity and related to this, superior copolar pattern symmetry than the state-of-the-art. Chapter 6 presents a novel idea for a horn to address this need.

5.4 References

[5.1] Clarricoats, P.J.B. and Saha, P.K.: *Propagation and radiation behaviour of corrugated feeds, pt I corrugated waveguide feeds*, Proc. IEE, 1971, Vol. 118, pp 1167-76.

[5.2] Rudge, A.W. and Adatia, N.A.: *Offset parabolic-reflector antennas: a review*, Proc. IEEE, 1978, Vol. 66, No.12, pp 1592-1618.

Chapter 6

HE$_{11}$ Dual-Band Horn

Having identified a potential shortfall in the performance of the conventional horn designs described in Chapters 3 and 4, the following section introduces a novel, hybrid horn that attempts to address the critical issue identified in Chapter 5 relating to the illumination of elliptical reflector antennas for satellite communications. In such applications, rather than a need for good performance over a continuous wide band, the requirement is more for good radiation characteristics in two separate sub-bands corresponding to the Receive and Transmit functions at the lower and upper limits of a wider overall bandwidth.

Consequently, the emphasis on performance is focused on the extremes of the overall band, in this case 18.3-20.2GHz and 29.5-30.0GHz, and there is little concern for what happens to the radiation characteristics in the range 20.20-29.5GHz.

This affords the opportunity to make use of two exclusive mechanisms to independently optimise the performance at each sub-band. The horn described herein makes use of a corrugated structure, but, unlike conventional designs, employs a secondary mechanism that takes effect once the performance as a consequence of the corrugations themselves begins to degrade [6.1, 6.2].

6.1 Background

In Chapter 2 the desirable properties of the HE_{11} mode were broken down into the appropriate combination of TE_{11} and TM_{11} smooth-walled waveguide modes. Horns employing this 'dual-mode' concept, as developed by Potter [6.3] and Satoh [6.4], provide boundary conditions such that the modes only combine favourably over a limited bandwidth.

The conventional corrugated horn operating in the HE_{11} mode, as discussed in Chapter 3, represents a significant improvement over the dual-mode horns due to its potential for good crosspolar performance over a much wider bandwidth. For antennas employed for satellite communications such operational bandwidths are usually sufficient to ensure adequate crosspolar performance in two separate sub-bands coinciding with the receive and transmit bands. However, when the frequency bands are separated by a ratio of 1.5:1 or more, the conventional corrugated horn can struggle to meet stringent crosspolar demands at the fringes of the overall band where polarisation purity of the HE_{11} mode begins to deteriorate due to the change in the electrical depth of the corrugations. Following Chapter 5, this leads to a degradation to on-axis axial ratio when used as a horn to illuminate elliptical reflector antennas.

However, by taking advantage of two different mechanisms, the operation in each sub-band can be optimised separately to improve overall crosspolar performance.

6.2 Principles of operation

Drawing on the analysis of Chapters 2 and 3 for the corrugated horn, as the frequency of operation increases well beyond that at which the balanced hybrid condition occurs, the corrugation depth increases from $\lambda/4$ and tends towards $\lambda/2$. From Equation 3.13, the surface impedance at $r = r_1$ under this condition is approximated as

$$\overline{Y}_m\left(k_0 r_1\right) \rightarrow \infty \tag{6.1}$$

which, from Equation 3.8, with the condition $\overline{k}_z \rightarrow 1$ well satisfied, implies that

$$F_1\left(k_{\rho_1} r_1\right) \approx 0 \tag{6.2}$$

and from Equation 3.9 implies that

$$\overline{\Lambda} \rightarrow \infty \tag{6.3}$$

Referring back to the general modal analysis of Chapter 2, Equation 2.9 indicates that Equation 6.3 is only satisfied if $a_m = 0$. The longitudinal electric field components defined in Equation 2.7 are subsequently excluded and only longitudinal magnetic field components are present in the central region of the waveguide. The presence of only magnetic longitudinal field components implies the transverse field distribution to be that of a TE mode. Equation 6.2 also suggests that Equation 2.13 reduces to

$$J_m'\left(k_{\rho_1} r\right) = 0$$

This is satisfied when $k_{\rho_1} r = 1.841$, the solution for the TE_{11} mode in smooth-walled circular waveguide of radius r_1.

The important conclusion from this is that as the frequency of operation increases, well beyond that at which $\overline{\Lambda} = 1$, the slot depth approaches $\lambda/2$ and the corrugated horn begins to exhibit similar characteristics to those of a smooth-walled horn of radius r_1. Crosspolarisation and pattern symmetry are correspondingly poor as demonstrated in Figure 2.2a.

With the corrugated horn operating in this state and following the concept of the dual-mode horn discussed in Chapter 2, it is reasonable to postulate that the addition of a suitable amount of TM_{11} mode to the existing fields in the corrugated horn may be enough to re-establish good pattern symmetry and low crosspolar levels, as in Figure 2.2b.

Applying this idea to the modal analysis of Chapter 3, it is possible to determine the validity of the hypothesis by means of examination of the aperture field distribution in relation to the copolar and crosspolar radiation patterns. Additional numerical analysis later in this chapter and in Chapter 7 explores the bandwidth limitations associated with this approach.

6.3 Modal analysis

Following the radiation pattern results of Figure 3.7 (reproduced here for convenience), the corresponding aperture field distribution at the upper frequency $f/f_0 - 1 = +0.24$ (30.0GHz) is provided in Figure 6.1.
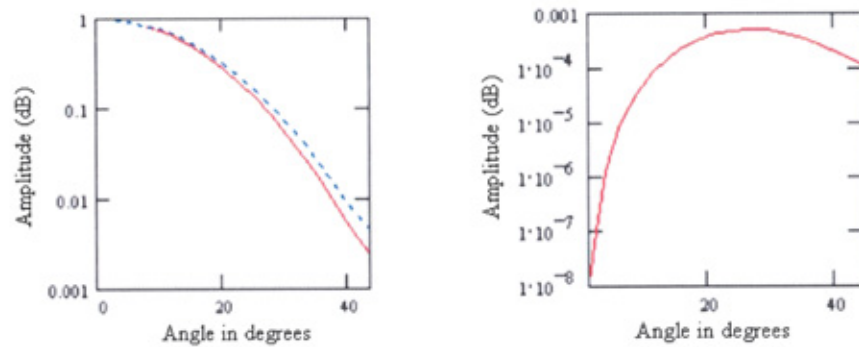
(a)
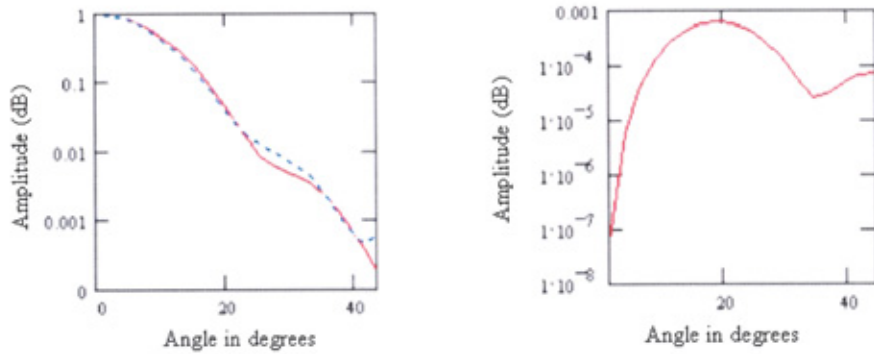
(b)

Figure 3.7 (reproduced). *Co- and crosspolar patterns at a) f/f₀-1 = -0.24 (19GHz)*
and b) f/f₀-1 = +0.24 (30GHz). HE₁₁ mode only. Slot depth chosen to yield $\overline{Y} = 0$ at
f/f₀ − 1 = -0.15 (see Figure 3.6)
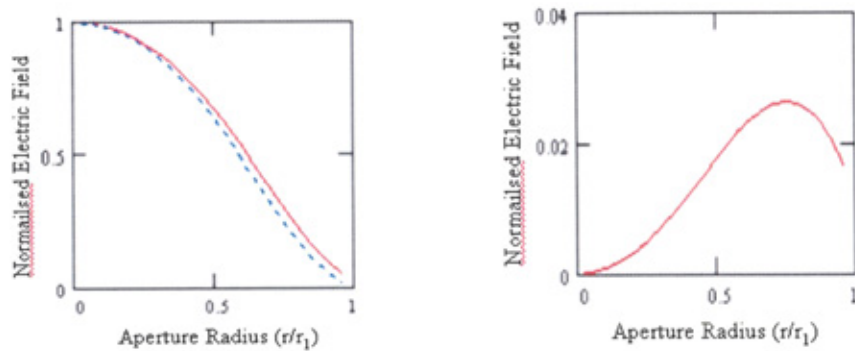
Figure 6.1 *Co- and crosspolar aperture field distribution at f/f₀-1 = +0.24. Slot*
depth chosen to yield $\overline{Y} = 0$ at f/f₀ − 1 = -0.15

By combining the modal content as a consequence of the HE_{11} mode with an appropriate amount of TM_{11} mode, the aperture distribution can be modified to improve performance, in a similar manner to the Potter horn discussed in Chapter 2, Figure 2.2.

For comparison against Figure 6.1, Figure 6.2 illustrates the change to the aperture distribution together with the resulting radiation patterns following a change to the modal content such that 7% is converted to the TM_{11} mode. Note how the level of radiated crosspolarisation has improved from –32dB to –43dB at the upper frequency limit (30GHz).
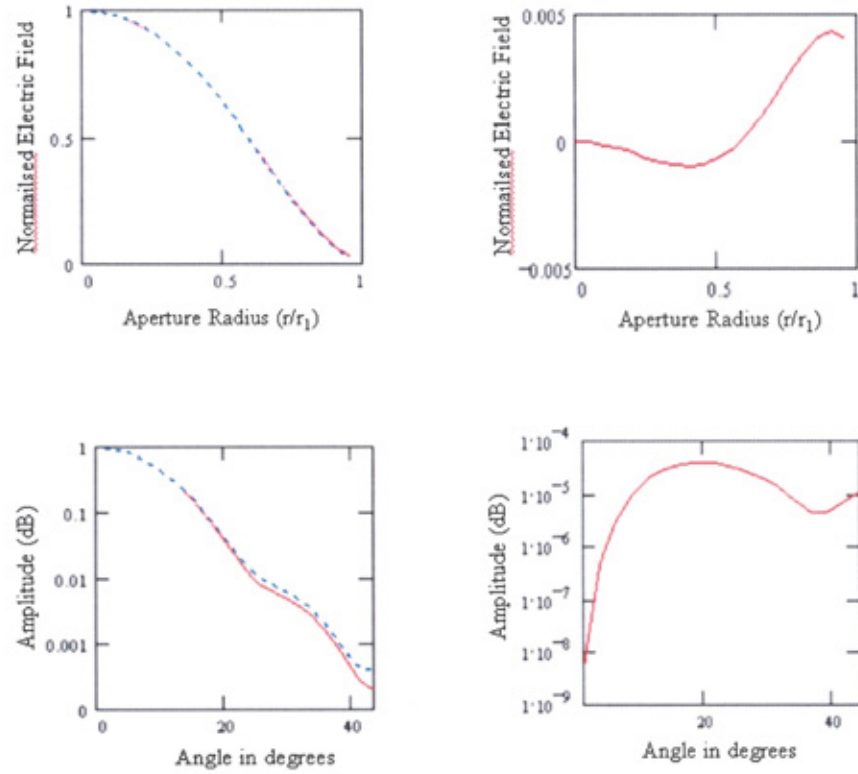
Figure 6.2 *Co- and crosspolar aperture and radiated fields at f/f_0-1 = +0.24 (30GHz) – 93% HE_{11} mode + 7% TM_{11} mode. Slot depth chosen to yield $\overline{Y}$ = 0 at f/f_0 – 1 = -0.15*

With the geometry of the horn throat forcing the TM_{11} to be cut-off at the lower sub-band the performance is unchanged there, still offering crosspolarisation levels of only –32dB as in Figure 3.7a.

However, extending this idea such that the corrugation slot depth is chosen purely to optimise the performance at the lower sub-band with the expectation that the performance at the upper sub-band can be enhanced by the addition of the appropriate amount of TM_{11} mode, there is scope to control each band independently, thereby ensuring better performance at both sub-bands.

To demonstrate this, Figure 6.3 shows the radiation patterns at $f/f_0-1 = -0.24$ (18.3GHz) with the slot depth increased (approximately 22%) to yield improved crosspolarisation of -40dB. This is only to be expected after re-plotting the variation in crosspolarisation versus frequency for this new slot depth, as in Figure 6.4 (to be compared with Figure 3.6 for the shallower slot depth). The same graph suggests the performance as a consequence of the HE_{11} mode alone at $f/f_0-1 = +0.24$ (30.0GHz) to be poor and this is confirmed in Figure 6.5 where the resulting aperture fields offer radiated crosspolarisation of only −23dB.
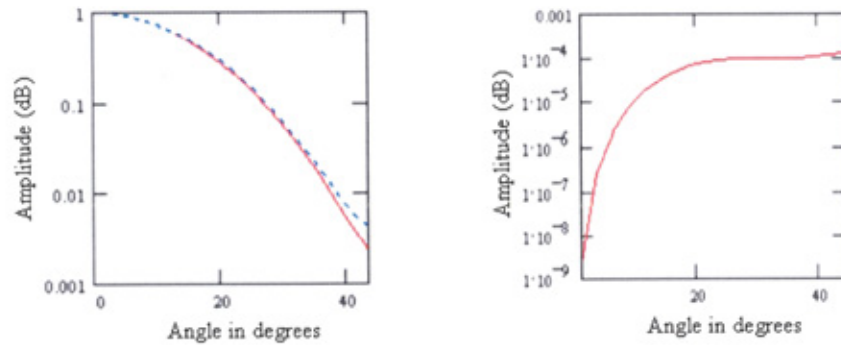
Figure 6.3 *Co- and crosspolar radiation patterns at $f/f_0-1 = -0.24$ (19GHz). Slot depth increased such that $\overline{Y} = 0$ at $f/f_0 - 1 = -0.29$*
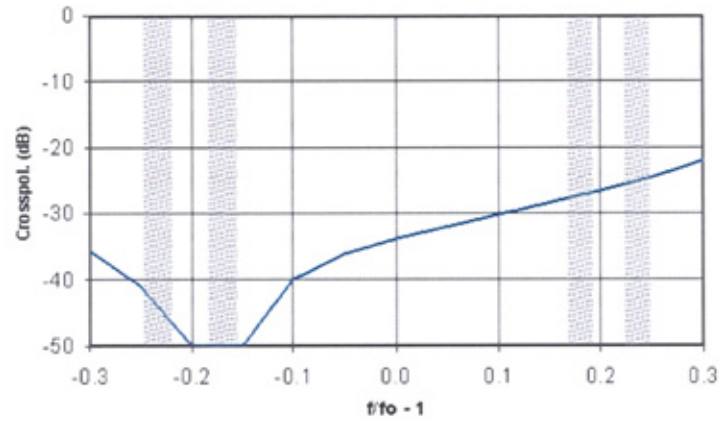
Figure 6.4 *Peak crosspol vs normalized frequency.*

Slot depth chosen to yield $\overline{Y} = 0$ *at* $f/f_0 - 1 = -0.29$ *and* $k_0 r_1 = 7$
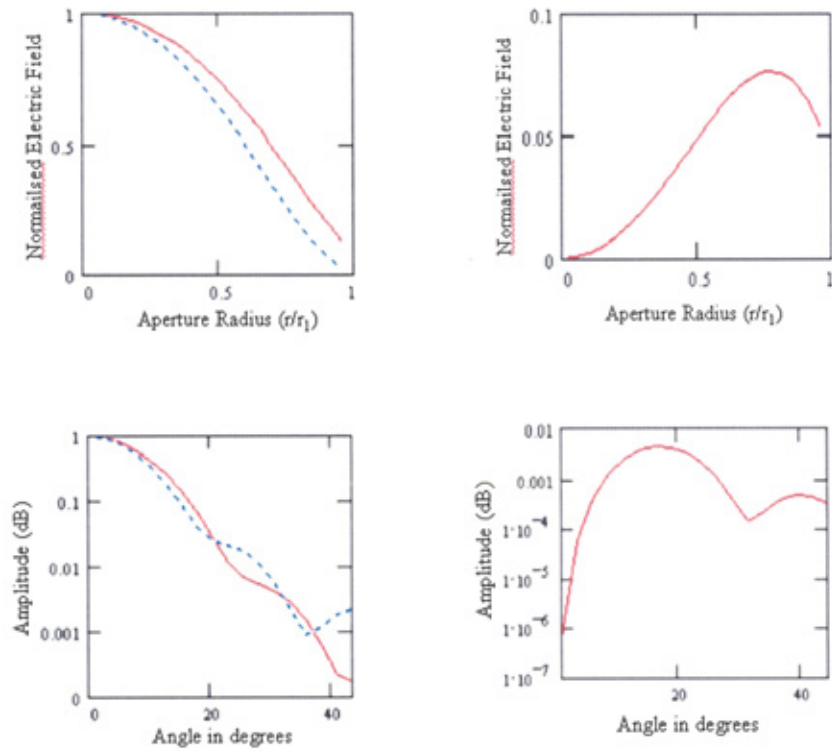
Figure 6.5 *Co- and crosspolar aperture and radiated fields at* $f/f_0 - 1 = +0.24$

(30GHz) – HE$_{11}$ mode only. Slot depth chosen to yield $\overline{Y} = 0$ *at* $f/f_0 - 1 = -0.29$.

However, by modifying the modal content at f/f_0-1 = +0.24 (30.0GHz) such that 18% is converted to the TM_{11} mode, as in Figure 6.6, the crosspolarisation improves dramatically to better than –43dB.

Note also how the shape of the copolar radiation pattern in Figure 6.6 is very similar to that of Figure 3.7 for the conventional corrugated horn operating at f/f_0-1 = +0.24 (30.0GHz) suggesting that the efficiency of the HE_{11} dual-band horn as a feed for reflector antennas to be similar to that of the conventional corrugated horn. With the conventional horn having been shown to demonstrate very favourable copolar characteristics by many authors, this is a desirable condition.
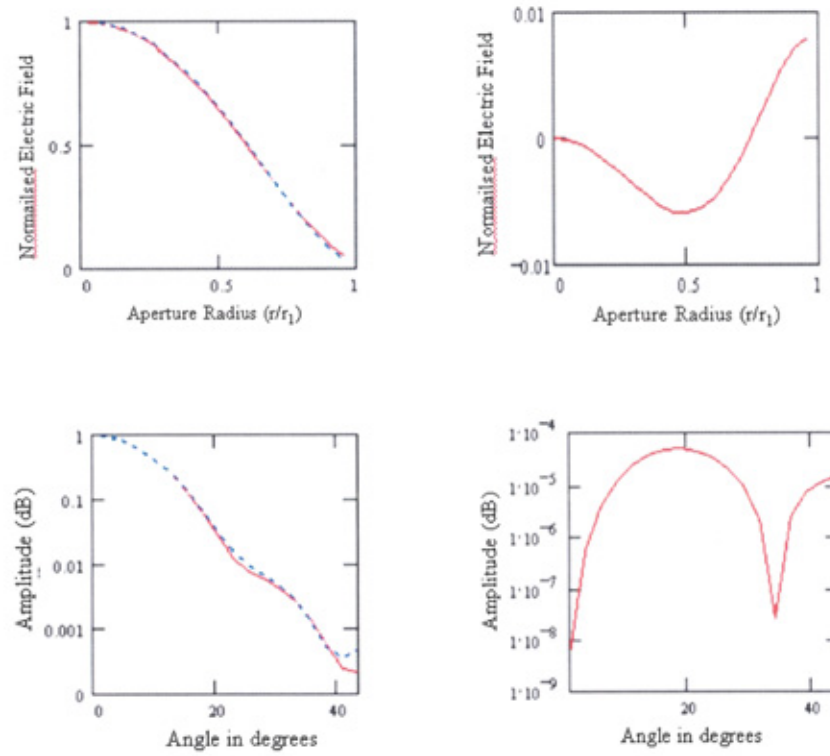
Figure 6.6 *Co- and crosspolar aperture and radiated fields at f/f_0-1 = +0.24 (30GHz) – 82% HE_{11} mode + 18% TM_{11} mode. Slot depth chosen to yield $\overline{Y} = 0$ at $f/f_0 - 1 = -0.29$.*

88

Whilst these are very encouraging results, it has been identified in Chapters 3 and 4 that the potential limiting factor in the operational bandwidth of conventional hybrid mode horns is not necessarily set by the frequency variation of the HE_{11} mode, but more the degradation due to the presence of higher order modes as the frequency increases. Therefore, in an effort to gauge the impact of this, Figure 6.7 shows the aperture field distribution and radiation patterns for the same horn as implied in Figures 3.7 and 6.1 but where the modal content is made up of 85% HE_{11} + 10% EH_{12} + 5% HE_{12}. (For this example the modes are assumed to combine in-phase). The presence of both higher order modes is consistent with Figure 3.2 where they are found to have similar cut-off frequencies and could therefore both be present in a practical horn. This is supported by [6.5] where the excitation and propagation of these two modes are investigated by way of scattering analysis.

The presence of these modes degrades the radiation patterns such that crosspolarisation changes from −32dB to −27dB. However, the performance can again be restored with the addition of an appropriate amount of TM_{11} mode, as in Figure 6.8, where crosspolarisation is improved to better than −40dB.
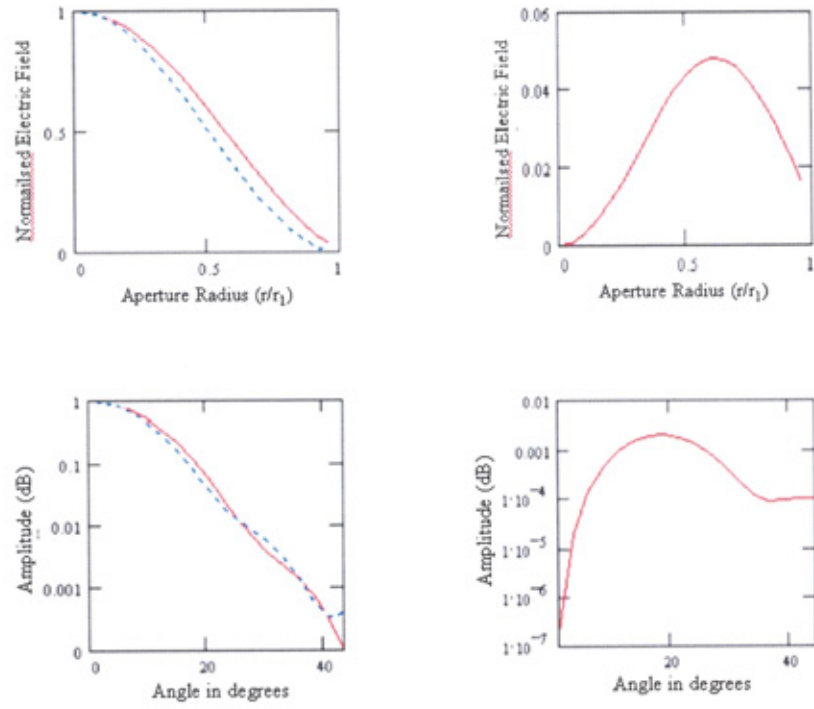
Figure 6.7 *Co- and crosspolar aperture and radiated fields at f/f₀-1 = +0.24* $(30GHz) - 85\% \, HE_{11} \, mode + 10\% \, EH_{12} \, mode + 5\% \, HE_{12} \, mode \, (in\text{-}phase). \, Slot$ *depth chosen to yield* $\overline{Y} = 0$ *at* $f/f_0 - 1 = -0.15$
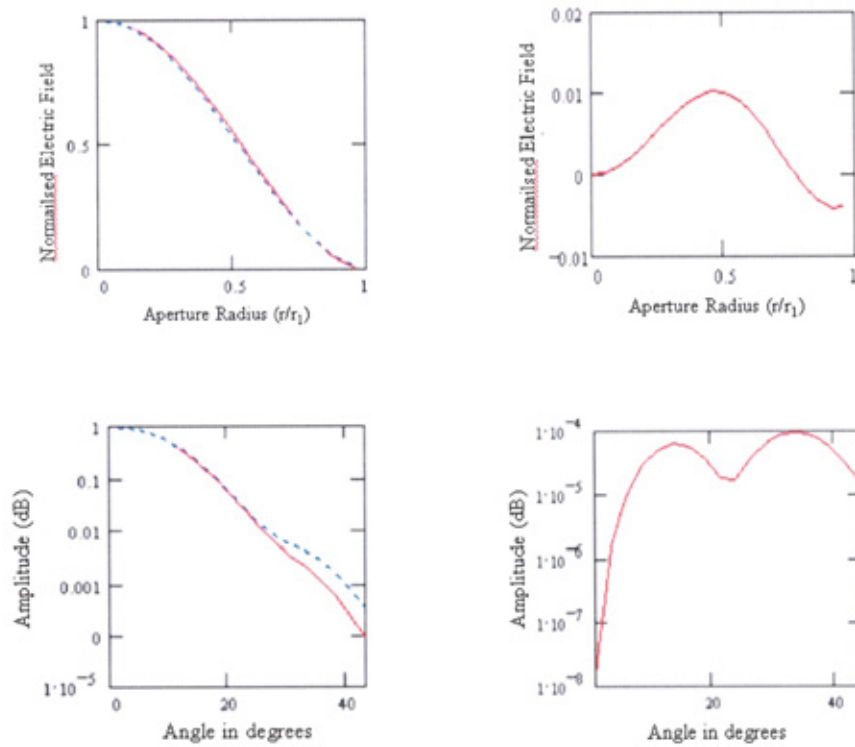
Figure 6.8 *As Figure 6.7, mode content modified to include 15% TM11 mode*

Although the above example assumes the higher order modes combine in-phase with the HE_{11} mode, a condition not typical in a practical horn design, the results here demonstrate the significant potential of the TM_{11} to control the aperture fields and consequently the radiation patterns, not only to compensate for changes to the characteristics of the HE_{11} mode but also to counteract the effect of higher order modes as the frequency of operation increases.

Despite these very encouraging results, the dependence on the interaction of two separate modes for good performance in the upper sub-band has inherent limitations with regard to the bandwidth over which the modes can be made to combine favourably. In contrast the useful bandwidth of the lower sub-band is set by the bandwidth over which an equivalent conventional corrugated horn can be made to operate with effective performance – this already having been demonstrated to be adequate for most applications.

With a view to examining the bandwidth issues for the upper sub-band the remainder of the chapter scrutinises the generation and interaction of the TM_{11} mode in more detail.

6.4 TM_{11} mode levels

As a good starting point it would be useful to determine the level of TM_{11} mode required to optimise crosspolarisation for a given horn geometry at a given frequency. This could then be used as one of the design criteria for the mode transducer within the horn.

In considering the parameter against which the TM_{11} modal content is best examined, there are several candidates from which to choose including the hybrid factor, Λ, and the normalized corrugation slot depth. However, in an effort to provide results independent of specific horn geometry and operating frequency, and after considering what ultimately dictates the required level of TM_{11} mode, the most useful parameter is that of peak crosspolarisation; specifically the level of crosspolarisation to be compensated for. This is also the parameter most easily determined by the designer through either analysis or measurement.

With this in mind, Figure 6.9 provides a plot of crosspolarisation vs TM_{11} mode for peak crosspolar values typical of a practical horn. The values have been determined iteratively using the modal analysis developed herein, the net result in all cases yielding crosspolarisation better than –42dB. Used in conjunction with Figure 6.4, the information in Figure 6.9 can be used as the initial design criteria for the mode transducer.
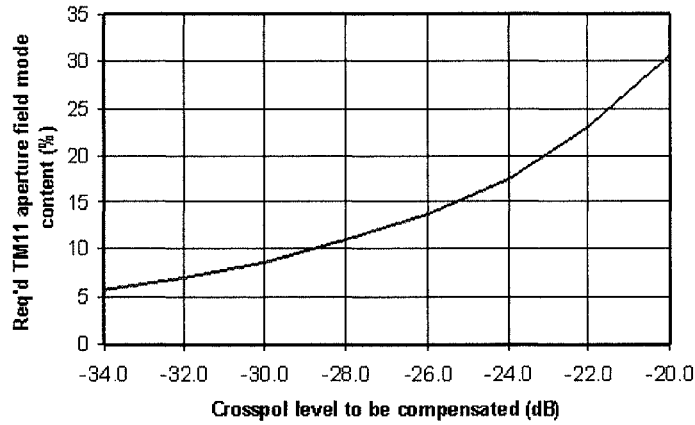
Figure 6.9 *TM11 mode content (%) vs level of crosspolarisation to be compensated*

Having now established a tangible relationship between peak crosspolar levels and the required TM_{11} mode levels for optimum crosspolar compensation, the next section examines how this information can be translated into developing basic design guidelines, particularly for the TM_{11} mode transducer inevitably required as part of the horn design.

6.5 TM_{11} Mode Transducer

The promising results seen in the section 6.3 take no account of the method by which the generation and optimisation of the modal content could be implemented in a practical horn design.

As with the Potter horn [6.3] this can readily be achieved with a circularly symmetric discontinuity, such as a step change in diameter in the throat of the horn as in Figure 6.10, to act as a mode transducer. The dimensions of the step are chosen to excite the required magnitude of the mode whilst the position of the step relative to the horn aperture is chosen to provide the correct phasing of the TM_{11} mode with respect to the existing modes inside the horn.
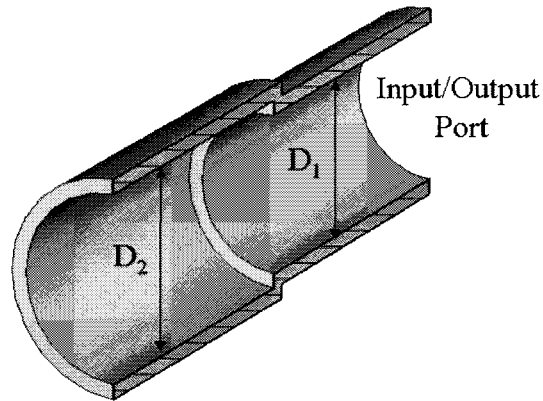
Figure 6.10 *Example of TM₁₁ mode transducer – Circularly-symmetric waveguide discontinuity*

With use of 3D FD-TD analytical software [6.6] the relationship between the mode conversion characteristics and the geometric parameters can be examined. Since it is usual for such programs to quantify mode content in terms of dB, Figure 6.11 provides an equivalent graph to Figure 6.9, converted to dB to allow direct comparison with subsequent results.
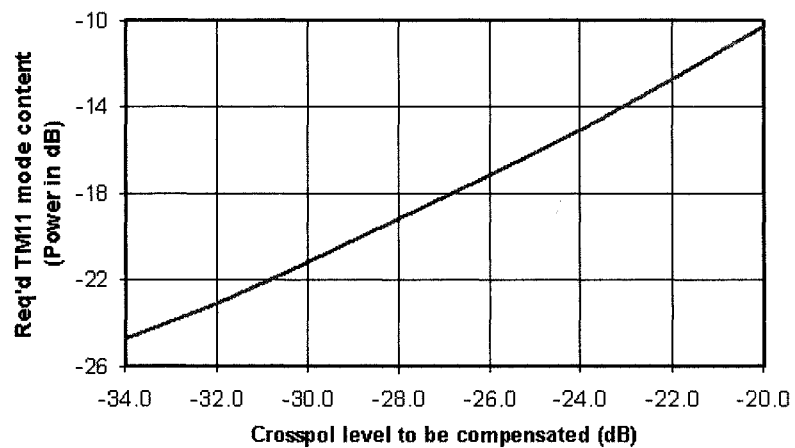
Figure 6.11 *TM11 mode content (dB) vs level of crosspolarisation to be compensated*

6.5.1 TM_{11} amplitude:

With a simple step change acting as the mode transducer, as in Figure 6.10, only diameters D_1 and D_2 can be adjusted to modify the mode-generating characteristics. Despite its simplicity, there are aspects of the resulting conversion from TE_{11} to TM_{11} mode that are useful in helping to understand the frequency limitations of this approach to generating the desired mode content.

With this in mind Figure 6.12 illustrates the amplitude behaviour of the TM_{11} mode versus frequency for typical values of D_1 and D_2. It has been shown that varying D_1 influences the useful bandwidth by changing the frequency, F_2, at which the mode spike occurs. The spike actually indicates the frequency at which the TM_{11} mode reflects back down the input waveguide and therefore represents the cut-on frequency of the TM_{11} mode in the input waveguide. Care must be taken to ensure this condition does not occur at any frequency within the operating band.

D_1 is therefore chosen to adequately support the TE_{11} mode at the lowest frequency of operation whilst ensuring the TM_{11} mode is cut-off at the highest frequency of operation.
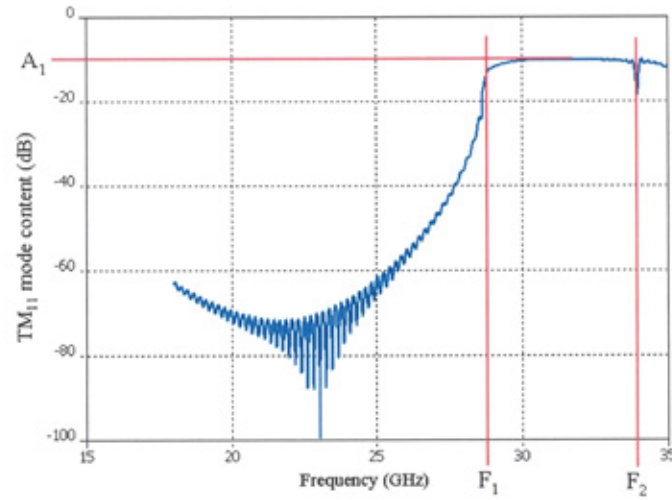
Figure 6.12 *TM$_{11}$ mode transfer function for a circularly-symmetric waveguide step acting as the mode transducer*

Diameter D_2 sets the frequency, F_1, at which the TM_{11} modes cuts-on in the larger waveguide, in accordance with standard waveguide theory [6.7], and is chosen to ensure the TM_{11} mode can propagate at the lowest frequency of the upper sub-band. The amplitude, A_1, indicates the level of power converted to the TM_{11} mode and is determined by the ratio D_1/D_2 as this sets the size of the waveguide discontinuity and therefore the extent to which the fields are disturbed and consequently the potential for energy to transfer to an alternate mode.

As a useful guide, Figure 6.13 provides the variation in mode conversion against the ratio D_1/D_2 where in a) D_2 is fixed at a typical value and in b) D_1 is fixed at a typical value.
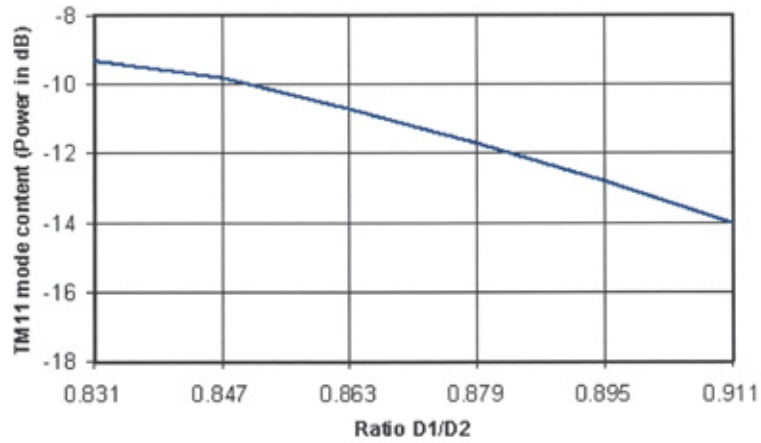
(a)
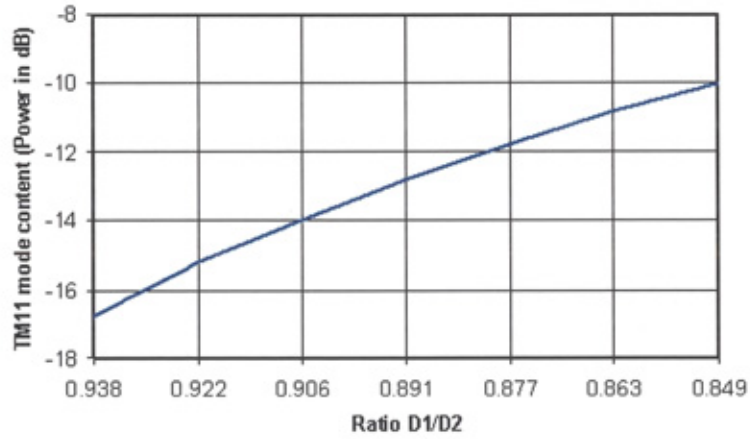
(b)

Figure 6.13 *Level of TM$_{11}$ mode conversion vs D$_1$/D$_2$ with (a) D$_1$ fixed (b) and D$_2$*

fixed

6.5.2 TM$_{11}$ phase:

Assuming the mode amplitude can be controlled with the correct choice of D$_1$ and D$_2$, the useful bandwidth for good crosspolarisation in the upper sub-band is set by the phase relationship between the residual HE$_{11}$ fields and the TM$_{11}$ fields. The bandwidth over which the TM$_{11}$ mode combines favourably with the other field components is dominated by the modal characteristics of the section of waveguide

immediately after the mode transducer in the horn throat (corresponding to D_2 in Figure 6.10) where dispersion between the TE_{11} and TM_{11} modes is at its greatest. Taking account of the guidelines presented in section 6.5.1 with respect to the mode amplitude, the fundamental guideline regarding the mode phase characteristics is that the larger the diameter and the shorter the length of the waveguide section (corresponding to D_2), the greater the potential for the two modes to interact favourably over a wider bandwidth.

This is discussed more in chapter 9 as part of a review of potential improvements to the HE_{11} dual-band horn concept and will not be developed further in this chapter. The findings of chapter 6 are however tested in the next chapter when the theory is put into practice by way of practical horn designs of various geometries.

6.6 References

[6.1] Geen, D.C. and Smith, D.: *Wide flare-angle horn antenna with means for radiating low levels of crosspolarisation in two widely separated frequency bands*, IEEE AP-S International Symposium, 1996, Baltimore, USA, Vol. 3, pp 2026-29.

[6.2] Geen, D.C. and Smith, D.: *Narrow flare-angle, dual-band horn antenna with good crosspolar and VSWR characteristics*, 26th European Microwave Conference, 1996, Prague.

[6.3] Potter, P.D.: *A new horn antenna with suppressed sidelobes and equal beamwidths*, Jet Propulsion Labs publications, June 1963, pp 71-78.

[6.4] Satoh, T.: *Dielectric-loaded horn antenna*, IEEE Trans., 1972, AP-20, pp 199-201.

[6.5] Clarricoats, P.J.B., Olver, A.D.: *Corrugated horns for microwave antennas*, IEE Electromagnetic Wave Series, Vol 18, 1984.

[6.6] *Microwave Studio* by CST – www.cst.de

[6.7] Balanis, C.A.: *Antenna theory – analysis and design*, John Wiley & Sons, 1982.

Chapter 7

Practical investigation - Results

The theory developed in chapter 6 shows the potential for the HE_{11} dual-band horn to offer superior performance over its conventional counterparts of chapters 3 and 4. In this chapter that theory is tested by way of comparisons with practical measurements.

The HE_{11} dual-band concept is applied to different horn geometries and in each case the results compared to equivalent conventional designs, both corrugated and dielectric-loaded. Further comparison between measured and theoretical results is also provided.

Radiation pattern and return loss results are presented for various horn geometries including those with wide (40°) and narrow (14°) semi-flare angles and having either radial or axial corrugations.

After it was determined that higher-order modes can have a significant impact on the overall performance of horns of this type, the theoretical results in this chapter have been generated using a FD-TD simulation package [7.1], rather than the modal analysis used in previous chapters, to fully account for their influence. However, reference is made to the accuracy of the modal analysis throughout.

The discussions on comparative performance will be reserved for chapter 8. This chapter will merely present the results and comment on the agreement with the theory of the previous chapters.

7.1 Radiation pattern results

The radiation patterns have been measured in an anechoic chamber developed solely to support this research [7.2]. Details of the design together with results validating the chamber performance are supplied in Appendix 2.

When comparing the accuracy of the modal analysis of chapters 3, 4 and 6 with the measured results presented here, the main parameter of interest is that of the level of crosspolarisation and its variation with frequency. Comparison of the shape of the radiation patterns, other than observations regarding copolar pattern symmetry, are of secondary importance particularly since the pattern shape is dominated by both the aperture size and flare angle [7.3] and these not having been exactly accounted for in the modal analysis.

7.1.1 Conventional corrugated horn (narrow and wide flare-angle)[1]

By way of a benchmark, Figure 7.1 provides the theoretical and practical radiation patterns for an example of a wide flare-angled conventional corrugated horn and Figure 7.2 provides the theoretical data for an example of a narrow flare-angled conventional corrugated horn.

Whilst measured results are not available for the narrow-angled horn, confidence in the predictions stems from the excellent agreement between measured and theoretical results for other horns tested here and this is not thought to be detrimental to this investigation.

---

[1] For reference and in order to provide a good comparison with results later in this chapter, the conventional horn designs presented in this section are based on the geometry of the HE_{11} dual-band horns illustrated in Figures 7.5 and 7.7, albeit with modified throat and corrugation geometries.
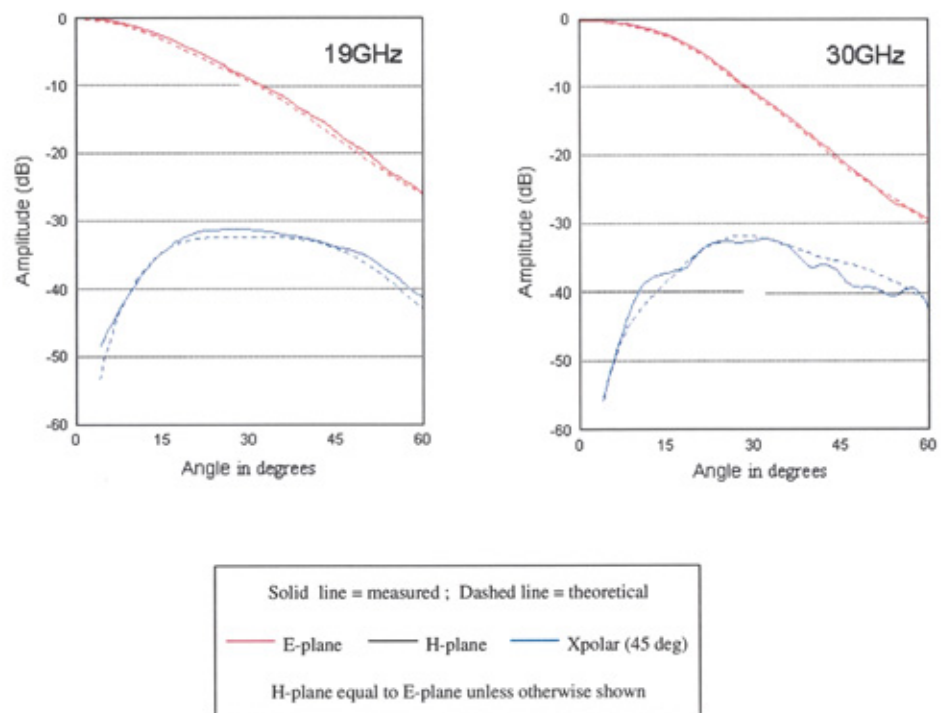
Figure 7.1 *Measured and theoretical radiation patterns for a wide angled*
conventional corrugated horn.
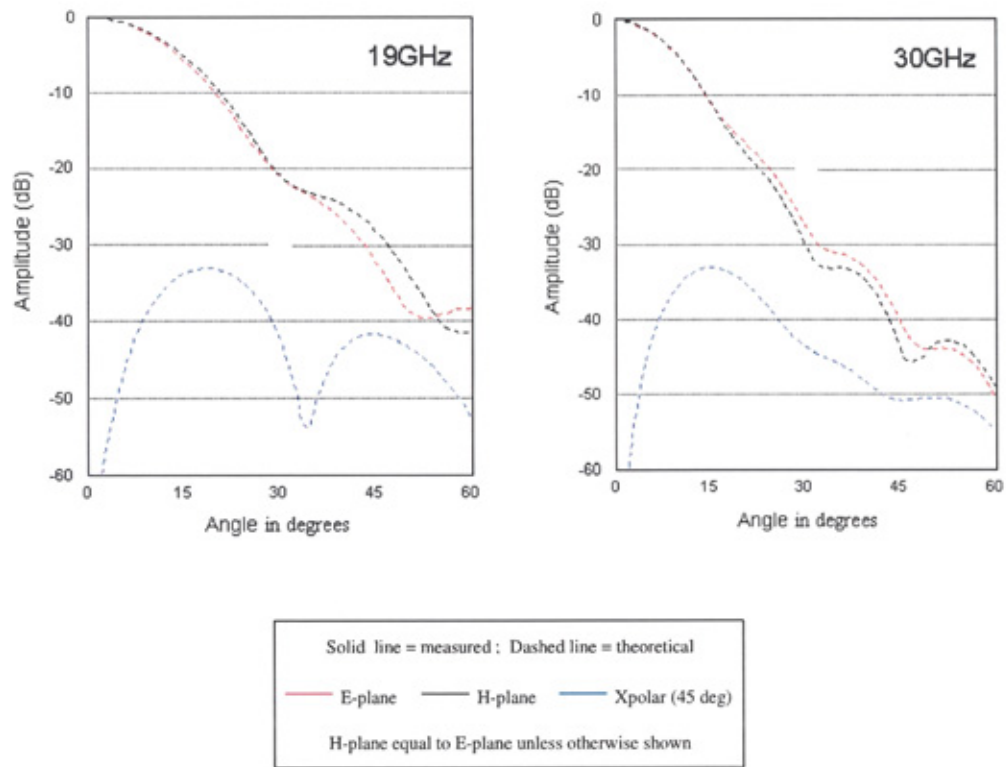
Figure 7.2 *Theoretical radiation patterns for a narrow angled conventional*
corrugated horn.

The results for the conventional corrugated horns of Figures 7.1 and Figure 7.2 should be compared with the theory developed in chapter 3.

Of particular interest is the close agreement with the expected levels of crosspolarisation predicted in Figure 3.6 for values of $f/f_0 - 1 = \pm 0.24$ (representing 19GHz and 30GHz respectively), particularly for the narrow-angled case. For the wide flare-angled example the agreement is not quite as good, a reflection on i) the difficulty to control the aperture distribution in horns having wide flare angles and ii) the use of cylindrical modal analysis applied to a structure that would be better suited to spherical analysis. Nevertheless the agreement is encouraging.

7.1.2 Narrow flare angle dielectric-loaded horn

Following the work of chapter 4 and with a view to providing a thorough comparison of all the horn-types discussed herein, this section examines the performance of a dielectrically-loaded horn with dimensions equivalent to the narrow-angled corrugated horn of section 7.1.1. The structure, as illustrated in Figure 7.3, consists of a smooth walled horn within which is placed a co-axial dielectric cone, separated from the horn wall by an air annulus. As with the corrugated horns considered so far, the beamwidth requirements at a given frequency influence the flare angle and aperture size of the metal horn, after which the dimensions of the dielectric cone are largely dependant on the permitivity of the material used, in accordance with the theory developed in chapter 4.

A key element in the design with regard to crosspolar performance is the method by which the cone is supported [7.4]; the aim being to maintain a constant, co-axial air gap along the length of the flared section of the horn without encouraging higher order mode conversion and a subsequent increase in crosspolarisation.

The horn presented here makes use of two annular rings of width 3.00mm to support the cone whilst maintaining the required air gap. Both the cone and the rings are made from the same material (ε_r = 1.48, polyurethane foam), having been machined from solid as a single item. The position of the rings along the length of the cone is important as this can affect both the crosspolar and VSWR performance. In this case optimum positioning was found empirically using FD-TD software [4].

Since the semi-flare angle is relatively narrow (14°) the aperture surface has been made cylindrical rather than spherical in an effort to ease manufacturing. To reduce the mismatch at the dielectric-to-air interface, and thereby improve the VSWR characteristics, a matching section consisting of ϕ-directed rings has been machined into the aperture surface. The overall aperture diameter is approximately $5\lambda_o$ (at f/f_0-1 = +0.24 (30GHz)).

The theoretical and measured radiation patterns are compared in Figure 7.4.
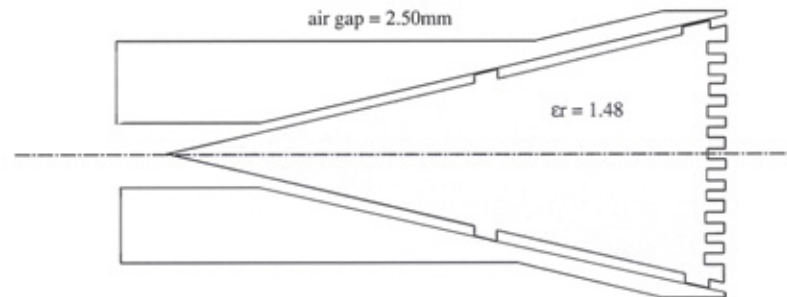
Figure 7.3 *Cross-section of dielectric-loaded horn*
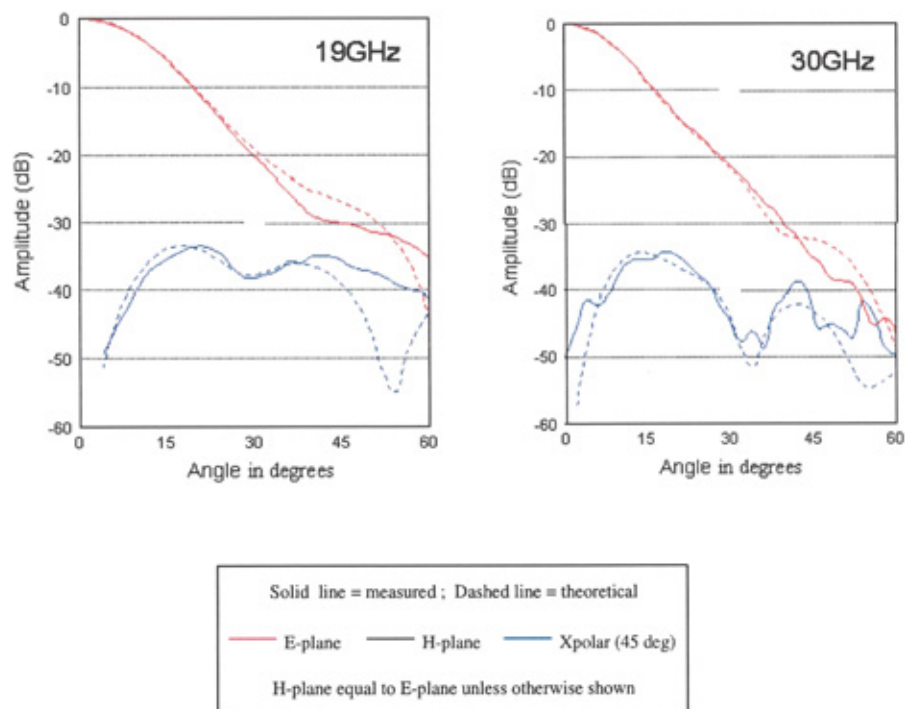
Figure 7.4 *E-plane copolar and 45° crosspolar radiation patterns for the dielectric-loaded horn of Figure 7.3*

The results for the dielectric-loaded horn should be compared with the theory developed in Chapter 4 where Figure 4.4 implies the level of crosspolarisation does not increase as the frequency increases, in contrast to the corrugated equivalent.

However, comparing Figure 7.4 for the dielectrically-loaded horn with that of 7.2 for the equivalent conventional corrugated horn shows there to be only a minor improvement offered by the former.

Although the general performance is good, the apparent superior performance indicated by the modal analysis of chapter 4 is not actually realised. This is thought to be due to the limited bandwidth over which the homogenous to non-homogeneous boundary in the horn throat (at the point of the dielectric core) can suppress the onset of higher order modes, rather than a reflection on the dielectric-to-air boundary condition itself.

7.1.3 HE_{11} dual-band horn

7.1.3.1 Wide flare-angled horn – radially corrugated

A cross section of the proposed horn is shown in Figure 7.5. The semi-flare angle is $40°$, the aperture diameter approximately $5\lambda o$ (at $f/f_0-1 = +0.24$ (30GHz)) and the design is restricted to a single slot depth with less than four corrugations per wavelength at the upper limit. The corrugations are neither radial nor axial with respect to the horn axis but are aligned to be perpendicular to the horn walls.
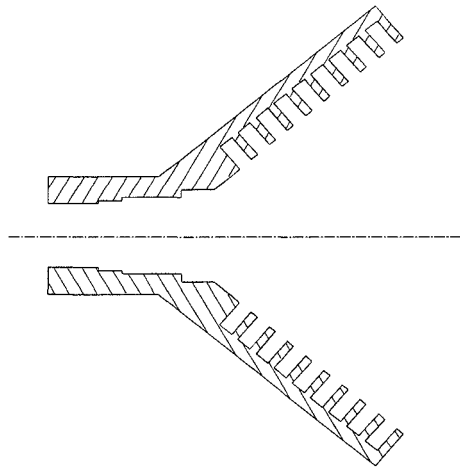
Figure 7.5 *Cross-section of wide flare angle HE$_{11}$ dual-band horn*

Figure 7.6a illustrates the theoretical and practical radiation patterns for the horn of Figure 7.5 at 19GHz and 30GHz, and for academic interest, Figure 7.6b shows equivalent results for the same horn but without the step (mode transducer) in the input waveguide. It is immediately evident that use of the mode transducer has little effect on the radiation patterns at 19GHz but its influence on the aperture distribution and subsequently the radiation characteristics at 30GHz provides more than 10dB improvement to the crosspolarisation along with significantly improved copolar pattern symmetry.
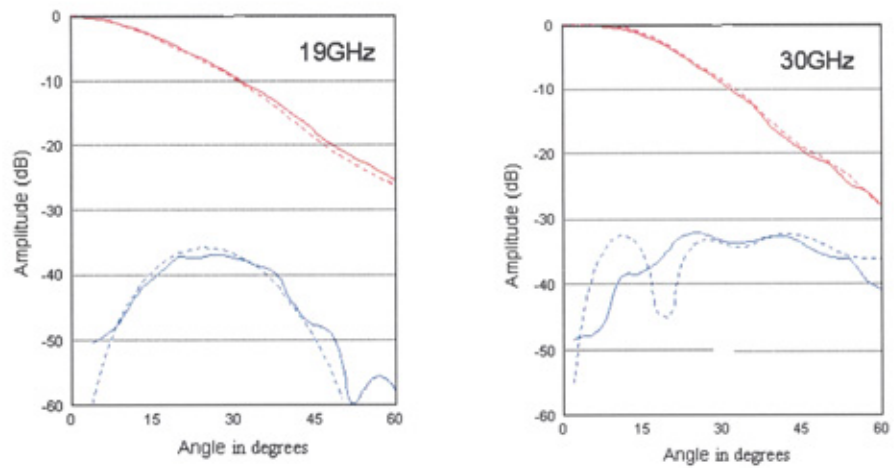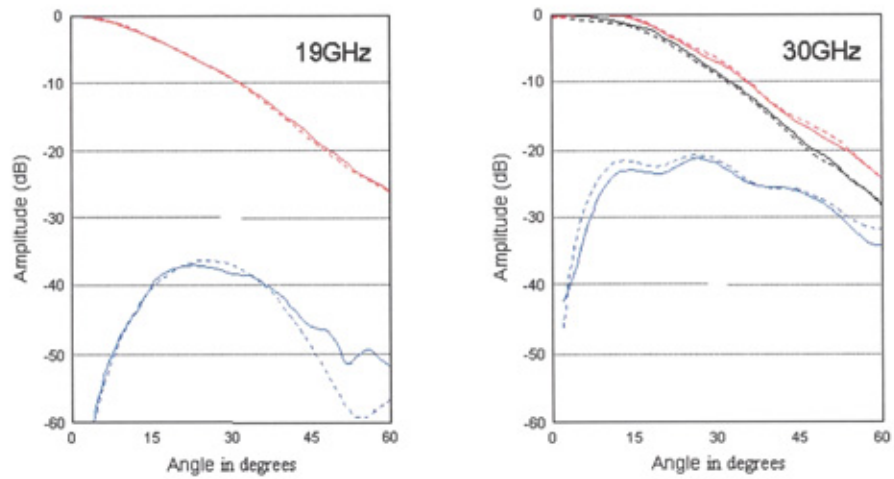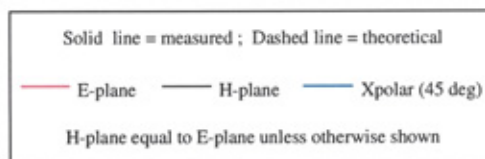
Figure 7.6 *Radiation patterns for the wide-angled horn of Figure 7.5: (a) dual-band horn, (b) as dual-band horn but without mode transducer*

For wide-angled horns it is difficult to control mode purity as the fundamental mode propagates from the throat to the aperture, due largely to the rapid rate at which the impedance of the corrugated boundary changes along the horn and the performance is not as good as for a narrow flare-angle.

7.1.3.2 Narrow flare-angled horn – radially corrugated

To investigate the versatility of the design concept, and in an attempt to represent horns for different applications, a narrow-angled horn, with semi-flare angle 14 degrees and radial corrugations, has been developed. A cross-section of the design is shown in Figure 7.7.

As with the wide-angled horn the aperture is approximately $5\lambda o$ (transmit), however to reduce manufacturing costs the number of corrugations per wavelength has been reduced to less than three at the upper limit.
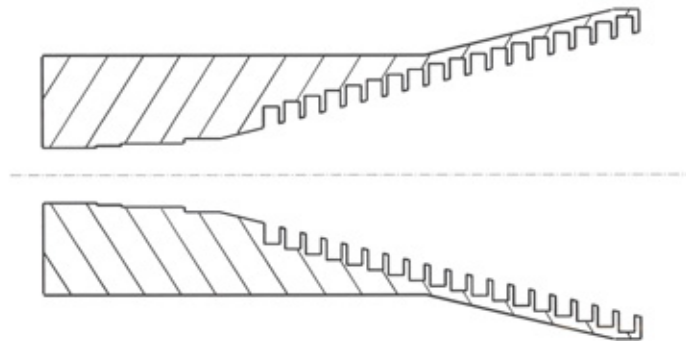
Figure 7.7 *Cross-section of narrow flare angle HE_{11} dual-band horn*

Figure 7.8a illustrates the theoretical and measured radiation patterns for the horn of Figure 7.7 at 19GHz and 30GHz whilst Figure 7.8b shows theoretical results for the same horn but without the step in the input waveguide. As with the wide-angled horn the mode transducer has little effect on the crosspolarisation at 19GHz. However, at 30GHz the introduction of the TM_{11} mode brings about an improvement to crosspolar performance of close to 19dB, thereby reducing the level of crosspolarisation to better than -40dB.
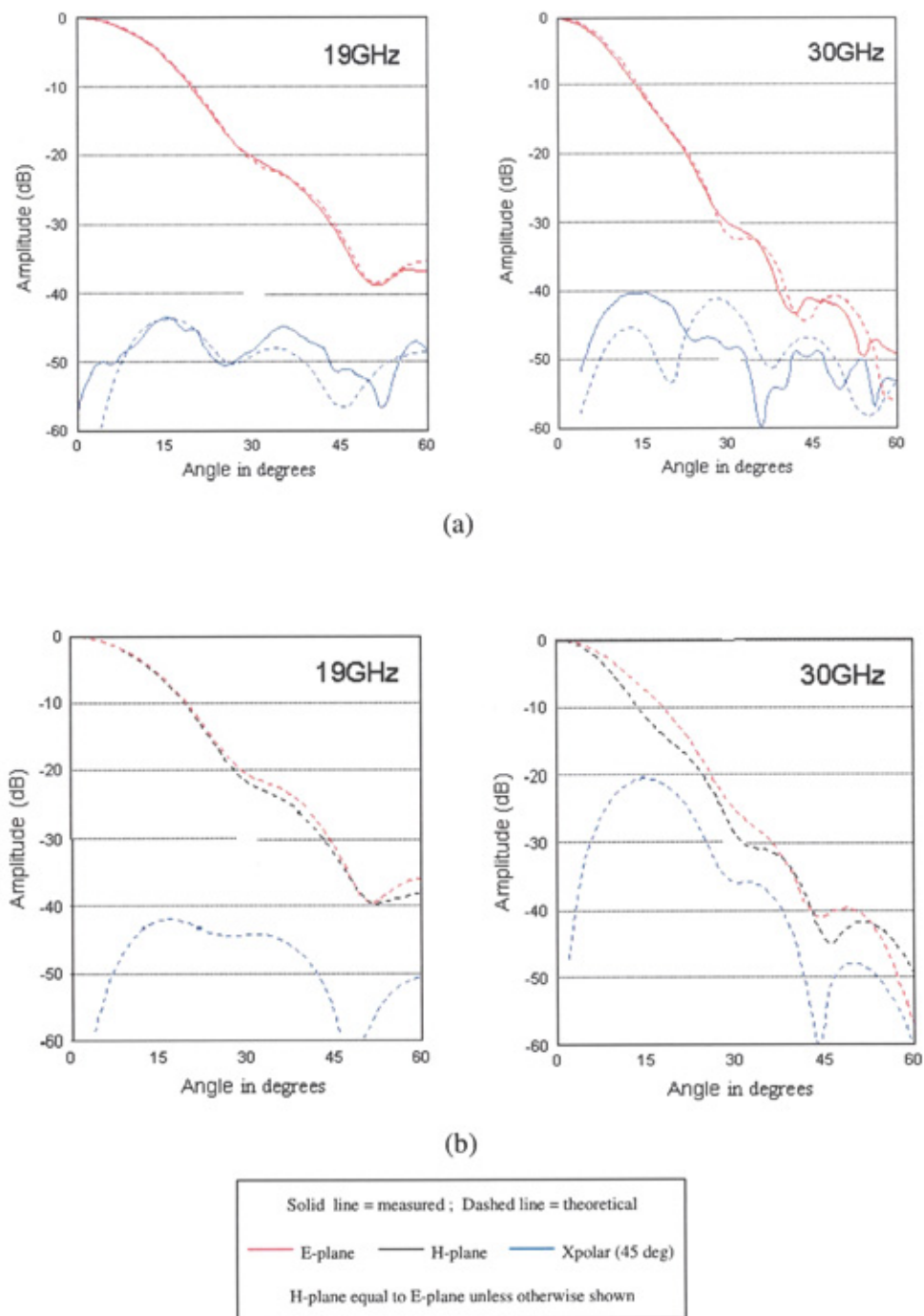
Figure 7.8 *Measured and theoretical radiation patterns for the narrow-angled horn*
of Figure 7.7; (a) dual-band horn, (b) as dual-band horn but without mode
transducer

7.1.3.3 Axially corrugated horn

To contrast with the corrugated horn geometries discussed so far, it is useful to consider a design having axial corrugations. Horns employing axial corrugations tend to have semi-flare angles greater than about 25° in order to properly accommodate the required corrugation geometry without requiring very thin corrugation slots or teeth.

The example presented here has been designed to operate from 19.7-20.2GHz and 29.5-30.0GHz. It has a 33° semi-flare angle and only 4 corrugations, as illustrated in Figure 7.9. The exact corrugation depth was arrived at iteratively using numerical code. The theoretical radiation patterns are provided in Figure 7.10. No measured data is available for this example, however confidence in the theoretical results is high following good agreement for previous horns.
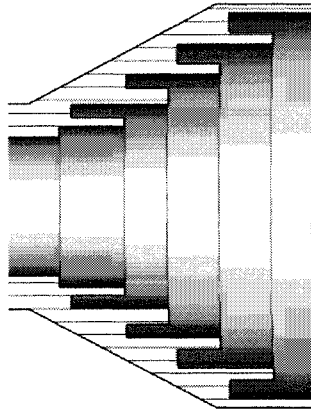
Figure 7.9 *Cross-section of axially-corrugated HE₁₁ dual-band horn*
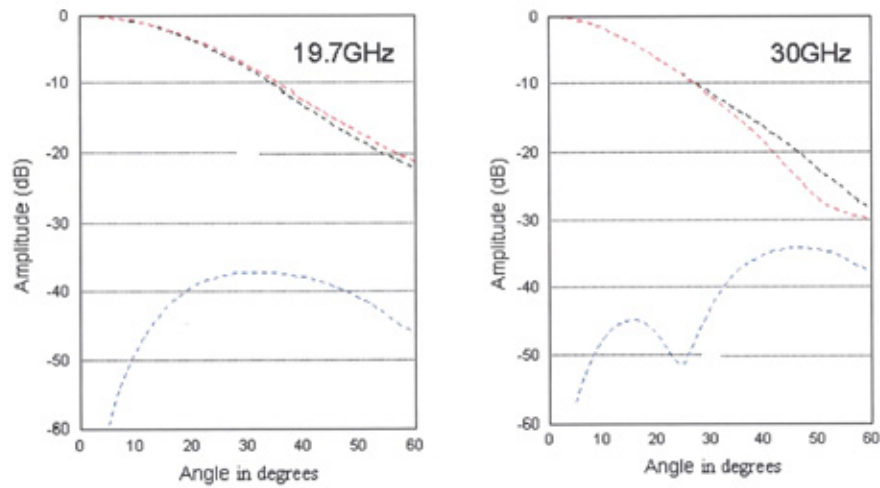
Figure 7.10 *Theoretical radiation patterns for the axially-corrugated horn of*

Figure 7.9

7.2 VSWR results

In addition to the copolar and crosspolar characteristics of section 7.1, consideration has also been given to the VSWR characteristics. Figure 7.11 indicates the theoretical response of reflection coefficient (Γ) versus frequency at the input waveguide for the three wide-angle horns of Figures 7.1 and 7.6. It is evident that, in the lower sub-band the nature of the HE_{11} dual-band design yields a significant improvement over its conventional counterpart. This is at the expense of a minor reduction in the upper sub-band performance, although even here the return loss remains better than -25dB.
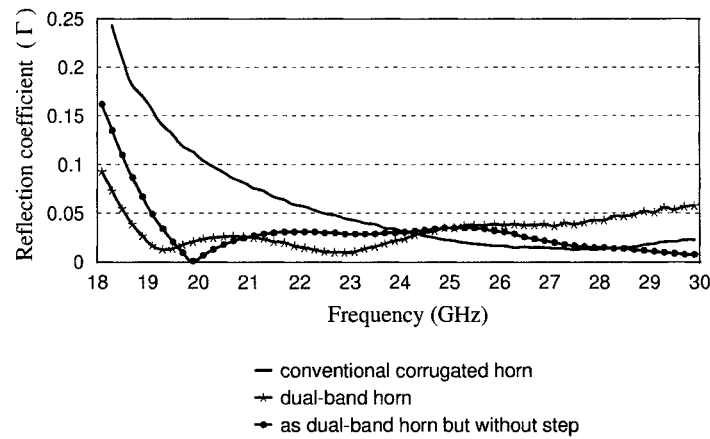
Figure 7.11 *Theoretical reflection coefficient vs frequency for the wide-angled horns*

based on Figure 7.5

Examining the VSWR characteristics for the three narrow-angled horns of Figures 7.2 and 7.8, as given in Figure 7.12, it is again evident that the HE_{11} dual-band horn yields a significant improvement over its conventional counterpart in the lower sub-band and furthermore, also offers a slight improvement in the upper sub-band. The increase in Γ around 22.5GHz is not significant for this application as it occurs outside the frequency bands of interest. Referring to Figure 7.7, it is believed this is caused by the diameter inside the horn throat at which the corrugations begin, a useful parameter to control VSWR.
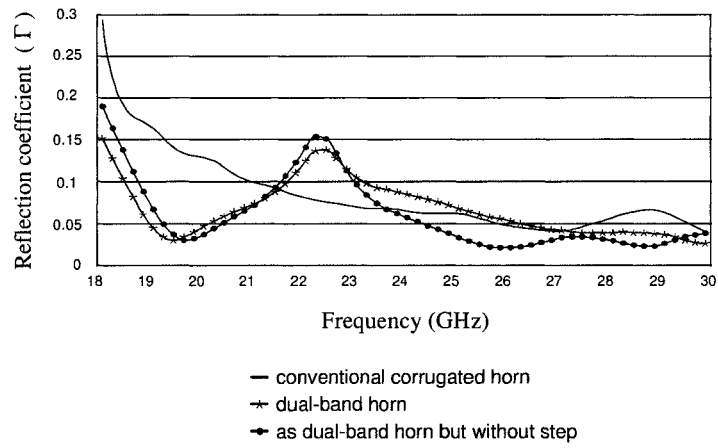
Figure 7.12 *Theoretical reflection coefficient versus frequency for the narrow-angled horns based on Figure 7.7*

Figures 7.13 and 14 provide the theoretical VSWR for the dielectric-loaded and axially corrugated HE_{11} dual-band horns respectively.
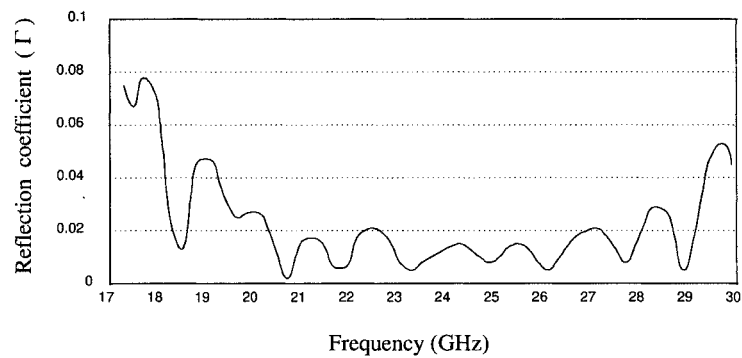
Figure 7.13 *Theoretical reflection coefficient vs frequency for the dielectric-loaded horn of Figure 7.3*
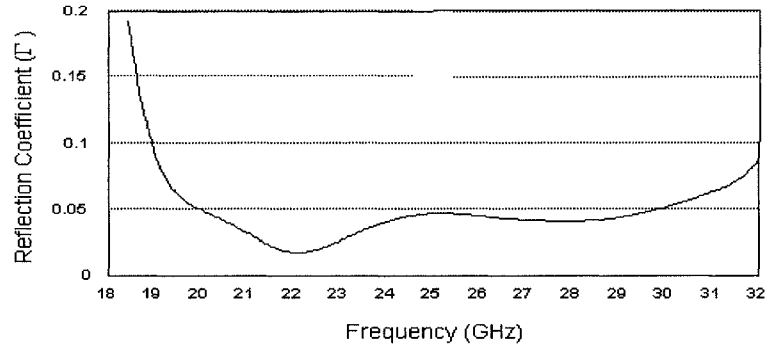
Figure 7.14 *Theoretical reflection coefficient vs frequency for the axially corrugated, dual-band horn of Figure 7.9*

7.3 Results review

The results for the 3 examples of HE_{11} dual-band corrugated horns should be compared with the theory developed in chapter 6.

First considering the wide-angled case and comparing Figure 7.6a with that of Figures 6.3 and 6.6. It is evident that the practical results fall short of the performance anticipated with the modal analysis by as much as 10dB at the upper frequency and 3-4dB at the lower frequency. This is further testament to the difficulty in controlling the aperture field distribution in wide-angled horns to the extent that crosspolarisation is reduced to levels below -40dB, particularly as the frequency of operation increases.

Considering the narrow-angled case and comparing Figure 7.8a with that of Figures 6.5 and 6.6, much better agreement in the level of measured versus anticipated crosspolar levels is observed. With the measured peak crosspolarisation being well below -40dB at both 19GHz and 30GHz, the improved control of the aperture field distribution and superior mode purity achievable in narrow-angled horns is clearly demonstrated.

Also in reasonable agreement is the crosspolarisation in Figure 7.8b versus that indicated in Figure 6.4 (also see Figure 6.5) at $f/f_0 - 1 = -0.24$ (19GHz) and $f/f_0 - 1 = +0.24$ (30GHz), for the case where the TM_{11} mode is *not* added to the existing

aperture field, when levels increase to -23dB according to the modal analysis versus -21dB according to FD-TD analysis.

The higher level predicted by the FD-TD analysis is believed to be a result of the practical horn of Figure 7.8a having an aperture size 25% larger than the horn considered in the modal analysis of chapter 6. As a consequence it better satisfies Equation 3.11 and the response of Figure 6.4 is expected to be centred closer to the frequency at which $\overline{Y} = 0$; the corresponding level of crosspolarisation at f/f_0-1 = +0.24 (30GHz) therefore being higher. It is also believed some of the difference can be attributed to the need to modify the physical geometry of the throat of the FD-TD model in order to remove the mode transducer to simulate the absence of the TM_{11} mode, thereby artificially changing the horns performance at the highest frequency. This is not so for modal analysis where the mode is added/subtracted analytically without account of subtle changes to the physical structure.

Continuing the comparison with the analysis of chapter 6, Figure 6.9 suggests that to improve the crosspolarisation from that offered in Figure 7.8b to that offered in Figure 7.8a for the horn of Figure 7.7, the aperture field mode content should be modified to include 27% TM_{11} mode. From Figure 6.11 the equivalent mode power is approximately −12dB, which from Figure 6.13, requires the ratio of D_1/D_2 in the mode transducer to be approximately 0.88.

With the dimensions of the mode step for the horn of Figure 7.8a derived iteratively using an FD-TD model of the complete horn, D_1 was chosen to be 11.62mm and D_2 was set at 13.20mm. The ratio D_1/D_2 is therefore exactly 0.88 – in excellent agreement with the modal analysis.

By way of a final and striking indication as to the manner in which the HE_{11} dual-band horn can be made to offer superior performance, Figure 7.15 shows the crosspolarisation versus frequency for the horn of Figure 7.9. It is interesting to compare this with Figure 3.6 for the conventional corrugated horn as it shows vividly the change to the crosspolar response as a consequence of modifying the slot

depth to favour the lower sub-band (Rx) and subsequently introducing the TM_{11} mode to optimise the upper sub-band[2].
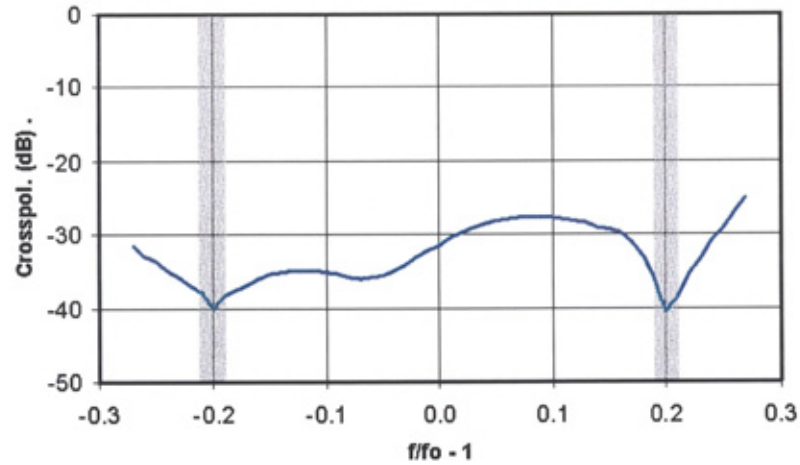
Figure 7.15 *Peak crosspolarisation vs normalized frequency for the axially-corrugated HE_{11} dual-band horn of Figure 7.9. (Obtained using FD-TD code)*

Having examined various types of horn in an effort to get a thorough appreciation of the design issues, only when the performance trade-offs are considered in the context of the application outlined in chapter 1, in particular the design boundary conditions, can proper conclusions be developed, as in Chapter 8.

---

[2] When comparing with Figure 3.6 note that the axially corrugated horn of Figure 7.15 was designed to operate from 19.7-20.2GHz for Rx and 29.5-30.0GHz for Tx. Consequently the vertical bars defining the operational bandwidths are positioned differently.

7.4 References

[7.1]   Gwarek, W.K.: *V2DE Solver*, FD-TD code for EM analysis of axisymmetrical antennas. Developed at Warsaw Polytechnic, Poland, 1995.

[7.2]   Geen, D.C and Smith, D.: *Design, construction and performance of a small, low cost anechoic measuring system for research applications*, IEEE AP-S International Symposium, 1995, Newport Beach, California, USA.

[7.3]   Clarricoats, P.J.B., Olver, A.D.: *Corrugated horns for microwave antennas*, IEE Electromagnetic Wave Series, Vol 18, 1984.

[7.4]   Cahill, R.: *Design of core support mechanism for mm-wave dielectrically loaded horn*, Electronic Letters, 1989, Vol. 25, No. 18, pp. 1248-9.

Chapter 8

Practical investigation – Comparative evaluation and review

Following the results of Chapter 7 the comparative performance of the various horns is subsequently examined by way of i) an evaluation of the RF results, ii) a review of each of the horn-types against the original design boundary conditions outlined in chapter 1 and iii) a review of the significance of the horn described in Chapter 6 with respect to the critical issue identified in Chapter 5.

8.1 Evaluation of the RF results

Neglecting the copolar radiation pattern beamwidth, on the understanding that it can be controlled by way of the aperture size and flare angle to suit a given reflector optical geometry [8.1], the key parameter of interest for this research is the level of crosspolarisation which in turn has been used as the metric by which to quantify copolar pattern symmetry.

Initially, using crosspolarisation as the sole figure of merit, the results of Chapter 7 show how i) wide flare-angled conventional corrugated horns do not perform quite as well as narrow flare-angled horns, offering approximately -30dB and -33dB crosspolar levels respectively, ii) dielectric-loaded horns have the potential to offer performance similar to, or better than, the equivalent conventional corrugated horn, offering approximately -34dB crosspolar levels, iii) the HE_{11} dual-band concept provides superior performance to conventional designs offering -32dB and better than -40dB for wide and narrow flare-angled designs respectively, and iv) the HE_{11} dual-band concept can be applied equally well to horns having axial corrugations as to those having radial corrugations.

The overall significance of points iii) and iv) will be discussed in greater detail throughout this chapter. However, to fully evaluate the RF performance the results

should be considered in the context of return loss *in addition to* crosspolarisation since the two are inter-related, as discussed next.

8.1.1 Conventional corrugated horns:

Considering first radially corrugated horns, Figure 7.11 and 7.12 compare the return loss of the conventional corrugated horn with that of the equivalent HE_{11} dual-band horn for the wide flare-angled and narrow flare-angled designs respectively. In both cases the return loss at the lower operating frequencies is significantly worse for the conventional designs versus that of the HE_{11} dual-band designs. For the conventional horns presented here, this is not too surprising since they have been designed for minimum crosspolarisation with little concern for return loss. However, the same can be said of the HE_{11} dual-band equivalents and their return loss is significantly better.

The root of the poor return loss for the conventional horns can be traced to the transition from smooth-walled to corrugated waveguide in the horn throat where the mode is encouraged to transform from TE_{11} to HE_{11}. Simple transmission line theory indicates the most effective geometry by which to achieve this transformation is to start with a corrugation slot depth of $\lambda/2$ and, with each successive corrugation, slowly taper to the required slot depth to adequately support the HE_{11} mode which, from Equation 3.13, is $\lambda/4$. Whilst this may address the poor return loss at the lower operating frequencies, the effect of the deeper slots is to encourage higher order modes at the higher frequencies, thereby leading to degraded crosspolarisation. As a consequence, the crosspolar performance for the conventional corrugated horns presented in Chapter 7 would likely get worse at 30GHz if the designs were modified to provide improved return loss at 19GHz.

[This provides justification for the anlaysis of Chapter 5 which, for a conventional corrugated horn, initially assumed a feed model having only –25dB crosspolarisation as part of the investigation into axial ratio in elliptical reflectors].

Examining the narrow-angled horn of section 7.1.1, the radiation pattern results and excellent agreement with the modal analysis of Chapter 3 indicate that only the fundamental HE_{11} mode is present in the horn, even at the highest frequency of

operation where the risk of higher order modes is greatest. However, the return loss is relatively poor, too poor for use in a practical antenna.

The absence of higher order modes suggests there is scope to improve the return loss by modifying the throat to include deeper slots without degrading crosspolarisation. Furthermore, any small increase to the peak crosspolarisation at the highest frequency can, to some extent, be counteracted by reducing the depth of the corrugations closer to the horn aperture, although this tends to result in degraded crosspolarisation at the lowest frequency of operation. Clearly the optimum design is a compromise.

This trade-off between return loss at the lower band edge versus crosspolarisation at the upper band edge is the classic design trade-off for conventional corrugated horns and is what, in practice, ultimately limits their operational bandwidth.

8.1.2 Dielectric-loaded horns:

Considering the dielectric-loaded horn, section 7.1.2 concluded that whilst offering good crosspolar performance, it only offered a slight improvement over the equivalent conventional corrugated horn. When reviewed in the context of return loss however, the dielectric-loaded horn is shown to offer improved crosspolarisation whilst also providing good return loss. In this respect, the dielectric-loaded horn can be viewed as being superior to its conventional corrugated equivalent.

Figure 7.13 illustrates the return loss for the horn of Figure 7.3. The ripples in the trace are caused by the discontinuity at the dielectric-to-free space boundary at the horn aperture, the impact of which has been minimised by way of a matching layer of approximate $\lambda/4$ deep grooves cut into the face of the dielectric core. Comparing this with the results of Figure 7.12 for the equivalent conventional corrugated horn demonstrates how the dielectric-loaded horn has the potential to provide superior performance.

This is however, not always the case for all horn geometries and all choices of dielectric material. From experience, the concept of dielectric-loading is better suited to horns having only moderate semi-flare angles, thought to be a result of the soft boundary not being able to control the mode content in the same way corrugations do for horns with wide semi-flare angles. In addition, as the relative permitivity of the dielectric core increases, so the greater the discontinuity at the dielectric-to-air interface at the horn aperture and the smaller the bandwidth over which it is possible to achieve a given level of return loss.

There are also additional concerns regarding the practical limitations of the dielectric-loaded horn in the context of the design boundary conditions of Chapter 1 and these will be discussed in section 8.2.

8.1.3 HE_{11} dual-band horns:

In contrast to the conventional horns of Chapters 3 and 4, the fact that the corrugation slot depth in the HE_{11} dual-band horn of chapter 6 is optimised solely for the lower frequency band, good return loss *and* good crosspolarisation are assured there, and by the addition of the appropriate portion of TM_{11} mode at the upper frequency band, good crosspolar performance is assured there. Furthermore, from the three examples provided in Chapter 7 (see Figure 7.11, 7.12 and 7.14), the combination of the step in the input waveguide (acting as the TM_{11} mode transducer) together with the corrugations themselves, appears to provide good return loss at the upper frequency band as well.

The concept operates better for narrow-angled horns than for wide-angled horns due largely to the fact that the fields are subject to far less mode conversion as they propagate from the throat to the aperture and generally exhibit superior radiation characteristics for dual-mode applications. Of particular note is the comparison against peak crosspolarisation of the narrow-angled conventional versus dual-band horns provided in Figures 7.2 and 7.8a respectively, where the dual-band design offers an advantage to crosspolarisation of >7dB at 30GHz and >10dB at 19GHz.

The performance and versatility of the new horn are reinforced following the results of the axially corrugated horn of Figure 7.9, a particularly simple design with relatively small aperture of $k_0 r = 6.5$ at the lowest frequency of operation.

Although measured results are not available for this example, theoretical predictions using FD-TD code show crosspolar levels better than −37dB in the angular range typical of that corresponding to the edge of a reflector. The patterns of Figure 7.10 also suggest there is scope to increase the depth of the corrugations to further improve the lower band crosspolarisation. Nevertheless, the overall performance, including that of the return loss in Figure 7.13[3], highlights the adaptability of the HE_{11} dual-band concept, and shows how it can be used to improve crosspolarisation, pattern symmetry and return loss in horns having a variety of corrugation geometries.

8.2 Review against the design boundary conditions of Chapter 1

In addition to the RF performance criteria and in an effort to provide the most useful all-round comparison of the different design methodologies in the context of the application being considered here, it is useful to examine each of the horn-types against each of the design boundary conditions of Chapter 1.

In addition to detailed discussion points, Table 8.1 provides a summary of the findings at the end of the section for reference. For convenience, the design boundary conditions are repeated here as;

1 Control of copolar patterns to suit a wide variety of reflector optical geometries

2 Low crosspolarisation to allow frequency reuse

3 Good VSWR (return loss)

4 Low insertion loss

---

[3] When comparing the return loss results for the different horns presented herein note that the axially corrugated example was designed to operate from 19.7GHz rather than 18.3GHz.

5   Environmentally hardy (outdoor 10 year life-cycle)

6   Lends itself to low cost, high-volume manufacture

8.2.1 Wide angled conventional corrugated horns:

Whilst this type of horn may offer the desired copolar patterns to match to a particular reflector optical geometry, it is difficult to achieve crosspolarisation as good as −30dB for a horn also having good return loss across the 20/30GHz bands. As with the majority of corrugated horns, the insertion loss is inherently low (typically <0.1dB) and with an appropriate window covering the aperture the performance is little affected by normal environmental conditions. With the corrugations orientated perpendicular to the horn walls, the parts must typically be machined and are consequently expensive and not suitable for low-cost, high-volume manufacture.

When reviewing Table 8.1 it is worth pointing out that the wide-angled conventional corrugated horn can also be implemented using axial corrugations, thereby satisfying the requirements for low-cost, high-volume manufacturing. However the RF performance would be similar to that presented here for the radially corrugated equivalent.

8.2.2 Narrow angled conventional corrugated horns:

Generally superior to wide-angled examples both in terms of crosspolarisation and return loss. Crosspolarisation levels are expected to be better than −30dB for a horn also having good return loss. However, in comparison with wide-angled designs, they may not offer the desired copolar beamwidth characteristics and are generally more complex to machine and therefore more expensive.

8.2.3 Dielectric-loaded horns:

Generally suited to narrow flare angles and, after having been shown to support the same HE_{11} mode content as the conventional corrugated horn, share similar copolar pattern characteristics. Whilst they have been shown here to offer superior crosspolar

and return loss characteristics than the equivalent corrugated horn, the achievable performance and suitability of this type of horn is set almost entirely by the choice of material used for the dielectric core.

Because of the significant implications the choice of material has on the RF performance, the environmental robustness and the manufacturability of the horn, as part of the review against the design boundary conditions, it is worthy of further discussion.

So far, a low cost, lightweight horn with good crosspolar and return loss performance has been presented. Its RF performance confirms its suitability as a replacement for the conventional corrugated horn, particularly for the 20/30GHz band where its superior bandwidth potential can be utilised.

Whilst the analysis of Chapter 4 provides a useful insight into the operation, design and potential performance of the dielectric-loaded horn, the practical constraints imposed by the inclusion of a solid volume of dielectric material limit both the performance and applications of this type of horn in the context of high-volume, low cost manufactured parts as discussed herein.

In particular, to suit high volume production techniques it is important for the material to lend itself to a low-cost production technique such as moulding. Also, for wideband applications there is the need to use a material having a low dielectric constant so as to yield good return loss at the dielectric-air interface at the aperture of the horn.

These requirements are often in conflict. The return loss specification may be best served with $\varepsilon_r < 1.5$, although the materials having such properties are often dense foams which can not easily be moulded and certainly not with guaranteed homogeneity. Conversely, those materials having the potential to be moulded tend to be solid plastics with $\varepsilon_r > 2.2$, thereby providing potential return loss problems. Whatsmore, even for those materials with $\varepsilon_r > 2.2$, there can be considerable difficulty in moulding a solid cone without introducing voids, shrinkage or sinkage into the part. Since one of the conditions to maintain mode purity and therefore good

125

crosspolarisation requires the dielectric core to be homogeneous, voids and inconsistencies cannot be tolerated.

There is also a need to employ a material with low insertion loss (dissipation factor << 0.001) in order to minimize the overall antenna noise temperature. Considering that dissipation losses prior to the Low Noise Amplifier not only reduce antenna gain but also increase the overall antenna noise temperature, any insertion loss attributed to the core material yields twice the reduction to the antenna G/T (the figure of merit usually given to reflector antennas for satellite communications).

Add to this the concerns of exposing the dielectric material to a harsh outdoor environment, even if protected by the metal horn and a feed window, and there is significant scope for concern over the suitability of the design, particularly when antennas such as this have a 10 year life cycle with zero maintenance.

The difficulty in sourcing environmentally-stable, low loss dielectric material suitable for high-volume manufacturing, together with the need to produce consistent and homogeneous dielectric cores in a material having a relatively low dielectric constant, jeopardises the anticipated superior performance of the dielectric-loaded horn and consequently steers the designer away from this option, in favour of the corrugated.

8.2.4 HE_{11} dual-band horns – radial corrugations:

Provided the mode transducer takes the form of a step in the input waveguide and no additional components or dielectric materials are used to excite the TM_{11} mode at the upper frequency band, the HE_{11} dual-band horn with radial corrugations offers the same environmental stability and manufacturing limitations as described for the conventional corrugated horns in section 8.2.1 and 8.2.2. Considering the RF advantages described earlier in the chapter, this makes this type of horn the best candidate for applications where volumes are low enough not to warrant tooling, and machining the parts is economically viable. For high-volume applications a modification to the corrugation geometry is required.

8.2.5 HE$_{11}$ dual-band horns – axial corrugations:

The use of axial corrugations in preference to radial corrugations opens the way for this horn to be manufactured in high volumes using techniques such as high-pressure die-casting to yield very low cost parts. With the introduction of suitable draft angles to assist in the manufacturing process, the orientation of the corrugations lends itself to the casting process by allowing the tool to withdraw from the die to release the part without sacrificing the tool itself.

With the RF performance on a par with the equivalent HE$_{11}$ dual-band horn having radial corrugations and the environmental stability as good as any of the corrugated horns discussed here, the suitability for high-volume production techniques makes the HE$_{11}$ dual-band horn with axial corrugations the only horn-type to satisfy all 6 design boundary conditions, as highlighted in Table 8.1, and whatsmore, it does this comprehensively.

	Copolar Pattern Control	Low Crosspolar	Good Return Loss	Low Insertion Loss	Environmentally Robust	Suited to High-Volume Manuf.
Conventional Corrugated - Wide Flare Angle	●	○	○	●	●	x
Conventional Corrugated - Narrow Flare Angle	●	○	○	●	●	x
Dielectric-Loaded - Narrow Flare Angle	●	○	○	x	○	○
HE$_{11}$ Dual-Band (Radial) - Wide Flare Angle	●	※	●	●	●	x
HE$_{11}$ Dual-Band (Radial) - Narrow Flare Angle	●	●	●	●	●	x
HE$_{11}$ Dual-Band (Axial) - Mid Flare Angle	●	●	●	●	●	●

●	Compliant
○	Trade-off with other parameter
※	Marginal
x	Non-compliant

Table 8.1 *Compliance matrix of horn-type against the six design boundary conditions of Chapter 1*

8.3 The HE_{11} dual-band horn as a solution to the critical issue of Chapter 5

Chapter 5 concluded that, for systems employing circular polarisation, the need for improved radiation characteristics from the primary feed horn is dictated by the system specification, the performance of the polariser itself and the optical geometry of the antenna (often chosen to accommodate additional scanned services rather than optimise the primary on-axis service). Ultimately however, with the demand for ever-increasing satellite network capacity placing additional emphasis on the crosspolar performance of the antenna, there is inevitably an advantage to be gained by improving this aspect of the antenna performance.

The results of Chapter 5 suggest the improved crosspolarisation and copolar pattern symmetry of the HE_{11} dual-band horn of Chapter 6 should yield superior secondary on-axis axial ratio when used as the feed for an elliptical reflector antenna. Figure 8.1 shows the secondary radiation patterns for an elliptical reflector[4] (E=1.6) illuminated by the primary radiation patterns of Figure 7.10. In contrast to Figure 5.10 and 5.12, which in the author's view represent the state-of-the-art for conventional horn designs, the superior performance of this new horn causes degradation to the secondary on-axis CP crosspolarisation of less than 0.2dB.

---

[4] With respect to the results in Chapter 5, the results in Figure 8.1 are taken from a slightly larger reflector with slightly larger F/D ratio. The conclusions with respect to the on-axis axial ratio presented here are not altered as a consequence.
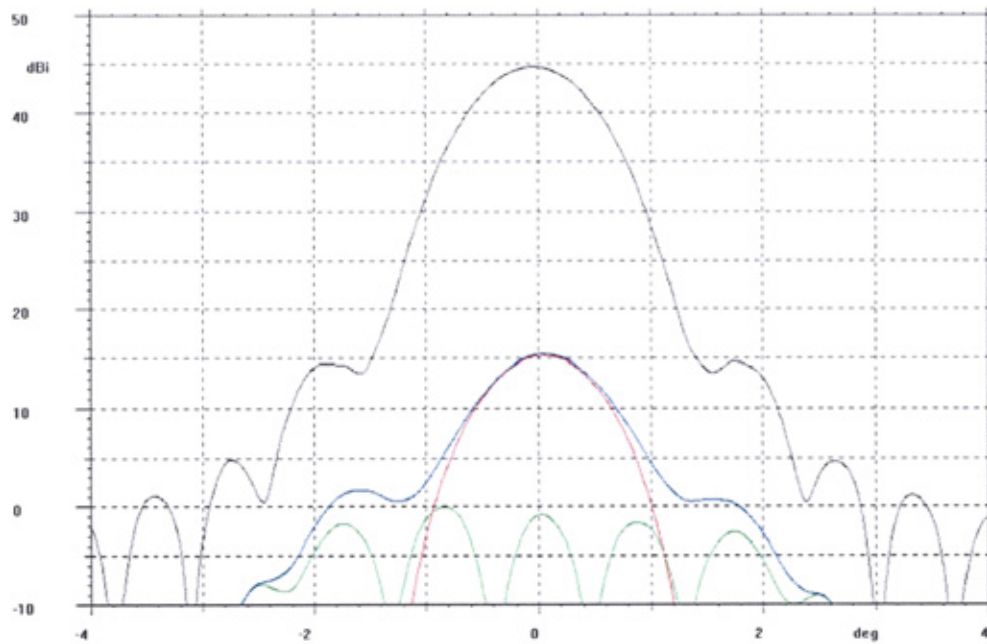
Figure 8.1 *±4° antenna radiation patterns in the plane of the major axis of the ellipse with E=1.6. Reflector illuminated with the patterns from Figure 7.10 for the dual-band, axially corrugated horn of Figure 7.9. i) horn only - green trace, ii) 0.5dB axial ratio contribution from the polariser only – red trace, and iii) combined effect of i) and ii) – blue trace.*

Depending on the various parameters discussed in Chapter 5 the consequences of using a conventional horn as the feed for an elliptical reflector antenna could yield degradation to axial ratio of up to 3dB. With the desire to improve the capacity of a given network to satisfy the anticipated increased demand for these services, and the upper capacity bounds being partially set by the crosspolar isolation between RHCP and LHCP, the improved axial ratio realisable as a consequence of the HE_{11} dual-band horn represents a significant development in the overall antenna design.

Not only has it been shown to offer improved RF characteristics over its conventional equivalents, but it provides these with no additional cost burden; the concept having been successfully applied to a horn having axial corrugations and this lending itself to high volume manufacturing techniques; and with no additional risks (manufacture or environmental), since no extra parts or materials are required.

8.4 References

[8.1] Clarricoats, P.J.B., Olver, A.D.: *Corrugated horns for microwave antennas*,

IEE Electromagnetic Wave Series, Vol 18, 1984.

Chapter 9

Final Summary and Further Work

This last chapter provides a final summary of the findings of this research work together with general conclusions. This is followed by ideas for further work, the chapter ending by way of a closing statement.

9.1 Summary and Conclusions

In the pursuit of the design of a suitable horn antenna to satisfy the design boundary conditions listed in Chapter 1, Chapters 3 and 4 have examined the specific cases of corrugated and dielectric-loaded horns respectively and concluded that the root of their desirable radiation characteristics stems not just from their ability to encourage and support the HE_{11} mode, but more importantly, their ability to do this over an extended frequency band.

It is this ability to operate with such good performance over such an extended bandwidth that has attracted so much interest from both researchers and industry, and is what makes the corrugated and dielectric-loaded horns so useful. However, there is inevitably a limit to the operational bandwidth set either by the variation in the surface impedance characteristics with frequency or by practical limitations.

In the case of the corrugated horn, as highlighted in Figure 3.4, the change in electrical depth of the corrugations causes $\overline{\Lambda}$, the hybrid factor, to deviate appreciably from the optimum value of 1, thereby leading to the performance as in Figure 3.6. In practical terms, this means that as the frequency of operation extends above or below the centre frequency (at which the corrugation depth close to a quarter wavelength), the pattern symmetry and crosspolar levels degrade; the useful bandwidth being dictated by the required performance for a particular application.

Figure 4.4 suggests otherwise for the dielectric-loaded horn for which $\overline{\Lambda}$ remains close to 1 for all frequencies above the centre frequency. Referring back to Equation 4.25, this is only to be expected after the surface impedance of the dielectric-air interface is found to vary as the slow, monotonically-varying, hyperbolic tangent function. However, in practice (and in addition to practical limitations), the useful bandwidth of this type of horn is restricted by the ability to excite only the dominant mode in the horn throat and not necessarily by the boundary condition itself.

Chapter 5 examines in detail the implications on antenna performance of using the conventional designs described in chapters 3 and 4 as primary feeds to illuminate elliptical, offset, reflector antennas typical of those due to be deployed for the next generation of Ka band satellite networks. It highlights two design constraints that particularly affect crosspolarisation for circularly polarised antennas (axial ratio) and goes on to suggest that the conventional corrugated or dielectric-loaded designs may not be able to offer the required RF performance to be employed as the primary horns for this application.

The need to operate over ever-increasing bandwidths has led researchers to pursue techniques that increase the operational bandwidth accordingly, even to the extent of combining the two concepts in a corrugated / dielectric-loaded horn [9.1].

Drawing on the findings of Chapters 2, 3 and 4 and in the search for an improved design for this particular application Chapter 6 introduces a novel, hybrid technique that is shown to offer considerable advantages over conventional designs, particularly with a view to addressing the critical issue identified in Chapter 5.

As is common to many satellite network architectures the two bands of interest, corresponding to the receive bandwidth and the transmit bandwidth, are separated in frequency thereby affording the opportunity to make use of two exclusive mechanisms to independently optimise the performance at each sub-band. This is particularly relevant at Ka-band because of the especially wide frequency separation between the sub-bands. The anticipated improvement to crosspolarisation is confirmed following the comparative evaluation and review of the practical results in Chapter 8 where section 8.1.1 introduces the interdependency between return loss

and crosspolarisation, particularly for the conventional corrugated horn, concluding that;

'The trade-off between return loss at the lower band edge versus crosspolarisation at the upper band edge is *the* classic design trade-off for conventional corrugated horns and is what, in practice, ultimately limits their operational bandwidth.'

In addition, following a review of the design boundary conditions laid out in chapter 1, section 8.2.3 goes on to identify the practical limitations attributed to the dielectric-loaded horn, particularly in the context of high-volume, low-cost manufacturing, concluding that;

'The difficulty in sourcing environmentally-stable, low loss dielectric material suitable for high-volume manufacturing, together with the need to produce consistent and homogeneous dielectric cores in a material having a relatively low dielectric constant, jeopardises the anticipated superior performance of the dielectric-loaded horn and consequently steers the designer away from this option, in favour of the corrugated.'

With the two statements above summarising, in the author's view, the state-of-the-art with respect to conventional hybrid-mode feeds, the RF improvements provided by the HE_{11} dual-band horn on its own yield a significant improvement to the design of horn antennas in general.

In addition, following the results of section 8.3, the subsequent improvements to the secondary radiation characteristics of elliptical reflector antennas as a consequence of the new design indicates it can be considered a good solution to the critical issue identified in chapter 5.

Together with the fact that the concept can be implemented in a horn with axial corrugations, thereby lending itself to high-volume manufacturing methods, means it

can also be considered a good solution against the six design boundary conditions identified in Chapter 1.

The HE_{11} dual-band horn therefore represents a useful and, for certain applications, necessary improvement to the overall earth-station terminal performance, one that will certainly offer increased capacity or availability for the satellite networks of the future.

By way of a final synopsis to demonstrate the concept and performance of the HE_{11} dual-band horn, Figure 7.15 (repeated here) shows the crosspolarisation versus frequency for the horn of Figure 7.9. It is interesting to compare this with Figure 3.6 for the conventional corrugated horn as it shows vividly the change to the crosspolar response as a consequence of introducing the TM_{11} mode at the upper sub-band.
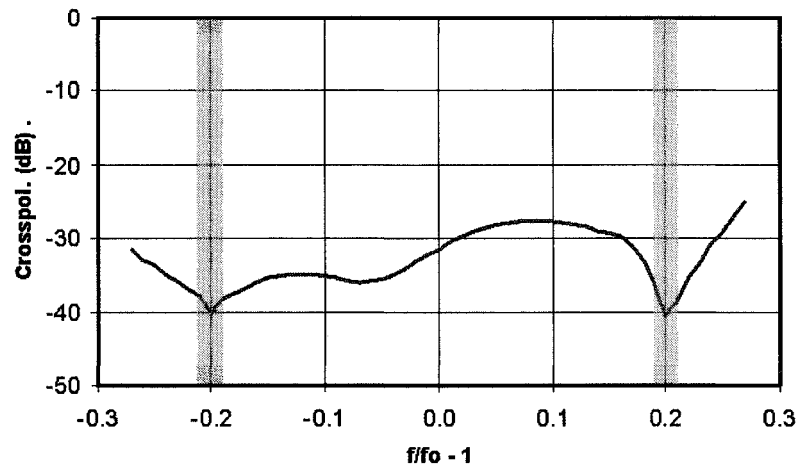
Figure 7.15 (reproduced) *Peak crosspolarisation vs normalized frequency for the axially-corrugated HE_{11} dual-band horn of Figure 7.9 (Obtained using FD-TD code)*

As part of the final summing up, it is appropriate to mention the quality of the measured results obtained during this research. The anechoic chamber facility used to characterise the various horns herein was designed and developed by the author solely to support this work and, as such, was a significant part of the overall research programme.

The facility is described in detail in Appendix 2, which includes details of its performance characteristics including the reflectivity level. However results from Figure 7.8 (page 10) in particular (showing good agreement between theoretical and measured crosspolar levels of better than −40dB) are testament to the integrity of the measurement setup.

With the verification of the concept of the HE_{11} dual-band horn being a key aspect to the core research, the ability to accurately measure feed horns at 30GHz has proven to be invaluable, making the chamber itself worthy of a specific reference here.

9.2 Further Work

Inevitably, through the course of this work, various additional issues have been identified that cannot be covered within the scope of this research and these are discussed here as areas of further work to be investigated by interested parties.

The concept of combining a conventional corrugated horn with that of a dual-mode horn for use as a primary horn to illuminate reflector antennas at 20/30GHz has been shown to provide improvements to both crosspolarisation and return loss characteristics in two widely separated sub-bands. The encouraging results indicate the concept is likely to be useful for other applications, the suitability being dependant on two main issues, these being i) the frequency separation between the upper and lower sub-bands and ii) the required bandwidth at each of the sub-bands. Whilst the two issues are not independent of each other, there are general restrictions that govern the limits of operation, these being set by the modal characteristics of circular waveguide or more specifically, the TM_{11} mode transducer.

Whilst Chapter 6 briefly examined the relationship between the frequency behaviour and the geometric parameters of a waveguide step acting as the mode transducer, further work is required to explore, define and hopefully improve the operational limits of this configuration [9.2].

In particular, from the graph of Figure 7.15 it is recognised that the HE_{11} dual-band horns presented here offer only limited bandwidth at the upper sub-band, due largely to the dispersion between the TE_{11} and TM_{11} modes in the horn throat making it difficult to phase the additional TM_{11} mode with the residual mode content correctly. To a lesser extent, dispersion in the corrugated section itself may also be a factor and is an interesting concept given that a corrugated structure is not usually associated with being able to support the TM_{11} mode.

A secondary issue in this respect may be the TM_{11} cut-off behaviour of the input waveguide (D_1). The attenuation per unit length of this section of waveguide will present a 'soft' short circuit to the TM_{11} mode excited by the step leading to two components of the mode. The first, and dominant, is the portion that travels directly

towards the horn aperture and the second is that which attempts to travel towards the horn input but is reflected back because of the cut-off condition presented by the waveguide.

Further investigations should not be limited to the relative phase of the TM_{11} mode as there is also the need to better understand the optimum mode amplitude, particularly as the bandwidth of the upper sub-band increases and the optimal amplitude to minimise crosspolarisation is likely to vary across the band. Referring to Figure 9.1, the dimensions chosen for the final design of the horn of Figure 7.9 indicate that the mode transducer is operating in an area of the TM_{11} mode transfer function that provides varying mode amplitudes across the relatively narrow band considered here. The significance of this is yet to be explored.

An evaluation of these issues for the horn of chapter 6 may lead to improvements to the useful bandwidth, particularly after the simple geometry of the waveguide-step mode transducer lends itself to computer optimisation, there being only three parameters to set as variables - D_1, D_2 and the length of section D_2. Since increasing the bandwidth at the upper sub-band is perhaps the most significant improvement that could be borne out of further research into this topic, additional investigations would be worthwhile.
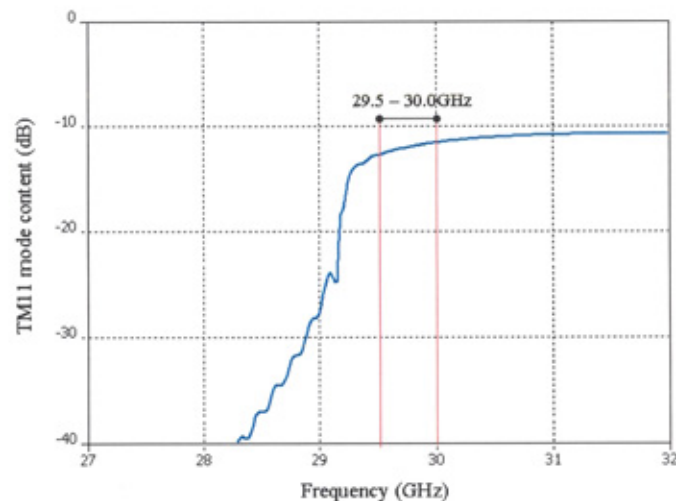
Figure 9.1 *TM₁₁ mode transfer function for the mode transducer used in the axially-corrugated HE₁₁ dual-band horn of Figure 7.9*

With a better understanding of the fundamental issues previewed above, it is possible that greater improvements will stem from use of alternative methods by which to generate and control the TM_{11} mode in the horn throat. Although a step change in the input waveguide is used here, the TM_{11} mode transducer may take various forms. Based on the work carried out by Agarwal [9.3] for example, there may be an advantage to using a dielectric-loaded step to extend the bandwidth. Other ideas include use of a modified profile rather than a step to generate the TM_{11} mode and a more radical solution to avoid the restriction that the input waveguide must be small enough to present a short-circuit to TM_{11} mode may be to use a mode filter in conjunction with dielectric-loading. There are doubtless other possibilities.

Extending the idea of a hybrid solution for feed horns required to operate in two distinct sub-bands opens the way for other combined concepts. One such solution that may provide good results is that which combines the Satoh horn [9.4] with the Potter horn [9.5]. For such a design, the concept developed by Satoh could be optimised for operation at the lower frequency band. At the higher frequency band the magnitude and phase of the TM_{11} mode as a consequence of the dielectric ring is likely to be incorrect for good pattern performance. However, it is postulated that this could be corrected with the introduction of additional TM_{11} mode content by way of a step change in the input waveguide dimensioned accordingly to function only at the higher operating frequencies. The optimum magnitude and phase are likely to need to be determined iteratively and there is a chance, depending on dimensions of the horn itself and the resulting vector addition of the modes at the horn aperture, that an adequate solution may not exist. However, the concept, if successful, is likely to yield a very simple design with good performance in two distinct frequency bands. The useful bandwidths at both the lower and upper operating bands are expected to be narrower than that of the HE_{11} dual band horn of chapter 6, particularly for the lower frequency band. However, for particular applications the concept may represent a high performing, simple, low cost solution as an alternative to the horns examined herein.

9.3 Closing statement

In accordance with the goals of this research activity, having defined the application, developed the theory, identified a critical issue and addressed that critical issue by way of a novel design offering superior performance to that of the state-of-the-art, it is hoped this work will be regarded as a worthwhile exercise and one that has brought about a small but useful progression to the design of antennas for the satellite communication industry.

9.4 References

[9.1]   Clarricoats, P.J.B. and Olver, A.D.: *Broadband low crosspolar horn*, Electronics letters, Dec 1994, Vol. 30, 2085-6.

[9.2]   English, W.J.: *The circular waveguide step-discontinuity mode transducer*, IEEE Trans., Oct 1973, MTT-short papers, pp 633-6.

[9.3]   Agarwal, K.K.: *Phase characteristics of a circularly symmetric dual-mode transducer*, Jan 1970, MTT-18 (correspondence), pp 69-71.

[9.4]   Satoh, T.: *Dielectric-loaded horn antenna*, IEEE Trans., 1972, AP-20, pp 199-201.

[9.5]   Potter, P.D.: *A new horn antenna with suppressed sidelobes and equal beamwidths*, Jet Propulsion Labs publications, June 1963, pp 71-78.

Appendix 1

Radiation from cylindrical apertures

Whilst these principles are treated at length in the literature [A1.1 to A1.5], it is worth reiterating the basic results presented here as the compliment to the modal analysis conducted in the main body of the thesis. The combination of the modal analysis together with the aperture theory herein completes the requirements to undertake theoretical predictions of the radiation patterns for the horns investigated.

A1.1 Vector potential theory

In the analysis of radiation problems it is required to determine the distant radiated fields due to specified sources. To simplify the analysis, a common procedure is to introduce intermediate functions, known as vector potentials. Application of vector potential theory yields solutions to the vector wave equation to describe the radiation into an unbounded, homogeneous region brought about by the effect of current densities J and M. The magnetic vector potential A, due to an electric current source J is given by

$$A = \frac{\mu}{4\pi} \int_S J \frac{e^{-jkR}}{R} \, dS \qquad (A1.1)$$

Similarly, the electric vector potential F, due to a magnetic current source M is given by

$$F = \frac{\varepsilon}{4\pi} \int_S M \frac{e^{-jkR}}{R} \, dS \qquad (A1.2)$$

where R is the distance between the source location and the field point at which A or F is evaluated. The total radiated electric field is obtained from the superposition of the individual fields arising from A and F respectively and as such is given by

$$E = -j\omega A - j\omega\eta F \times \hat{r} \qquad\qquad (A1.3)$$

For many antenna configurations the source distributions are not known exactly and it is useful to develop an alternative method by which the actual sources are replaced by a set of equivalent sources. One such method is the field equivalence principle.

A1.2 Application of field equivalence to aperture antennas

The field equivalence principle is a technique which allows for the radiation patterns of various aperture antennas to be calculated by way of reasonable approximations of the fields on or near the antenna structure and is an extremely useful tool in solving antenna problems.

To apply the field equivalence principle to a waveguide or horn an imaginary surface, S, is chosen to coincide with the radiating aperture. With knowledge of either the magnetic or electric currents, or a combination of them both over the surface, the horn can be removed and and the radiated fields outside of S calculated. If the surface currents are given by

$$\left.\begin{array}{l} J_s = \hat{n} \times H_a \\[3mm] M_s = -\hat{n} \times E_a \end{array}\right\} \quad \text{over the aperture} \qquad\qquad (A1.4)$$

and $\quad J_s = M_s = 0 \quad$ elsewhere on the surface

the radiation equations produced are those originally derived by Chu [A1.6] which can be used to calculate the radiated fields over the complete far-field sphere.

142

Alternative approaches assume the surface currents are given either by

$$M_s = \begin{cases} -\hat{n} \times 2E_a & \text{over the aperture} \\ 0 & \text{elsewhere} \end{cases} \qquad (A1.5)$$

and $J_s = 0$ everywhere

or by

$$J_s = \begin{cases} \hat{n} \times 2H_a & \text{over the aperture} \\ 0 & \text{elsewhere} \end{cases} \qquad (A1.6)$$

and $M_s = 0$ everywhere

where E_a and H_a are the tangential electromagnetic field distributions in the horn aperture and $\hat{n}$ is the unit vector normal to the imaginary surface. The condition in Equation A1.5 is known as the E-field model and that in Equation A1.6 the H-field model. In both cases, to facilitate use of image theory, the surface is extended beyond the aperture to form an infinite plane made up of either a magnetic conducting sheet ($M_s = 0$ everywhere) or an electric conducting sheet ($J_s = 0$ everywhere). The radiated fields are now determined in the presence of the conducting surface and solutions can only be obtained in the forward hemispere.

To develop the radiation models the hybrid coordinate system shown in Figure A1.1 shall be adopted. In it, Cartesian or polar coordinates define a source point on the aperture plane and spherical coordinates define the far-field points. The equivalent current densities over the aperture for Chu's model are given by Equation A1.4. Replacing these in Equations A1.1 and A1.2 leads to

$$A = \frac{\mu}{4\pi r} e^{-jkr} \hat{n} \times \int_a H_a\, e^{jk(\hat{r}\cdot r')} da \qquad (A1.7)$$

$$F = -\frac{\varepsilon}{4\pi r} e^{-jkr} \hat{n} \times \int_a E_a\, e^{jk(\hat{r}\cdot r')} da \qquad (A1.8)$$

where R has been approximated by

$R \approx r$ for amplitude terms

$R \approx r - r'\cos\psi = r - \hat{r}\cdot r'$ for phase terms.

on the assumption that the potentials are to be evaluated at a far off distant point.

The integrals in Equations A1.7 and A1.8 are two-dimensional Fourier transforms generally defined as

$$Q = \int_a H_a e^{jk(\hat{r}\cdot r')} da \qquad (A1.9)$$

$$P = \int_a E_a e^{jk(\hat{r}\cdot r')} da \qquad (A1.10)$$

If, as is often the case, they are known in terms of their x and y components, then with $\hat{n} = \hat{z}$, Equations A1.7 and A1.8 can be rewritten as

$$A = \frac{\mu}{4\pi r} e^{-jkr} \left(-Q_y \hat{x} + Q_x \hat{y} \right) \qquad (A1.11)$$

$$F = -\frac{\varepsilon}{4\pi r} e^{-jkr} \left(-P_y \hat{x} + P_x \hat{y} \right) \qquad (A1.12)$$

Transforming the fields into spherical coordinates and retaining only the θ and φ components, the radiated electric fields are obtained using Equation A1.3 as

$$E_\theta = jk \frac{e^{-jkr}}{4\pi r} \left[P_x \cos\phi + P_y \sin\phi + \eta \cos\theta \left(Q_y \cos\phi - Q_x \sin\phi \right) \right] \tag{A1.13a}$$

$$E_\phi = jk \frac{e^{-jkr}}{4\pi r} \left[\cos\theta \left(P_y \cos\phi - P_x \sin\phi \right) - \eta \left(Q_y \sin\phi + Q_x \cos\phi \right) \right] \tag{A1.13b}$$

If the aperture fields are assumed to be of the TEM type, $\eta Q_y = P_x$, $\eta Q_x = -P_y$. and Equations A1.13 reduce to

$$E_\theta = jk \frac{e^{-jkr}}{4\pi r} \left[(1 + \cos\theta)(P_x \cos\phi + P_y \sin\phi) \right] \tag{A1.14a}$$

$$E_\phi = jk \frac{e^{-jkr}}{4\pi r} \left[(1 + \cos\theta)(P_y \cos\phi - P_x \sin\phi) \right] \tag{A1.14b}$$

In a similar fashion, if only the tangential electric field in the aperture is employed, the radiated fields are given by

$$E_\theta = jk \frac{e^{-jkr}}{2\pi r} \left(P_x \cos\phi + P_y \sin\phi \right) \tag{A1.15a}$$

$$E_\phi = jk \frac{e^{-jkr}}{2\pi r} \cos\theta \left(P_y \cos\phi - P_x \sin\phi \right) \tag{A1.15b}$$

and if only the tangential magnetic field in the aperture is employed, they are given by

$$E_\theta = jk \frac{e^{-jkr}}{2\pi r} \eta \cos\theta \left(Q_y \cos\phi - Q_x \sin\phi \right) \tag{A1.16a}$$

$$E_\phi = -jk\frac{e^{-jkr}}{2\pi r}\eta\big(Q_x \cos\phi + Q_y \sin\phi\big) \qquad\qquad \text{(A1.16b)}$$

The three formulations in Equations A1.14, A1.15 and A1.16 produce corresponding results if the fields over an infinite plane are known exactly. In practice only approximate fields are assumed over the aperture alone and each formulation provides different results. The differences are small for aperture sizes of some wavelengths, but it is apparent that Chu's equivalent model involves several more calculations than those using only one equivalent current, and since it is customary to work with the aperture electric field, the formulation postulating that $J_s = 0$ everywhere is most commonly used.

To allow direct comparison between predicted and measured results it will be advantageous to express the radiated fields in a form which correlates conveniently with standard measurement techniques. Employing Ludwig's third definition [A1.7] the copolar E_{co} and cross polar E_{xp} radiated fields are expressed as

$$\begin{bmatrix} E_{co} \\ E_{xp} \end{bmatrix} = \begin{bmatrix} \sin\phi & \cos\phi \\ \cos\phi & -\sin\phi \end{bmatrix} \begin{bmatrix} E_\theta \\ E_\phi \end{bmatrix} \qquad\qquad \text{(A1.17)}$$

for an aperture electric field polarised in the y direction. For an aperture electric field polarised in the x direction E_{co} and E_{xp} are interchanged.

At this stage no specific aperture geometry has been defined. Since of primary interest is the prediction of radiated fields from waveguides and horns of circular cross-section, the following section determines the radiation equations for this type of aperture.

A1.3 Circular Cylindrical Apertures

A1.3.1 Apertures with constant phase

Typical examples of aperture antennas having constant phase over the aperture are open-ended waveguide and parabolic reflector antennas.

For the case of an aperture in the xy plane

$$r' = \rho' \cos \phi' \, \hat{x} + \rho' \sin \phi' \, \hat{y}$$

In addition

$$\hat{r} = \sin \theta \cos \phi \, \hat{x} + \sin \theta \sin \phi \, \hat{y} + \cos \theta \, \hat{z}$$

from the spherical coordinate transformations, leading to

$$\hat{r} \cdot r' = \rho' \sin \theta \left(\cos \phi \cos \phi' + \sin \phi \sin \phi' \right)$$
$$= \rho' \sin \theta \cos(\phi - \phi')$$

The differential surface $da = \rho' d\rho' d\phi'$ and, following Equations A1.9 and 1.10, components of Q and P are subsequently given by

$$Q_{\hat{x},\hat{y}}(\theta,\phi) = \int_{0}^{2\pi} \int_{0}^{a} H_{a\hat{x},a\hat{y}}(x',y') e^{jk(\rho'\sin\theta\cos(\phi-\phi'))} \rho' d\rho' d\phi' \tag{A1.18}$$

$$P_{\hat{x},\hat{y}}(\theta,\phi) = \int_{0}^{2\pi} \int_{0}^{a} E_{a\hat{x},a\hat{y}}(x',y') e^{jk(\rho'\sin\theta\cos(\phi-\phi'))} \rho' d\rho' d\phi' \tag{A1.19}$$

assuming the fields over the aperture are known in rectangular components. If they are known in cylindrical components the coordinate transformation in A1.20 should be applied [A1.8].

$$\begin{bmatrix} A_x \\ A_y \end{bmatrix} = \begin{bmatrix} \cos\phi' & -\sin\phi' \\ \sin\phi' & \cos\phi' \end{bmatrix} \begin{bmatrix} A_\rho \\ A_\phi \end{bmatrix}$$

(A1.20)

Inserting A1.18 and/or A1.19 into the appropriate Equations A1.14, A1.15 or A1.16 yields the radiated fields for a circular, cylindrical aperture illuminated with a general field distribution having a uniform phase variation.

A1.3.2 Apertures with phase tapers (conical horns)

In most practical cases, such as when used as a primary feed for a reflector antenna, the fields across an aperture are produced by a horn with a finite flare angle giving rise to a tapered aperture phase variation.

Consider the cross-section of the circular conical horn shown Figure A1.2. The fields arriving at the aperture are essentially an expanded version of the spherical waves excited at the origin of the horn. However, for moderate semi-flare angles the aperture field can be represented by the fields due to an equivalent open-ended waveguide plus a spherical phase variation to account for the influence of the flared section. This allows use of the cylindrical aperture theory developed herein to be employed and whilst this procedure is approximate, it works well for horns with semi-flare angles less than about 15 degrees [A1.9] and offers substantial simplifications to the analysis.
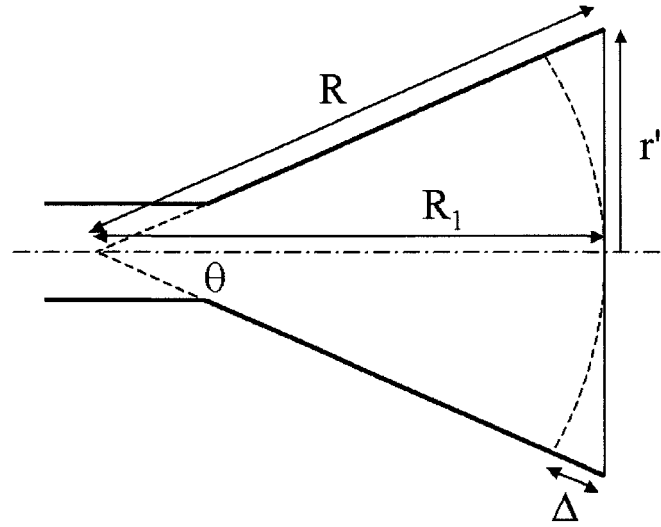
Figure A1.2 *Conical horn – aperture phase taper*

Referring to Figure A1.2 the waves arriving at arbitrary points on the aperture surface have travelled along different path lengths and are therefore not in phase. The path length from the horn apex to the aperture increases from a minimum at the centre to a maximum at the horn's edge. For a sufficiently large aperture it is a valid approximation in the vicinity of the aperture to assume the phase constant is that of free-space, and with this in mind, the aperture phase distribution is given by

$$e^{-jk(\Delta)}$$
(A1.21)

where Δ changes for each position along r'

The differential phase factor $\Delta = R - R_1$ is found as

$$R = \sqrt{R_1^2 + r'^2} = R_1 \left[1 + \left(\frac{r'}{R_1} \right)^2 \right]^{1/2}$$

149

which, provided $r' \ll R_1$ (usually valid for horns with narrow semi-flare angles) can be approximated by

$$R \approx R_1 \left[1 + \frac{1}{2} \left(\frac{r'}{R_1} \right)^2 \right]$$

Then

$$R - R_1 \approx \frac{r'^2}{2R_1} \tag{A1.22}$$

The simulated aperture fields are obtained by multiplying the aperture electric field of the equivalent open-ended waveguide with the spherical phase distribution factor

$$e^{-jk \left(\frac{r'^2}{2R1} \right)}$$

The general radiation integral is consequently given by

$$F(\theta,\phi) = C \int_a E_a e^{jkr'\sin\theta\cos(\phi-\phi')} e^{-jkr'^2/2R_1} da \tag{A1.23}$$

where C is a constant. Whilst it is possible to obtain closed form solutions to A1.23 with the use of Fresnel integrals, the mathematics is cumbersome and it is generally better to solve it numerically.

Equation A1.23 demonstrates that it is possible to represent the aperture field of a flared horn antenna with cylindrical waves and a spherical phase factor. The method is valid for all horn types of moderate semi-flare angle, however the geometry of horns with larger flare angles violates the assumption made in A1.22 and it is necessary to employ an alternative technique where the aperture distribution is described in terms of spherical modes [A1.10]. This will not be addressed here.

A1.4 References

[A1.1] Schelkunoff, S.A.: *Electromagnetic waves*, Van Nostrand, Princeton, N.J., 1943.

[A1.2] Colin, R.E. and Zucker, R.: *Antenna theory Parts I and II*, McGraw Hill, N.Y., 1968.

[A1.3] Harrington, R.F.: *Time harmonic electromagnetic fields*, McGraw Hill, N.Y., 1961.

[A1.4] Stutzman, W.L. and Thiele, G.A.: *Antenna theory and design - 2nd edition*, John Wiley, N.Y., 1981.

[A1.5] Silver, S.: *Microwave antenna theory and design*, McGraw Hill, N.Y., 1949.

[A1.6] Chu, L.J.: *Calculation of the radiation properties of hollow pipes and tubes*, J. App. Phys., 1940, Vol. 11, pp 603-10.

[A1.7] Ludwig, A.C.: *The definition of cross-polarisation*, IEEE Trans., 1973, AP-21, pp116-9.

[A1.8] Balanis, C.A.: *Antenna theory – analysis and design*, John Wiley & Sons, 1982.

[A1.9] Parini, C.G.: *Transmission and radiation characteristics of corrugated waveguides*, Ph.D. thesis, London University, Oct. 1976.

[A1.10] Clarricoats, P.J.B., Olver, A.D.: *Corrugated horns for microwave antennas*, IEE Electromagnetic Wave Series, Vol 18, 1984.

Appendix 2

Antenna measurements

As with the design of any antenna it is important to be able to accurately measure its performance in order to verify its suitability for the intended application. This not only allows qualification of the particular antenna-under-test but, as in this case, also the theory and methodology used in its design.

This appendix describes the considerations and activities undertaken in the design, construction and evaluation of a low-cost anechoic chamber and measurement system developed solely to support this research. It describes some of the key performance and design parameters and attempts to offer general guidelines and basic information, as taken from the articles and books referenced within. Of particular note, because of the scope and detail they provide in all aspects of anechoic chamber design are the articles by Galagan [A2.1] and Appel-Hansen, Dyson, Gillespie and Hickman [A2.2] and the IEEE standard [A2.3].

A suitable enclosure and its incorporation into a fully automated measuring system to characterise small aperture horn antennas in the range 18-30GHz is presented. Methods to assess its level of performance are described and results given to indicate the effectiveness of the facility. It has been developed specifically to support the work of Chapter 7 where a practical investigation into the different horn-types presented in the main body of the thesis is conducted.

A2.1 Indoor test ranges – background

To accurately simulate free-space conditions the primary consideration in the design of an anechoic chamber is the creation of a region of uniform field free from reflection within which the antenna under test is located. The extent to which this can be achieved is related primarily to i) the separation between the antenna under

test and the source antenna and ii) the degree to which reflected signals can be suppressed.

To identify the requirements for an indoor test range it is necessary to look closely at the mechanism by which antennas radiate electromagnetic energy with reference to their intended application. The majority of applications result in long transmission distances between the source and the receiver and as such the antenna is illuminated with a plane-wave field. Whilst this is so, it is not practical, and often not possible, to maintain such a large transmission distance within an indoor test facility. Consequently it is necessary to establish a minimum value for the distance R between two antennas such that the phase curvature of the illuminating wavefront is small enough for it to be regarded as a good approximation to a plane-wave.

To appreciate this issue it is noted that the space surrounding an antenna can be sub-divided into three principle regions [A2.4], these being;

i) the reactive near-field, defined as "that region of the field immediately surrounding the antenna wherein the reactive field predominates", and for most antennas exists within a distance of about $\lambda/2\pi$ from the antenna surface.

ii) The radiating near-field or Fresnel region, defined as "that region of the field of an antenna between the reactive near-field and the far-field regions wherein radiation fields predominate and wherein the angular field distribution is dependant upon the distance from the antenna." In this region the radial field component may be appreciable.

iii) The radiating far-field or Fraunhofer region, defined as "that region of the field of an antenna where the angular field distribution is essentially independent of the distance from the antenna." In this region the field components are essentially transverse.

Whilst no abrupt changes occur at the boundaries, there are distinct differences between the field distributions in each region. Most significantly, the boundary between the latter two radiating regions is generally regarded as being at that distance for which directly measured data represents with sufficient accuracy the far-field characteristics. As such it is taken as the minimum distance required to recreate

153

the condition whereby the antenna under test is illuminated by a so called quasi plane-wave.

For measurements of most aperture antennas the distance R is generally accepted to be given by

$$R \geq 2D^2 / \lambda \qquad\qquad\qquad\qquad (A2.1)$$

where D is the largest aperture dimension. Assuming a spherical wavefront, this corresponds to a maximum path length difference between field contributions from the centre to the edge of the aperture of $\lambda/16$ or a phase difference of $22.5°$.

Assuming the separation between two antennas satisfies Equation A2.1, the additional requirement to ensure accurate results is that the received signal is not subjected to interference from reflections. In an effort to fulfil this need early antenna engineers postulated that if the boundaries of a given volume, within which the antennas were measured, were covered with a material capable of absorbing all or a large proportion of the energy incident upon it, reflections would be negligible and the desired condition achieved [A2.5]. Such a facility could be constructed indoors, its size being mainly dependent on the separation distance R. This concept became the origin of what we now call the 'anechoic' chamber from the Latin word meaning 'without echo'.

The extent to which reflected energy can be suppressed within a defined region determines the *reflectivity level* of the chamber, this being the key figure of merit against which the quality of the chamber is usually judged. It is dependant firstly on the level of energy incident upon the walls of the chamber and secondly by the level of absorption offered by the material covering the walls. There are also other performance parameters to consider, as outlined next.

A2.2 Anechoic chamber performance parameters

With the goal to simulate free-space conditions within a finite enclosure and assuming interference from external sources is negligible, there are potentially five sources of error that may limit the accuracy of measured results, these being;

i) reflectivity

ii) phase variation

iii) transverse and longitudinal amplitude taper

iv) crosspolarisation

v) path loss uniformity

A2.2.1 Reflectivity

This source of error usually has most impact on the accuracy of measurements undertaken within the chamber and as such, it is important to be able to quantify its effect.

It is inevitable that a percentage of the energy incident on the chamber walls is reflected. Consequently, at any point the total power is a combination of two components - the direct and reflected waves. The aim is to produce a volume within the chamber where the reflected energy has a negligible effect within which the antenna under test is located. This 'quiet zone', as it is termed, can be a sphere, a cylinder or even a rectangular box centred on the axis of the chamber and is defined as that volume where the reflected rays from all surfaces bounded by the chamber are less than the direct ray by a specified amount expressed in dB and referred to as the reflectivity level. The lower the reflectivity, the better the chamber is said to simulate free-space conditions and consequently, measurements taken within it are said to be more accurate.

However, it should be pointed out that in reality, due to the polarisation sensitivity of the antenna and the fact that at any point the reflected energy is made up of an infinite number of components from all surfaces within the chamber, the reflectivity level is not a measure of the magnitude of the total reflected field. Instead it is an

indication of the effect such reflections have on measured results in terms of the magnitude of any subsequent errors. It represents an equivalent reflected signal which when propagating along the axis of the receiving antenna would have the same net effect as that observed due to the actual multiple reflections [A2.6].

A2.2.2 Phase Variation

Over a fixed area the variation in phase curvature of a radiating wave front is a function of the radius of the spherical wave. Applied to an anechoic chamber the phase variation over the test region is primarily a function of the separation R between the two antennas. As discussed in section A2.1, a commonly employed criterion is to limit this phase variation to 22.5°. This can cause deep sidelobe nulls to become 'filled-in' [A2.3 – Figure 3] and although the effect may appear quite considerable, provided the amplitude variation limit is not exceeded, it is not generally a problem so long as the engineer is aware it exists.

A2.2.3 Amplitude variation

Throughout the test region the illuminating field should be sufficiently constant in amplitude. This is particularly the case in the plane transverse to the range axis where excessive amplitude taper can result in a reduction in measured gain [A2.7] and slight modifications to the close-in side lobes [A2.2]. The degree of taper is controlled by the directivity of the source antenna; the lower the directivity, the more uniform the field. However, the increased illumination of the chamber walls brought about by the use of a source antenna with broader beamwidth adds greater dependence on the ability of the material covering the walls to absorb more energy and may therefore cause even greater errors due to reflections. As a compromise it is generally required to choose a source antenna such that the amplitude taper over the test region is +/-0.25dB. In the longitudinal direction, when it cannot be controlled as closely since the power varies inversely as the square of the separation distance, an acceptable limit is regarded as 2dB [A2.1 – Part 3], although this is ultimately dependant on the particular type of antenna being measured [A2.3 – section 4.2.4].

156

A2.2.4 Crosspolarisation

The crosspolarisation characteristics of the chamber are especially important in this application. Such characteristics control the purity of polarisation as the wave propagates from one antenna to the other. Since it is required to be able to measure feeds with crosspolar levels of the order of -40dB, the crosspolar contribution from the chamber itself must be less than −50dB to limit the measurement uncertainty to less than +/-2dB.

A2.2.5 Path Loss Uniformity

Path loss uniformity is a measure of the difference in transmission loss characteristics between waves polarised in orthogonal planes. Any such difference is usually a result of a non-symmetrical design and is particularly apparent with circularly polarisation where waves starting off circularly polarised end up elliptically polarised. For this application, where only linearly polarised antennas are being investigated and there is no requirement to measure absolute gain, this is not thought to be a critical design parameter although any difference should be limited to within +- 0.25dB [A2.1 – Part 3].

A2.3 Anechoic chamber design parameters

Having identified in section A2.2 the key parameters that dictate the quality of the measurement environment, the following section discusses some of the design considerations that influence the degree to which they can be satisfied within an anechoic chamber. Throughout this discussion regard should be given to the inevitable constraints on size, access and cost, the designer may be subjected to; the objective being to design an chamber that is as small as possible, with the least expensive materials whilst still achieving the desired performance.

A2.3.1 Shape

Early designs were rectangular in shape and had relatively poor reflectivity levels of the order of -20dB, due largely to the poor absorber materials available at the time. Various methods were tried to improve on this [A2.5] but it was not until 1967, when Emerson [A2.8] devised the 'tapered' chamber, that any significant improvement to chamber performance was made; the sloping sides having the effect of straightening out the wave front at a faster rate than in a rectangular chamber. More importantly, the image sources are much closer together than for a rectangular chamber and as such the transverse amplitude variation resulting from the difference in path lengths of the direct and the reflected illumination of the quiet zone was reduced. This type of design is particularly useful at frequencies below 1GHz when the performance of absorber material deteriorates significantly and it becomes increasingly difficult to control the illumination of the longitudinal surfaces with the use of directional antennas. However, for frequencies well above 1GHz this is not an issue and certainly for measurements above 18GHz it can be said the performance of a tapered chamber is similar to that of a rectangular chamber. Furthermore it should be noted that certain types of measurements, including absolute gain measurements based on the Friis transmission formula, cannot be carried out accurately, or indeed at all, in a tapered chamber due to path loss phenomena [A2.9]. For general application then, and especially for gain and pattern measurements in the range 18-30GHz, it can be concluded that the rectangular chamber is the more useful.

A2.3.2 Length

As discussed, the length of a chamber is dependant on the lowest frequency of operation and the size of the antennas under test. Using the generally accepted condition for far-field measurements the source and transmitter must be separated by a distance $R \geq 2D^2 / \lambda$. In addition clearance for each of the antennas should be included to obtain the total length of the chamber. A distance of approximately half the width of the chamber behind each antenna is usually allowed to avoid the adverse effect of coupling to the end walls and ideally a similar distance behind the transmitting antenna [A2.1 – Part 2 and A2.6].

A2.3.3 Width

The width is a critical parameter since for a given dB rating of absorber material on the chamber walls, it is often the most influential parameter on the magnitude of reflections from the walls.

There is no optimum value from an electrical point of view since chamber performance improves with increasing width. For the present design, where the aim is to provide good performance at reasonable cost, the following considerations should be borne in mind. Firstly, absorber performance deteriorates as the angle of incidence, θi, of the incoming wave increases (normal incidence = 0°) [A2.10]. To make maximum efficient use therefore of the absorber material, the chamber width should be chosen to ensure θi does not exceed, ideally, 60° at the point of main specular reflection, ie. that point on the walls, floor or ceiling of the chamber half way between the two antennas. Associated with this is the fact that if the width is large enough to ensure no part of the source antenna's main radiated lobe is incident on the side walls, the magnitude of subsequent reflections may also be reduced. The extent to which this can be achieved is inherently dependent on the directivity of the source antenna. For antennas with high directivity the performance of the absorber material, on the floor, ceiling and side walls at least, becomes less critical, although it is noted that as the directivity increases, the separation between the antennas must also increase if the far-field requirements of Equation A2.1 are to be satisfied. The optimum financial solution is therefore a compromise between the cost of the absorber and the cost of the enclosure itself.

These considerations suggest an optimum length to width ratio of 3:1 to conserve on building materials or 2:1 to improve electrical performance. The cross-section of the chamber is made square in order to preserve symmetry and ensure propagating energy has equal path loss.

A2.3.4 Absorber

There is a requirement for a suitable material to line the inner surfaces of the chamber with properties that ensure i) a good match at the interface between itself

and free-space, and ii) complete absorption of all energy incident upon it. Over the years many different ideas have been tried [A2.1 – Part 1 and A2.5] with varying degrees of success, however in recent times the familiar pyramidal shaped, polyurethane based material has proved most successful. The pyramidal spikes act as a resistive taper to gradually match the impedance from that of free space to that of the material itself providing a good VSWR, while the thick, carbon-loaded base absorbs and dissipates the energy.

The size, or more specifically the depth, of the material with respect to the wavelength is usually directly proportional to the ratio between reflected energy and incident energy expressed in dB. However for a given frequency absorber becomes more expensive as its dB rating improves, hence the objective is to use material capable of achieving the desired performance without incurring excessive costs. Unfortunately there is no direct link between absorber rating and overall chamber performance since too many other factors contribute towards the reflectivity level.

Whilst it is not uncommon to use the same size absorber all over, better performance can be achieved by placing superior material at specific regions within the chamber. The back wall, for example, is illuminated with the full impact of the transmitted wave and must totally absorb all the energy incident upon it. Similarly, the performance of the absorber in the region of main specular reflection suffers due to the increase in the angle of incidence of the incoming wavefront. In both areas definite advantages can be gained with the use of sufficiently deep material having a dB rating of typically -50dB for this application. Elsewhere, the absorber is sized one size smaller to absorb secondary reflections.

A2.3.5 Shielding

As well as having a means with which to absorb electromagnetic energy at the boundary of the test chamber, there is also a requirement to prevent direct transmission through the absorbing material into adjacent areas and conversely, prevent external radiation from 'contaminating' the controlled conditions within the chamber. This is best achieved using a metallic liner throughout the interior surface upon which the absorber is mounted.

The degree of shielding needed is very much dependant on the application and types of measurement to be undertaken and could lead to significant attention to detail and cost throughout all aspects of the chamber design to ensure the required levels of RF leakage. For this application there is no requirement beyond that of the metallic liner, on to which the absorber is mounted.

A2.3.6 General

Other parameters to be considered include the power dissipating capability, the support capability of the floor, the degree of access, the method by which the source antenna is supported and the method by which the test objects are supported, moved and controlled, this usually being done with an antenna positioner as described in the next section.

A2.4 Design of an anechoic measurement system for high performance feed horns in the range 18-30GHz

With the performance parameters of section A2.2 in mind and after applying the design considerations outlined in section A2.3, a suitable facility to support this research into small aperture feed horns at 18-30GHz has been designed and constructed [A2.11].

A2.4.1 Chamber

The relatively small size of the horn apertures (in wavelengths) being considered here means that the far-field requirement is satisfied in a chamber of very modest dimensions.

The chamber could not be made a permanent fixture but needed to be constructed in a manner which allowed disassembly if required. This placed restrictions on the size and method of construction as different parts of the chamber needed to be portable. In addition, since it was hoped the chamber could be used to aid demonstration of

antenna characteristics to undergraduate students [A2.12] maximum accessibility and ease of use were considered important factors.

Following section A2.3.1, a rectangular design was selected with dimensions 2.25m x 1.20m x 1.20m. Externally the chamber is constructed from 1.20mm thick aluminium sheet supported by a wooden skeletal frame to provide mechanical rigidity. The six sides are constructed individually and assembled by means of pinned hinges thereby allowing it to be dismantled and reassembled. Each panel can be swung open enabling the chamber to be used in conjunction with an outdoor range if required.

A view of the chamber, with one side open to illustrate the manner of construction, is shown in Figure A2.1. Following the discussion in section A2.3.4 the walls are lined with two grades of absorber. The back wall, behind the antenna-under-test, and central sections of the side walls are lined with 150mm depth pyramidal material, specified as having reflection loss (dB rating) better than 50dB at 18Ghz for normal incidence, whilst the remainder of the chamber is lined with 80mm depth material, specified as having reflection loss better than 44dB at 18Ghz for normal incidence [A2.10]. The blocks of absorber have been glued to the aluminium walls, although a more flexible arrangement would be to use industrial Velcro.

With the chamber being quite small a length to width ratio of approximately 2:1 was chosen to maximise the electrical performance without incurring a significant increase in the amount of absorber material required.

A2.4.2 Antenna supports and positioner

To obtain radiation patterns there is a need for some way of positioning and rotating the test antenna in order that readings can be taken at each of a number of discrete positions and orientations. This is achieved using the antenna positioner pictured in Figure A2.1. It provides azimuthal rotation only, elevation pattern cuts being achieved by turning the device under test through 90 degrees about its longitudinal axis. The positioner is constructed mainly from wood and perspex to minimise reflections and is powered by a small stepper motor housed in the base, having a resolution of 0.5°. The platform can be adjusted in height to accommodate different

antennas and is also offset from the centre of rotation to facilitate optimum positioning of the antenna with respect to its phase centre. The weight of the antenna is relieved from the stepper motor output shaft by means of a thrust bearing. A micro-switch located on the main shaft of the support structure has been incorporated into a simple logic circuit to ensure the platform returns to a fixed reference position at the beginning of each measurement.

The source antenna is supported by means of a metal shaft located within a steel bushing through the end wall of the chamber. This allows for rotational and longitudinal positioning of the source antenna to facilitate measurements in different planes. The distance between the source and test antennas is adjustable from 1.00m to 1.40m resulting in a typical path loss of approximately 60dB for frequencies in the range 18 to 30GHz.

A2.4.3 Instrumentation

A Wiltron 360 vector network analyser provides the source and receiver. Such instruments present themselves as a very attractive alternative to conventional instrumentation provided powers in excess of typically, 0dBm are not required. The synthesised source is inherently stable and in its existing form can cover the range 200MHz to 40GHz. It can support an IEEE bus interface to facilitate control, data acquisition and automation. When operated in the CW mode with a reduction in the IF bandwidth the dynamic range can be optimised to better than 100dB. This, together with the use of averaging, where up to 1000 measurements can be averaged for each recorded result, makes the network analyser an extremely powerful tool with which to conduct antenna measurements. Furthermore, use of a *vector* network analyser in particular enables both magnitude and phase measurements to be carried out.
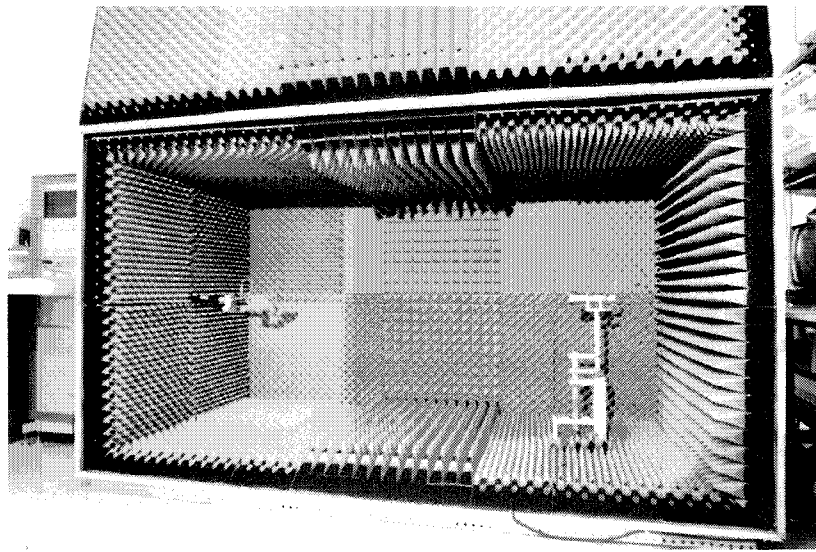
Figure A2.1 *View of anechoic chamber with side door fully open. Network analyser located far left.*

A2.4.4 Overall layout and operation

The chamber, positioner and network analyser have been incorporated into a fully automated antenna pattern measurement system interconnected via the IEEE interface bus and under the direction of a PC as illustrated in Figure A2.2. By this method an operator can control azimuthal rotation of the antenna, data acquisition and data presentation from a single point.

The hardware and software for control of the positioner have been developed at the University and allow the user to select angular resolution, start and stop positions and number of steps.

The analyser is set up so that one port is connected via a short section of co-axial cable to the source antenna and the second port is connected via a four meter length of high quality, low loss co-axial cable to the test antenna. Before the start of each measurement cycle the software returns the positioner to its reference position. The aspect angle of the test antenna is subsequently incremented and for each angle the

value of the S21 marker is recorded. Data is processed by the PC and either storred to disk or displayed on the screen as a normalised or absolute radiation pattern.

20dB standard gain pyramidal horns are used as the source antennas; one covering the range 18 to 26.5GHz and the other 26.5 to 40GHz. For test antennas with directivities of the order of 15dB, and after accounting for cable losses which at 30GHz approach 10dB, this arrangement leads to a system dynamic range of >50dB. An externally mounted video camera has been installed above the positioner to provide a visual indication of the antenna aspect during testing when the chamber is closed.
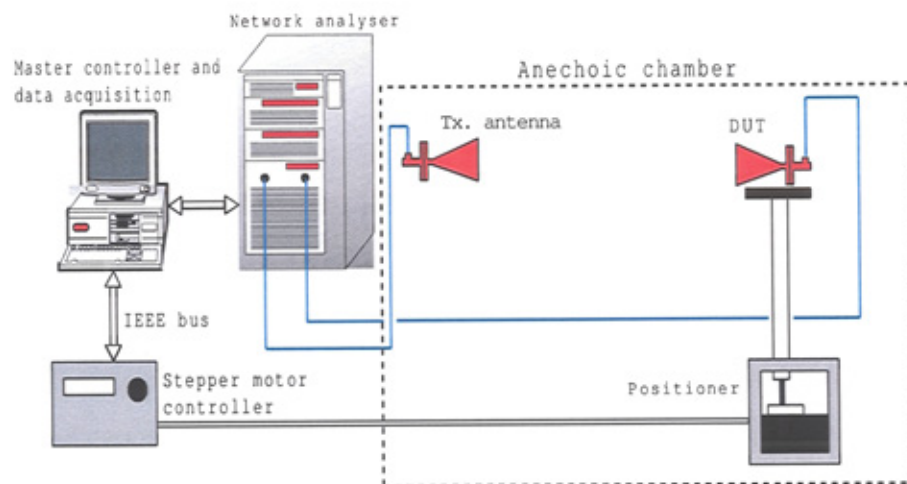

Figure A2.2 *Antenna radiation pattern measurement system*

A2.5 Evaluation of chamber reflectivity

Because of its strong influence on the accuracy of measured results the reflectivity level is the parameter recognised as the figure of merit to describe chamber performance. As such, since the advent of the anechoic chamber in the 1950's, there

have been several methods suggested for obtaining a measured value to indicate chamber performance. Over the years, two methods, referred to as the antenna-pattern comparison technique (APC) and the free-space voltage standing-wave ratio technique (VSWR), have proved to be the most satisfactory since the results they yield lend themselves to the production of data and graphs from which chamber performance can be evaluated [A2.6]. The following section briefly describes these two techniques.

A2.5.1 APC technique

The pattern comparison technique relies on the small variations that occur when a series of radiation patterns are taken at different positions throughout a defined area surrounding the usual position of the test antenna. From the magnitude of these variations the uncertainty of the recorded patterns is determined.

The chamber is illuminated in the usual manner by a source antenna located at one end. The received pattern is recorded at closely adjacent test points along the three principal planes defining the desired quite zone and sets of patterns obtained in each case. Each pattern within a set is superimposed on top of the reference pattern, usually taken as that recorded with the receiving antenna positioned on the central axis of the chamber, having been normalised to ensure the peaks of the main lobes coincide. The deviations of each pattern from the reference are determined at different aspect angles, ϕ, and the results obtained at each angle plotted against the relative position of the test point with respect to the chamber axis. The observed cyclic variation of the deviation with distance displays the interference pattern arising from the interaction between the direct and reflected signals to which the antenna is sensitive, from which the reflectivity level is readily determined [A2.2].

It is evident that at each aspect angle and for each of the different sets of received patterns, changes in the deviation plots will yield a range of values for the reflectivity. Since it is desirable to end up with a single value expressing the overall performance of the chamber, the range of values are often averaged or otherwise statistically manipulated to yield a final figure of merit.

A2.5.2 VSWR technique

The source and test antennas are positioned as if to undertake a conventional pattern measurement except that the test antenna is tilted in the horizontal plane to a given aspect angle, ϕ. Whilst maintaining this angle the test antenna is moved on a traverse line coinciding with one of the three principal planes defining the quiet zone. At a number of closely spaced test positions the received power is recorded and plotted against the distance travelled in relation to the central axis of the chamber. As with the APC technique, the resulting interference pattern is assumed to be a consequence of the in- and out-of-phase interaction of the direct and reflected rays from which it is possible to determine the reflectivity level. The process is repeated for various aspect angles, across different planes and for different polarisations to yield an overall value which is then put forward as the figure of merit representing the expected accuracy for measured results at a given frequency.

Comparing the two techniques shows them to be essentially the same since from the antenna patterns obtained using the APC technique discrete points of the interference curves obtained using the VSWR technique can be identified and vice versa. However, as a consequence of differences in the way final results are analysed, the VSWR technique tends to be more suited to determining the worst case or maximum reflectivity level, unlike the APC technique, where results are averaged.

For this reason it is the VSWR technique that has been used to evaluate the chamber developed here.

A2.6 Chamber performance - measured results

A2.6.1 Reflectivity

The VSWR method has been used to determine the reflectivity level within a sphere of diameter 14cm centred about the receiving antenna. A 20dB standard gain horn was used as the transmit antenna, however a corrugated horn was chosen as the receive antenna as a typical example of the type of antenna being tested in the

chamber. In this way the reflectivity level is more relevant, if not absolutely specific, to other horns of this type.

A number of measurements were taken at various aspect angles, across different planes within the quiet zone and for the two principle polarisations. Figure A2.3 shows an example of an interference curve at 18.5GHz as the receive antenna is traversed across the chamber in a horizontal line normal to that connecting the receiving and transmitting antennas. Note that the measured power is normalised to the on-axis copolar main lobe level for the condition when the two antennas are pointing towards each other. The oscillations show the interference between the direct and reflected signals, with the variation in the average level being due, in this case, to the scanning of the two antenna patterns.

For the analysis and interpretation of the interference curve the reader is directed to [A2.2], section 8.11.3 for additional details and illustrations of the related graphs. The basic calculation is described here with use of Figure A2.4 which represents a sub-set of data used in the aforementioned reference.

The reflectivity level R, is found from the maximum peak-to-peak variation, σ, and the average received power, a, (shown dashed) at the point where this occurs. In this case $\sigma = 2.4$dB and $a = -37.8$dB. Figure A2.4 relates σ to the number of dB by which the reflectivity level is below the pattern level, alternatively referred to as the interference distance, I. Hence, $R = a - I$.

For the value of σ indicated in Figure A2.3, Figure A2.4 indicates I to be 17.25dB, and consequently the reflectivity level is better than -55dB. Other results taken in a similar way suggest that within the quiet zone a reflectivity level better than -52dB has been achieved.
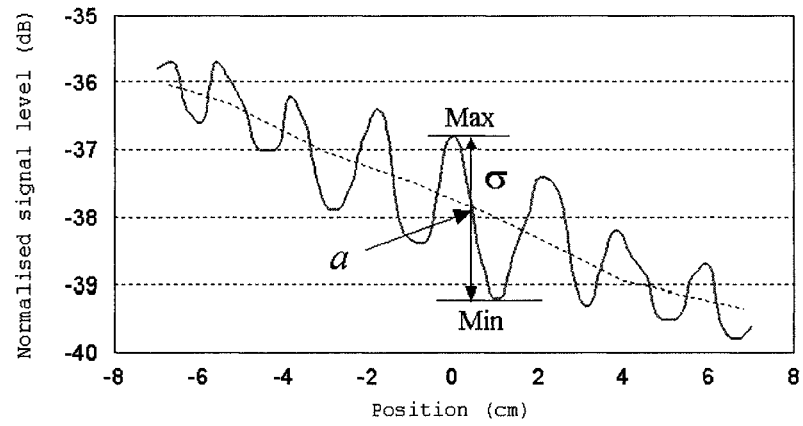
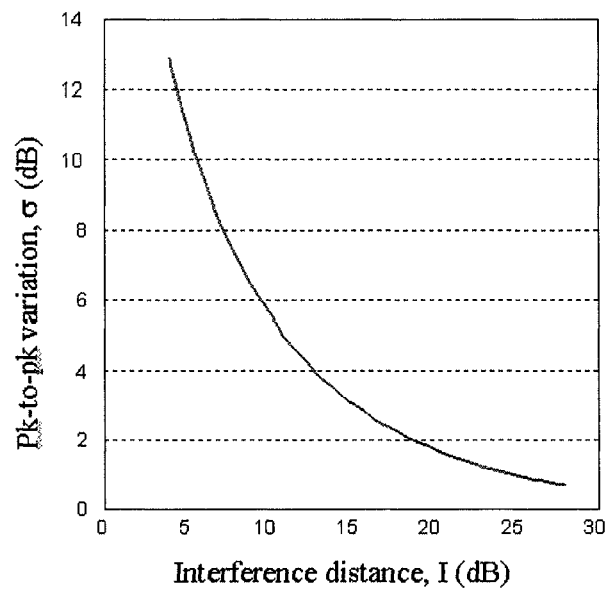Figure A2.3 *VSWR interference curve @ 18.5GHz for the chamber of Figure A2.1*

Figure A2.4 *Interrelationship between peak-to-peak variation (σ) and Interference distance (I) as required to calculate reflectivity level.*

A2.6.2 Amplitude variation

As the antenna, positioned on axis, is traversed across the quiet zone, the amplitude variation of the received signal should be limited to less than $\pm$ 0.25dB in order to approximate the far-field requirements and ensure sufficiently accurate results.

This has been measured and in the H-plane is within $\pm$ 0.2dB, however in the E-plane a maximum variation of 0.35dB was recorded at the upper frequency limit. This is thought to be due to mechanical difficulties in aligning the test apparatus at such frequencies as oppose to being a fault with the chamber since the far-field requirement of R = 0.82m is easily met.

A2.6.3 Crosspolarisation

Measurements taken on boresight in both principle planes and the 45 degree plane show the level of crosspolarisation to be below -55dB. Beyond this level the received power approaches the noise floor of the receiver, especially at the upper frequency limit (approx. -100dBm), and it becomes increasingly difficult to obtain a steady result. In any case such levels are of the same order as the reflectivity level and are therefore subject to large inaccuracies.

A2.6.4 Path loss uniformity

In addition to low crosspolarisation, the chamber must posses ' path loss uniformity ' in that horizontally and vertically polarised signals should be transmitted with the same transmission loss. Failure to achieve this causes the rotation of the polarisation of the principal wave, an effect particularly noticeable with circular polarisation where waves starting off circularly polarised end up elliptically polarised. The difference between the path loss for each of the principle planes has been measured and is within $\pm$ 0.2dB.

A low cost anechoic measuring system has been presented, the heart of which is the anechoic chamber. This has been characterised as having a reflevtivity level better than -52dB for frequencies between 18 to 30GHz. For high performance feeds, such as corrugated or dielectrically loaded horns, this equates to errors of the order of 2dB for typical crosspolar pattern levels of -40dB. The chamber and a simple positioner have been incorporated into a fully automated antenna pattern measuring system in order to determine the radiation characteristics of various horn antennas with a high degree of accuracy and consistency.

The performance is consistent with one proposal put forward by Clarricoats and Olver for accurate measurements of corrugated horns [A2.13] suggesting that the background reflectivity should be at least 10dB lower than the minimum pattern level to be recorded.

A2.7 References

[A2.1] Galagan, S.: *Understanding microwave absorbing materials and anechoic chambers. Parts 1 to 4*, Microwaves, Dec 1969 – May 1970.

[A2.2] Rudge, A.W., Milne, K., Olver, A.D., Knight, P. (editors): *The Handbook of Antenna Design. Vol. 1 and 2*, IEE Electromagnetic Wave Series, Vol. 15 and 16, 1986. Chapter 8 by Appel-Hansen, J., Dyson, J.D., Gillespie, E.S., Hickman, T.G.

[A2.3] IEEE Standard 149-1979: *Test procedures for antennas*, (revised 1986).

[A2.4] Balanis, C.A.: *Antenna Theory – analysis and design*, John Wiley & Sons, 1982.

[A2.5] Emerson, W.H.: *Electromagnetic wave absorbers and anechoic chambers through the years*, IEEE Trans., 1973, AP-21, pp 484-90.

[A2.6] Appel-Hansen, J.: *Reflectivity level of radio anechoic chambers*, IEEE Trans., 1973, AP-21, pp 490-8.

[A2.7] Jull, E.V.: *Finite-range gain of sectoral and pyramidal horns*, Electronics Letters, Vol. 6, 1970, pp 680-81.

[A2.8] Emerson, W.H., Sefton, H.B.: *An improved design for indoor ranges*, Proc. IEEE, Vol. 53, 1965, pp 1079-81.

[A2.9] King, H.E., Shimabukuro, F.I., Wong, J.L.: *Characteristics of a tapered anechoic chamber*, IEEE Trans. AP-15,May 1967, pp 488-90.

[A2.10] GEC-Marconi Materials specification bulletin: - *Materials/933/DS, broadband absorber, AF range*, 1990.

[A2.11] Geen, D.C. and Smith, D.: *Design, construction and performance of a small, low cost anechoic measuring system for research applications*, IEEE AP-S International Symposium, 1995, Newport Beach, California, USA, Vol. 4, pp1738-1741.

[A2.12] Geen, D.C. and Smith, D.: *Compact anechoic chamber and antenna measurement system for microwave teaching and research applications*, Microwave and Optics Technology Letters, 1996.

[A2.13] Clarricoats, P.J.B., Olver, A.D.: *Corrugated horns for microwave antennas*, IEE Electromagnetic Wave Series, Vol 18, 1984.

This page intentionally left blank